INFORMATION TO USERS

MICROSTRUCTURAL DEVELOPMENT AND SEGREGATION EFFECTS IN

DIRECTIONALLY SOLIDIFIED NICKEL-BASED SUPERALLOY PWA 1484

Lichun Li

A Dissertation

Submitted to

the Graduate Faculty of

Auburn University

in Partial Fulfillment of

the Requirements for the

Degree of

Doctor of Philosophy

Auburn, Alabama

May 11, 2002

UMI Number: 3044010

UMI®

MICROSTRUCTURAL DEVELOPMENT AND SEGREGATION EFFECTS IN

DIRECTIONALLY SOLIDIFIED NICKEL-BASED SUPERALLOY PWA 1484

Except where reference is made to the work of others, the work described in this thesis is my own or was done in collaboration with my advisory committee.

Lichun Li

Certificate of Approval:

Bor Z. Jang
Professor
Mechanical Engineering

Ruel A. Overfelt, Chair
Professor
Mechanical Engineering

Jeffrey Fergus
Associate Professor
Mechanical Engineering

Ralph H. Zee
Professor
Mechanical Engineering

Stephen L. McFarland
Acting Dean
Graduate School

VITA

Lichun Li, son of Suzheng Liu and Qinxiu Li, was born on February 2, 1965, in Benbu, Anhui province, P.R.China. He attended Tsinghua University, P. R. China, where he received his Bachelor of Science degree in mechanical engineering in 1987, and Master of Science degree in the major of Metallic Materials and Heat Treatment in 1990. He then worked as an engineer at Beijing Mechanical Design and Research Institute for 4 years and Nichimen Corporation for 2 years. He came to Auburn University to pursue a Doctor of Philosophy degree in Mechanical Engineering in September 1996. He married Jianjun Zhang, daughter of Doctor Zhiying Chen and Wanliang Zhang, in June 1992.

DISSERTATION ABSTRACT
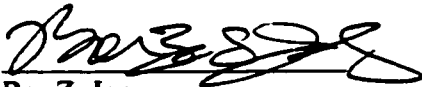

MICROSTRUCTURAL DEVELOPMENT AND SEGREGATION EFFECTS IN

DIRECTIONALLY SOLIDIFIED NICKEL-BASED SUPERALLOY PWA 1484

Lichun Li

Doctor of Philosophy, May 11, 2002
(M.S. Tsinghua University, P. R. China, 1990)
(B.S. Tsinghua University, P. R. China, 1987)

180 Typed Pages

Directed by Dr. Ruel A. Overfelt

These studies were performed to investigate the effects of thermal gradient (G)

and growth velocity (V) on the microstructure development and solidification behavior of

directionally solidified nickel-based superalloy PWA 1484. Directional solidification

(DS) experiments were conducted using a Bridgman crystal growth facility. The

solidification velocity ranged from 0.00005 to 0.01 cm/sec and thermal gradients ranged

from 12 to 108 °C/cm. The as-cast microstructures of DS samples were characterized by

using conventional metallography; chemical composition and segregation of directionally

solidified samples were analyzed with energy dispersive spectroscopy in SEM.

A range of aligned solidification microstructures is exhibited by the alloy when examined as-cast at room temperature: dendrites, flanged cells, cells. The microstructure transitions from cellular to dendritic as the growth velocity increases.

The experimental data for PWA1484 exhibits excellent agreement with the well-known exponential equation ($\lambda_1 \propto G^{-1/2} V^{-1/4}$). However, the constant of proportionality is different depending upon the solidification microstructure: (1) dendritic growth with secondary arms leads to a marked dependence of λ_1 on $G^{-1/2} V^{-1/4}$; (2) flanged cellular growth with no secondary arms leads to much lower dependence of λ_1 on $G^{-1/2} V^{-1/4}$.

The primary dendritic arm spacing results were also compared to recent theoretical models. The model of Hunt and Lu and the model of Ma and Sahm provided excellent agreement at medium to high thermal gradients and a wide range of solidification velocities. The anomalous behavior of λ_1 with high growth velocity V at low G is analyzed based on the samples' microstructures. Off-axis heat flows were shown to cause radial non-uniformity in the dendrite arm spacing data for low thermal gradients and large withdrawal velocities.

Various precipitates including γ', ($\gamma'+\gamma$) eutectic pool or divorced eutectic γ', and metal carbides were characterized. Processing conditions (growth velocity V and thermal gradient G) exert significant influence on both morphology and size of precipitates present.

Freckle defects were observed on the surface of nickel-based superalloy MM247 cylindrical samples but not on the surface of cylindrical PWA 1484 samples. The Rayleigh number (Ra) that represents liquid instability at the interface was evaluated for

MM247 and PWA 1484 in terms of a recently proposed theoretical equation. The effects

of segregation, sloped solid/liquid interface and the morphology of dendritic/cellular

trunks on the mushy zone convective flow and freckle formation are also discussed.

ACKNOWLEDGMENTS

The author would like to express his great gratitude to his advisor, Dr. Ruel A. Overfelt for his advice during the whole course of this study. He constantly provided invaluable suggestions and encouragement. The author would also like to extend thanks and gratitude to all members of the materials engineering faculty for their general assistance and help in conducting the research experiments. Finally, I offer special thanks to my wife Jianjun Zhang for her support and patience.

Style manual or journal used <u>Metallurgical Transactions A (American Society of Metal,</u>

<u>ASM International)</u>

Computer software used <u>Microsoft Word for MSOffice 98</u>

TABLE OF CONTENTS

LIST OF TABLES

LIST OF FIGURES

CHAPTER 1.

INTRODUCTION

1.1. Superalloys

The term superalloys refers to a class of materials with a combination of high strength, creep, thermal fatigue and oxidation-corrosion resistance, as well as microstructure stability at elevated temperature, i.e. 650°C and above[1~7]. Generally a superalloy is very complex, and often consists of eight or more atomic constituents. In terms of major constituents, there are iron-based superalloys, cobalt-based superalloys, and nickel-based superalloys. Some commercial nickel-based superalloys are listed in Table 1-1[5].

The high temperature properties of superalloys are determined by their unique microstructure. For example, nickel-based superalloys generally are comprised of austenitic face-centered-cubic (fcc) matrix phases (gamma phase, γ), ordered intermetallic precipitated particles (gamma prime, γ'), and other secondary precipitates determined by the chemistry of this alloy[1]. Among those phases, gamma prime γ' plays an important role in strengthening high temperature properties of alloys. γ' has a cubic ordered crystal structure as shown in Figure 1-1[8]. Nickel atoms occupy face-centered positions and aluminum atoms are at the corner positions. When external stresses are

1

Table 1-1. Nominal compositions of some commercial nickel-based superalloys[5]

	Ni	Al	Cr	Co	Ti	Mo	Ta	W	Re	Nb	Hf	Fe	B,C,Zr
IN 718	Bal.	0.5	19		0.9	3				5.1		9	minor
Waspaloy	Bal.	1.4	19	19.5	3	4.2							minor
MM247	Bal.	5.5	8.3	10	1	0.7	3	10			1.5		minor
CMSX-11B	Bal.	3.6	12.5	7	4.2	0.5	5	5		0.1	0.04		
SRR 99	Bal.	5.5	8.5	5	2.2		2.8	9.5					
Rene N6	Bal.	5.75	4.2	12.5		1.4	7.2	6	5.4		0.15		
PWA1484	Bal.	5.6	5	10		2	9	6	3				

Ni   AL
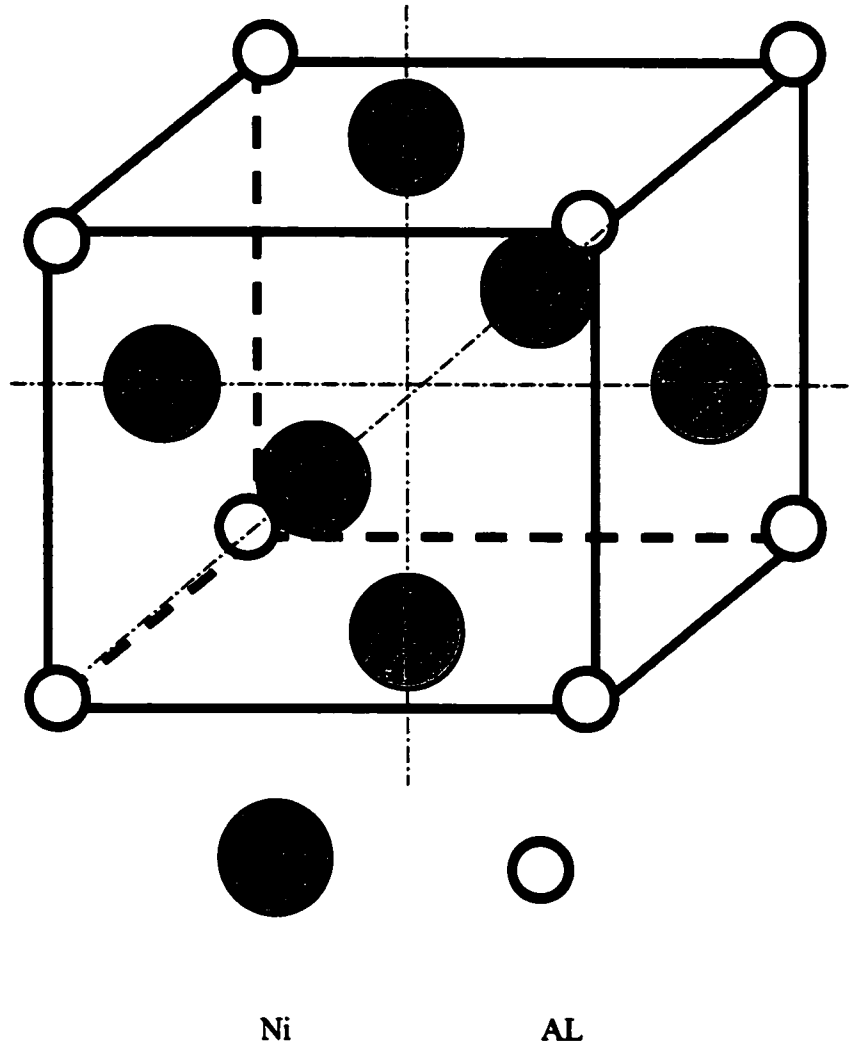
Figure 1-1. Ordered gamma prime phase (γ′) crystal structure with Ni atoms at face

centers and Al atoms at cube corners.

applied, dislocations can move readily through the γ matrix, but are pinned upon encountering γ′. When the dislocation lines penetrate into ordered γ′, the order of atomic structure (i.e. Ni-Al chemical bonding) will be disrupted and a high energy anti-phase boundary will be created[5,8,9]. Also, strengthening by γ′ relates to many factors, i.e. volume fraction and particle size of γ′. Previous researchers have shown that the higher volume fraction of γ′ there is in matrix, the greater the strengthening effects will be [5, 10~12]. Also the addition of refractory elements, i.e., W, Re, Ta, Hf, can significantly increase the matrix strength by lattice distortion (solid solution strengthening)[5, 6]. Those high melting point elements also provide strong lattice cohesion and reduce high temperature diffusion.

Superalloys, due to their unique high temperature properties, have a wide range of applications in the aerospace, power generation and chemical industries. Particularly in the manufacturing of aircraft turbine engine and industrial gas turbines (Figure 1-2), the application of components made out of superalloys has significantly expanded from 10% of total engine weight in the 1950s' to 50% in the 1980s', and reached 60% in the 1990s'[13, 14]. The continual drive for enhanced thrust and improved efficiency from gas turbines has led to a progressive increase in operating temperature, which, in turn, has pushed the development of new alloys and innovative process techniques for critical parts such as turbine blades. Directional solidification has been an important component of this development.
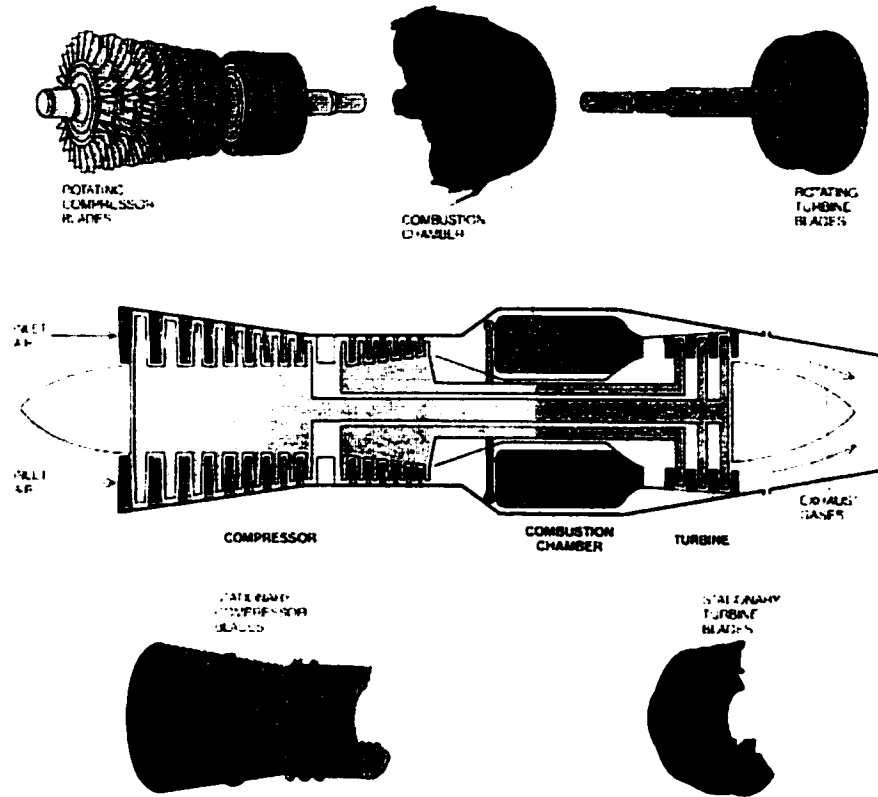
Figure 1-2 Assembly scheme of turbine engine components. Nickel-based and cobalt-based superalloys are employed in the production of turbine blades [8].

1.2. Directional Solidification and Single Crystal Investment Casting

Versnyder and co-workers at Pratt & Whitney[13] were the first to suggest using directionally solidified single crystal superalloys as structural components. Directional solidification (DS) can offer the following significant advantages[13, 15, 16] as high temperature structural parts in turbine engines:

a) Aligned crystal structure minimizes (polycrystalline) or eliminates (monocrystalline) the weak transverse grain boundaries that has been observed as sources for creep and thermal fatigue failures.

b) The low modulus <001> oriented growth texture provides significant enhancement in thermal fatigue resistance.

c) By minimizing or eliminating the boundary strengthening elements i.e., B, C, Zr, Hf, the solvus temperature could be increased and allow additional refinement of the as-cast γ′ leading to high creep strength.

Figure 1-3 illustrates a typical configuration of a directional solidification process. There are two major compartments, a hot zone and a cool zone separated by an adiabatic baffle insulator to minimize energy transfer between two zones. Initially, the casting mold sits inside the hot zone above the melting temperature. A chill plate cooled with water is designed for use at the bottom of the mold to ensure heat extraction from the bottom. Liquid alloy is then poured into the mold, and the mold is gradually withdrawn into the cool zone. Solidification proceeds in a directional manner as a consequence of the thermal gradient created between the upper hot zone of the furnace and the chill plate. In order to produce DS and single crystal castings free of defects, both casting parts and
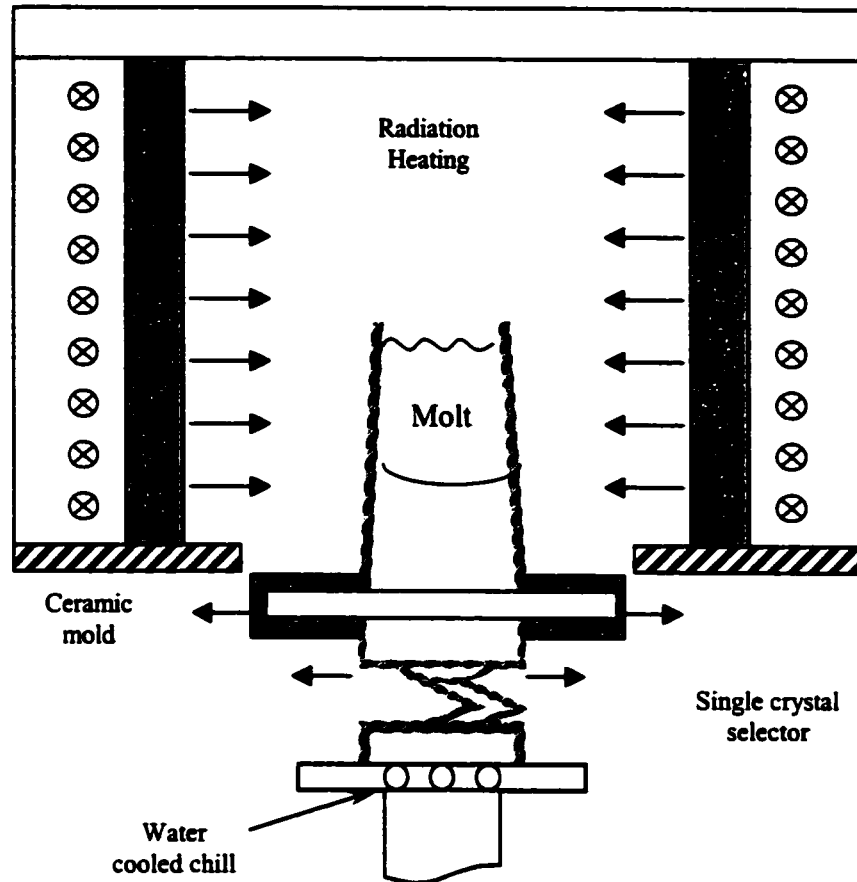
Figure 1-3 Schematic principle of directional solidification process with a single crystal

selector, utilized to cast DS and single crystal superalloy components

operating conditions (metal pour temperature, furnace temperature and withdrawal velocity) should be designed and controlled correctly. Sufficient heat must be extracted at the solidus interface by conduction into the solid so that the heat of fusion, ΔH, does not accumulate and alter the sign or direction of the thermal gradient G_s at the solidus.

1.3. DS and Single Crystal Casting Defects

Directional solidification techniques require stringent process controls to avoid the formation of extra grains and their deleterious grain boundaries. Understanding the interrelationships among the many process parameters of casting geometry, alloy composition, thermal field, and growth rate is required to obtain satisfactory grain structures. Unfortunately, the many physical phenomena affecting grain formation during directional solidification are interrelated in a complicated fashion and only qualitatively understood. These phenomena combine to induce several kinds of defects, such as spurious equiaxed grains, porosity, channel segregates, and freckles, which cause high scrap rates for the production of many components.

Channel segregates in the interior of castings and freckle chains along the exterior of castings are meandering lines of defects composed of small randomly-oriented equiaxed grains, second phase particles, porosity and the defects enriched with the eutectic composition[17]. An example is shown in Figure 1-4. After macroetching, freckle chains appear at the outside surface of shaped castings with defect trails in the direction anti-parallel to gravity. Freckle grains obviously weaken the high temperature creep resistance of directionally solidified components due to the transverse grain
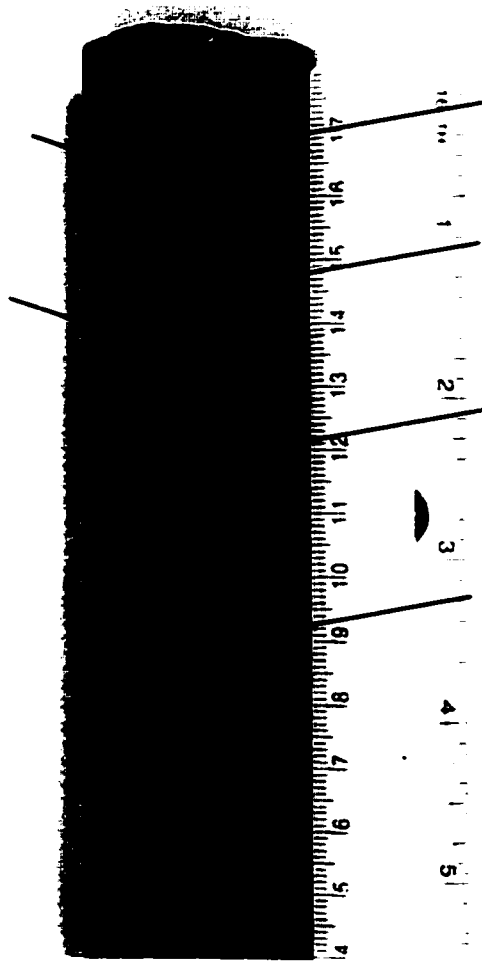
Figure 1-4. Typical freckle defects on the surface of a directionally solidified elliptic

cylinder sample of PWA 1484 superalloy (as pointed by arrows)

boundaries and the local composition of low melting point eutectic[13].

In the past two decades, significant research has been reported on channel segregation phenomena. However, many investigations have been based on low melting point model systems: organic analog solutions of NH_4Cl-H_2O[18,19] and simple binary metallic Pb-Sn alloys[20-24]. These investigations have contributed to an improved qualitative understanding of the mechanism of channel segregate/freckle formation. (Hereinafter, only the simpler term of 'freckles' will be used.). Unfortunately, freckles remain a common and serious manufacturing defect in many directionally solidified alloy systems of commercial importance[25]. Additional research on the physical phenomena influencing freckle formation in high melting point commercial alloys is required to establish quantitative relationships that will enable rigorous design and control of the solidification parameters. The research described in this document defines the processing-microstructure relationships for the commercial superalloy PWA 1484, and is intended to decouple some of the complex microstructural interrelationships affecting freckle formation in PWA 1484. In addition, this work will help establish a quantitative understanding of the freckle formation mechanisms in this important alloy.

CHARTER 2.

REVIEW OF RESEARCH LITERATURE

2.1. Microstructural Development During Directional Solidification

Microstructure characterization is an important aspect of materials science and engineering since it is the strategic link between materials processing and materials behavior. A quantitative understanding of materials development is necessary in making decisions of processing activity and obtaining desired materials performance.

Microstructures of directionally solidified superalloys can be varied widely. In terms of morphologies at the growing interface, the typical microstructures include planar interface, cell, dendrite, and equiaxed grain (Figure 2.1). Although nickel-based superalloys are very complex with eight or more atomic constituents, the solidification behavior can be understood with the solidification mechanism for simple binary alloys.

It is well known that, during solidification of many alloys, solute atoms are rejected from the growth interface and pile up forming a solute-rich boundary layer ahead of the growth front. The change in concentration modifies the local equilibrium liquidus temperature T_L which could be described by the equation first derived by Tiller and Chalmers[26]:

$$\frac{dT_L(C_0)}{dz}\bigg|_{x=0} = -\frac{mC_0(1-k)V}{kD_L} \qquad (2.1)$$
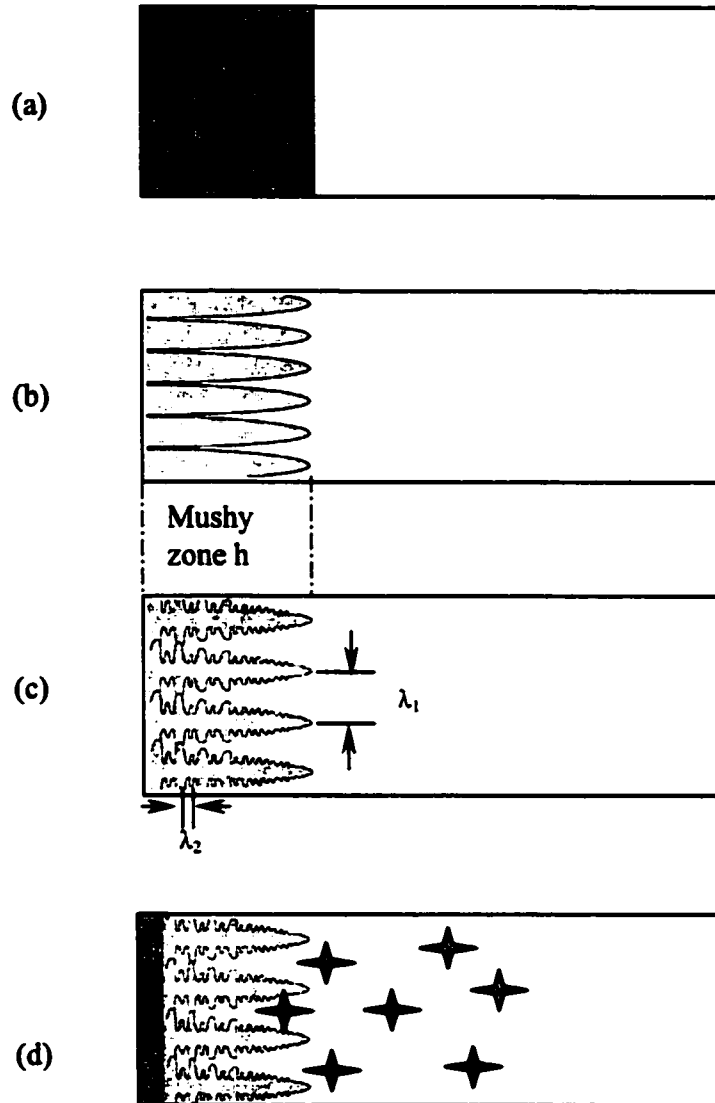
Figure 2-1. Four types of growing fronts of directional solidification process: (a) planar interface, (b) cellular structure, (c) dendrites with of λ_1 and λ_2 identified, and (d) equiaxed grains in front of growing mushy zone.

which leads to the critical condition for obtaining stability of a planar interface:

$$(\frac{G_L}{V})_{cri} = \frac{mC_0(1-k)}{kD_L} = \frac{\Delta T}{D_L}$$

(2.2)

where $T_L(C_0)$ is the liquidus temperature corresponding to the initial alloy composition (C_0), and m is the slope of the liquidus. k is the partitioning coefficient of solute element. z is distance from freezing interface. As shown in Figure 2-2, the actual temperature profile in the liquid (T_q) imposed by the heat flux at the growth interface may not match the equilibrium liquidus temperature profile $T_L(z)$. If T_q is higher than $T_L(z)$, any perturbation from a flat S/L interface will not be stable and the growth front will remain with a planar interface (Figure 2-1(a)). If T_q is lower than that of $T_L(z)$ at the growth interface, there will be a zone of constitutional supercooling and any perturbation to the interface will be stable and will grow into cells or dendrites (Figure 2-1(b,c)). As a result of the constitutional supercooling zone, the growth front will be a zone with both liquid and solid phase. This area is referred to as the mushy zone.

Figure 2-3[28] summarizes reported data on the morphological transition of several directionally solidified superalloys between planar interface, cellular and dendritic microstructures. It shows that, when actual G/V increasingly deviates below the critical (G/V) for planar growth, a progression of microstructure forms as cellular, cellular/dendritic, dendritic and even equiaxed grains. Also there is a sharp boundary between planar interface and cellular microstructure, and this boundary line has been shown to be consistent with Equation 2.2. However, the transition between cellular and dendritic is not a distinct boundary but a transition band. Also there is no quantitative
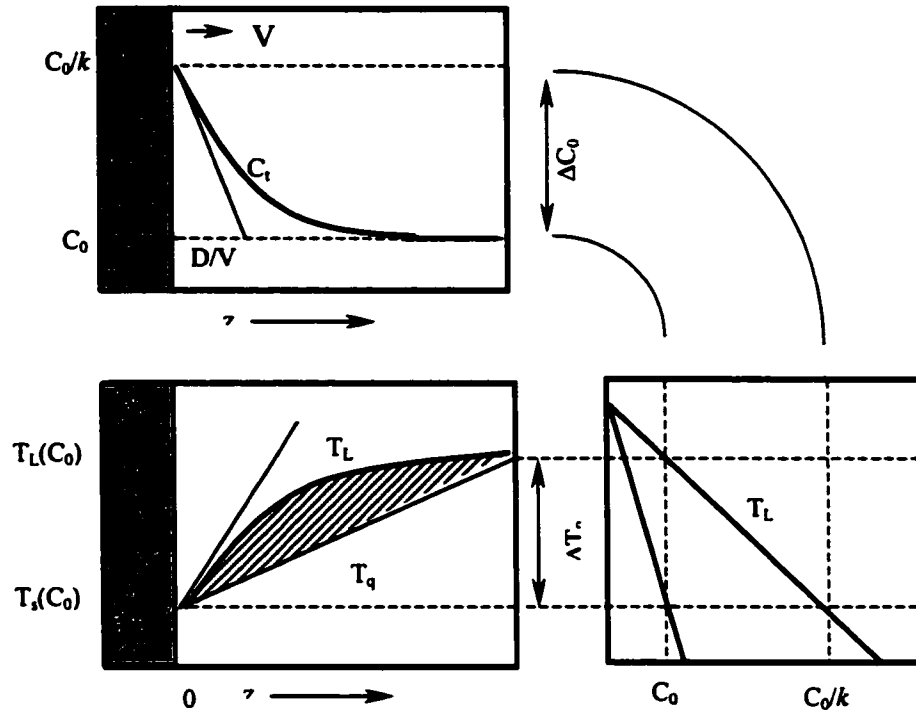
Figure 2-2. Constitutional supercooling formation mechanism

ahead of freezing front in alloys[27]
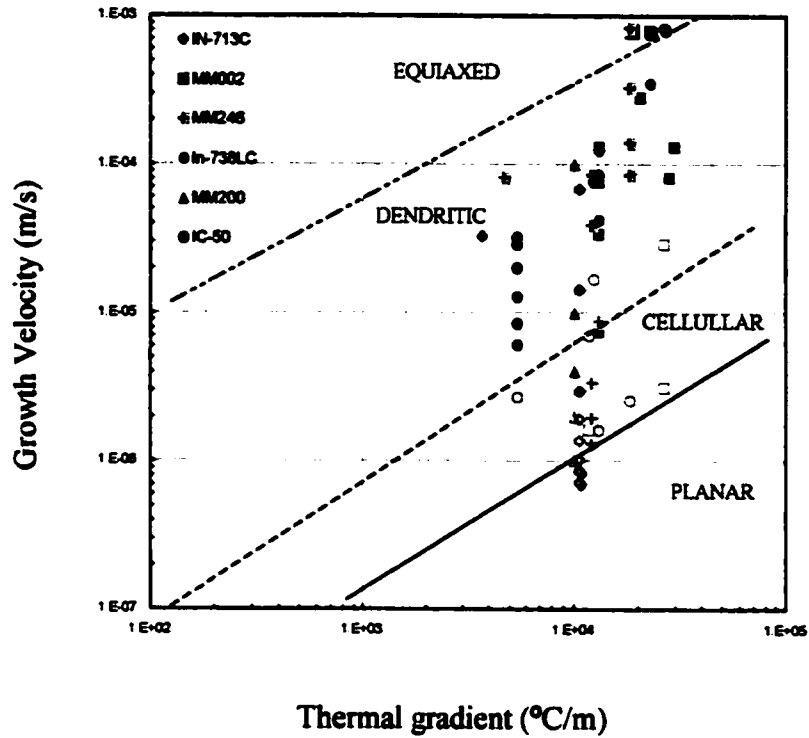
Figure 2-3. Morphologies of directionally solidified nickel base superalloys mapped on a plot of logV vs. logG. The lines in the map are boundaries defining the various zones (shadow marks at lowest V: planar interface; empty marks: cellular structure; solid marks: dendrite; solid shadow marks: equiaxed)[28]

relationship to theoretically define the transition between cell and dendrite, corresponding to the difficulty of physically identifying the microstructure at transition points between the two morphologies. More work is needed to quantitatively establish this solidification map to benefit industry in selecting appropriate process conditions.

2.2 Dendritic/Cellular Arm Spacings

The average spacing between the primary dendrite arms is termed λ_1 or simply PDAS and the average spacing between the secondary arms is λ_2 or SDAS . The dendritic/cellular arm spacings of directionally solidified materials are very important microstructural features that impact mechanical properties of solidified products[16]. Also the spacing and morphology of arms directly influence convection in the mushy zone and dominate the occurrence of grain defects, freckle/channel segregates and porosity in the microstructure[20, 29,30]. Thus the variation of primary dendritic/cellular arm spacings during directional solidification has been intensively studied[28, 31~36]. Although the fundamental phenomena of microstructure development and transition are qualitatively understood, there is still work required to quantitatively describe multi-component systems, growth with mis-aligned thermal fields, and growth during transient thermal conditions.

Previous researchers have developed several empirical and theoretical expressions to relate λ_1 with the variables of alloy composition (C_o) for simple binary alloys and the applied solidification parameters, i.e., thermal gradient (G) and growth rate (V). Early

experimentalists[37-39] correlated λ_1 and λ_2 with the solidification time (t_f) or cooling rate (GV) imposed during solidification. Thus

$$\lambda_1 = m_1 (t_f)^n = m_2 (GV)^{-n} \qquad (2.3a)$$

$$\lambda_2 = m_3 (t_f)^q = m_4 (GV)^{-q} \qquad (2.3b)$$

where $m_1 \sim m_4$ are simple constants.

Hunt[40] developed the first theoretical formulation to predict dendrite arm spacings based upon the imposed process parameters. In Hunt's model, several assumptions were invoked to simplify the treatment: 1) the thermal and compositional gradients in the direction parallel with the growth direction were constant; 2) the tip of the dendrite or cell was a steady parabolic shape; and 3) the cell or dendrite grew at the minimum undercooling for a given growth velocity (or maximum growth velocity). Hunt's model resulted in a relationship of the form:

$$\lambda_1 = \{2.83(\frac{\gamma D}{\Delta S})^{\frac{1}{4}}[m(1-k)C_0 + \frac{kGD}{V}]^{\frac{1}{4}}\}G^{-\frac{1}{2}}V^{-\frac{1}{4}} \qquad (2.4a)$$

or $\quad \lambda_1 = 2.83(k\Delta T_0 \Gamma D)^{\frac{1}{4}}G^{-\frac{1}{2}}V^{-\frac{1}{4}} \qquad$ when $\quad GD << V\Delta T_0 \qquad (2.4b)$

The first term in the braces { } is a combination of material constants for a given alloy. γ is the alloy solid-liquid interfacial energy, ΔS is entropy of fusion per unit volume, D is the solute diffusion coefficient, m is the slope of the liquidus, k is the solute distribution coefficient and C_0 is the alloy composition. G and V are the thermal gradient and growth velocity at the dendrite tip, respectively.

Two years later Kurz and Fisher[41] published a modified theoretical model utilizing the stability criterion proposed by Langer and Muller-Krumbhaar[27]. In addition, Kurz and Fisher assumed that the tips of the cells/dendrites were smooth ellipsoids, and cells/dendrites form uniform hexagon arrays. Thus, Kurz and Fisher obtained the following results for cells and dendrites:

$$cells: \quad \lambda_1 = [\frac{6\Delta T'}{G(1-k)}]^{\frac{1}{2}}[\frac{D}{V} - \frac{k\Delta T_0}{G}]^{\frac{1}{2}} \tag{2.5}$$

$$dendrites: \lambda_1 = \{4.3[\frac{\Gamma D\Delta T_0}{k}]^{\frac{1}{4}}\}G^{-\frac{1}{2}}V^{-\frac{1}{4}} \tag{2.6}$$

where Γ is the Gibbs-Thomson coefficient and $\Delta T'$ and ΔT_0 are the non-equilibrium and equilibrium freezing ranges, respectively. As in Hunt's previous model, the first term in the braces { } for both cells and dendrites is an alloy dependent constant. For dendritic growth, even though Hunt and Kurz/Fisher applied different arguments, very similar expressions for dendritic growth were obtained. In fact, the only difference was in the derived alloy dependent constants.

Although overly simplistic, these two analytic models provide excellent insight into the growth mechanisms and qualitative agreement with experimental data. More exacting models are now under development. Hunt and Lu[42, 43] have reported predictions of spacing from time dependent finite-difference models of solute transport during array growth of cells and dendrites. Fully self-consistent solutions were produced for axi-symmetric interface shapes for well-aligned growth conditions. The analytic relationship of the results of the numerical models is:

$$\lambda_1 = 0.156(\Gamma k)^{a_d+0.4} D^{-a_d} \Delta T_0^{-a_d+0.2} (1-\frac{V_c}{V})^{\frac{3}{4}} G^{-0.6} V^{a_d} \qquad (2.7)$$

with $\qquad a_d = -1.131 - 0.1555 \log_{10}(\frac{G\Gamma k}{\Delta T^2}) - 0.76 \times 10^{-2} [\log_{10}(\frac{G\Gamma k}{\Delta T^2})]^2$ $\qquad (2.8)$

V_c is the critical velocity where the interface will break down from a planar to a cellular

structure and a_d is a gradient dependent exponential factor and established from

numerical analysis. An important feature of the numerical approach was that the spacing

selection mechanism was incorporated and no *a priori* assumptions were required

(marginal stability, minumum undercooling, etc.). The critical spacing was considered

achieved when the composition along the cell groove was nearest in composition to the

equilibrium composition line. A principal result was that spacing deviations below the

critical array spacing lead to overgrowth. Although the model was originally set up for

cells, it was extended to dendritic growth when it appeared to provide reasonable

predictions for dendritic structures. Finally, Hunt and Lu's model did not consider the

effect of secondary arms or of possible transverse thermal gradients.

Recently, Ma and Sahm[44, 45] proposed a new analytic model to explain the

variation in primary arm spacing with growth velocity and specifically included the

effects of secondary arm growth on primary dendrite arm spacing. Ma and Sahm's

analysis concluded that:

$$\lambda_1 = 2\pi(kD\Gamma \Delta T_0)^{\frac{1}{4}}(1-\frac{V_c}{V})^{\frac{3}{4}} G^{-\frac{1}{2}} V^{-\frac{1}{4}}. \qquad (2.9)$$

In this model, dendritic growth was resolved into 2 parts - growth of center core

and growth of side arms. The arm spacings are considered to be the sum of the dendrite

core diameter and twice the sidearm length. The dendritic core diameter was directly related to dendrite core tip radius R. The side arm length was determined by local free growth time and growth velocity until encountering the neighboring arms. The side arm tip radius was assumed to be equal to the primary tip radius and the side arm growth velocity was assumed to be equal to the primary growth velocity (for dendritic growth only). Transverse (i.e., radial) thermal gradients were assumed to be negligible. This model gave a reasonable dependence of cellular/dendritic spacing on the process parameters. Ma and Sahm tested their model and the Hunt and Lu model against experimental data of λ_1 vs. V for directionally solidified succinonitrile-0.35 wt. pct. acetone, SRR99 superalloy and Pb-Ti alloy and found that their model gave better agreement.

The ability of mushy zone microstructures to adjust to non-aligned growth conditions and transient solidification conditions is becoming of increasing interest. Han and Trivedi[31] investigated the primary dendrite spacing adjustment process in succinonitrile-acetone after sudden increases in velocity and proposed there is a range of stable spacings associated with specific values of G and V, rather than a unique spacing. Eshelman et al[102] studied the variation in average cellular spacing with velocity and observed that there was a finite band of velocities in which both cellular and dendritic structures were stable. Bouchard and Kirkaldy[46] summarized work on a large number of binary metal systems and found the exponents on G and V in Eqs. (2.4, 2.6) to be generally -0.3 to -0.5 and -0.1 to -0.39, respectively, and proposed that the difference between the measured exponents and the theoretical exponents (-0.5 and -0.25,

respectively) were mainly due to convection effects. Su et al[47, 48] found that although the primary and secondary dendrite arm spacings in Al-4.5 wt. pct. Cu adjust quickly to increases in imposed velocity, the compositional profiles adjust more slowly.

Growth when the dendrites are mis-aligned with the thermal gradient was examined in succinonitrile-water alloys by Grugel and Zhou[49]. The primary dendritic arm spacing in SCN-H$_2$O alloys were measured as a function of growth velocity and orientation angle with respect to the applied temperature gradient. The spacings were found to increase with the angle from 0° to 45° deg at constant composition, growth velocity and thermal gradient G$_L$. Grugel and Zhou postulated that the increase in primary spacing was due to an increase in side arm growth velocity from the off-axis thermal gradients.

While the effects of V and G on primary arm spacings have been extensively investigated with simple binary alloys, experimental data on high melting point multi-component alloys, particularly at very low thermal gradients consistent with production conditions, are limited. The present experiments were designed to investigate the cellular and dendritic solidification behavior of the multi-component Ni-base superalloy PWA 1484 over a wide range of imposed solidification velocities V and thermal gradients G.

Secondary arm spacing also is an important microstructural feature for DS alloys. Secondary arm spacing λ_2 has been shown to depend on the local solidification time and cooling rate[52] for a wide variety of alloys and that λ_2 develops by a coarsening process. The coarsening may be due to the process of dissolution of smaller arms with sharper tip radii and growth of large arms with less curvature. Alternatively a process of separation

of the secondary arms by "pinching off" of the neck has also been proposed[53].

Evidently, an inverse cube root relationship of λ_2 with cooling rate appears

satisfactory[46]. In addition, secondary arm spacing would affect the transport phenomena

ahead of the growth front significantly. Poirier *et al*[50, 51] stated that the permeability in

the mushy zone was strongly dependent on the secondary dendritic arm spacing (λ_2) as

well as λ_1 when the convective flow was normal to the primary dendritic arms.

2.3 Various Precipitate Phases in DS Superalloys

High temperature mechanical properties of superalloys stem from the various

precipitates, i.e. ordered γ' and carbides, that act as barriers to deformation. The nature

and distribution of those phases in castings are directly dependent upon the solidification

conditions.

Precipitation of γ' is one of the most important reactions in nickel-based

superalloys. γ' precipitates are face-centered-cubic (f.c.c.) ordered $Ni_3(Al, Ti)$ type

intermetallic compounds in superalloy. It is well known that the precipitation of γ' in the

γ matrix is a continuous process of nucleation, growth and ripening[3,6,7,11]. γ' precipitates

from γ matrix to relieve the over-saturation of the solid solution. The morphology of γ'

precipitate has been shown to progress from spheres, to cubes, to octet cubes and large

irregular geometry patterns[54].

The morphological change of γ' precipitates is governed by the thermodynamic

forces, and elastic distortion energy from the lattice mismatch between matrix γ and

precipitates γ' [54, 55, 56]. The distortion energy associated with the solute size differences

will drive the γ' to precipitate and grow. At the initial stage of precipitation, the

interfacial energy dominates, and hence precipitates exhibit a spherical shape. As γ'

precipitates grow, the elastic energy contribution increases. Because the <001> growth

directions have the lowest elastic constants, the cubic morphology of γ' precipitates is

favored. The octet cubes result from splitting of single cube and this configuration has

been shown associated with a lower elastic distortion energy than that of any other

morphology. With the further growth of γ' precipitate, the neighboring cubes coalescence

into the bigger irregular shaped particles, and lose its coherence with γ matrix. Dendrites

of γ' have also been observed in some superalloys.

The cooling rates during and after solidification play an important role in the

morphology and size of γ' precipitates [57~59]. The high cooling rate and large super-

cooling causes high nucleation density with uniform and fine sized precipitate

configuration. In addition, high supercooling creates $\gamma+\gamma'$ eutectic pool, nucleated directly

from melt [58, 60~63]. $\gamma+\gamma'$ eutectic pool usually grows at locations such as grain boundaries

or interdendritic regions. In contrast, under a low cooling rate, there is a lower nucleation

density and longer active growth time. The precipitates were observed to grow to larger

sizes. Both $\gamma+\gamma'$ eutectic pool and divorced eutectic γ' are highly undesirable since they

retain a large amount of alloying elements that otherwise could have strengthened the

solid solution matrix. In addition, the $\gamma+\gamma'$ eutectic will decrease the incipient melting

temperature and make solution heat treatment more difficult or impossible [5, 7].

Numerous experimental results of nickel-based superalloys on the mechanical properties[5, 7, 10~12, 64] have shown that the morphologies of γ' precipitates have significant effect on the mechanical properties. When the volume fraction of γ' is around 70~80% with a size of about 0.5 μm, the creep-rupture and hardness could reach a maximum[5,10]. As the size of γ' precipitate increases towards the optimum size, the strengthening increases since anti-boundary energy is raised when dislocations cut through ordered γ' precipitates. When γ' continues to grow and lose the coherence with γ matrix, the effect of strengthening is weakened since dislocations could bypass γ' precipitates easily[11, 65~67].

Metal carbides (MC) are another common constituent in nickel-based superalloys. MC provide enhanced creep-rupture resistance for nickel-based superalloys with equiaxed grain microstructures [13, 63, 68]. However directional solidified and single crystal Ni-based superalloys have minimum or no grain boundaries. Thus there is no need of the grain boundary strengthening by carbides. Furthermore, experimental results show that the fatigue life varies inversely with MC size[4, 66, 69], and a continuous network of script carbides drastically reduces the ductility of an alloy by facilitating crack initiation and propagation. Therefore, the morphology of small uniform and equiaxed carbides are preferred in superalloys.

Numerous research works [63, 68~72] have investigated the effects of solidification variables on the morphology of carbides. It is well known that the near-equilibrium morphology of MC in superalloys is octahedral blocks, and the blocky morphology

gradually transitions to script with a finer size as carbide growth rate increases. In the as-cast conditions, carbides are usually of the MC type, where M is Ta, B, Zr, Ti or Mo[68,73]. Chen et al [69, 73] studied MC carbide formation in DS MM247 LC Ni-based superalloy. The results indicated that MC morphologies and chemistry were determined by the MC growth rate, MC forming element segregation and surrounding solid geometry. Sun et al [74] stated that the γ+MC eutectic reaction was an important factor to determine the MC morphology. It was found that high solidification rate causes the quasi-eutectic reaction of γ+MC, and increases the number of MC; script MC formed at medium rate due to significant segregation in the residual liquids; at low rates of cellular or near-plane interface growth, eutectic reaction of γ+MC took place again.

2.4 Segregation Effects in DS Nickel-base Superalloys

Giamei and Kear[17] pioneered the investigation of freckle formation in several nickel base superalloys and reported on spurious grain locations, freckle chain morphology, composition and microstructure. The local composition in the freckle chain was found to be close to the eutectic composition. When remelting samples with freckles at temperatures just above the solidus, the freckle chains would melt and drain first. These researchers concluded that the freckle chains were rich with solute from the solute rejected during dendritic growth and were probably the last region to solidify and form their inhomogeneous structure. Giamei and Kear proposed that freckles were related to the imposed solidification parameters (thermal gradient, growth rate and size of castings) as well as the alloy's specific composition.

Research on freckle formation has been conducted in three primary ways: (1)

solidification of analog alloys like aqueous ammonia chloride[18,19, 20] ; (2) solidification

of metallic alloys including simple binary Pb-Sn and complex superalloys[24, 29,30,75-79],

and (3) simulation of the solidification of alloy systems (Pb-Sn, NH_4Cl-H_2O, and recently

Ni-base superalloys) by computational models[80-89].

Since the analog alloy solutions are transparent, the solidification process can be

directly observed providing significant intuitive insight into the phenomena. Through

directly observing unidirectional solidification of samples of of ammonium chloride

solutions (30% NH_4Cl-H_2O), Copley and Giamei[18] found that freckling of the analog

alloy was initiated by the upward flow of convective jets caused by a density inversion in

the microsegregated, solute rich mushy zone. The mechanism is shown schematically in

Figure 2-4. The jets coming from the bottom of the mushy zone were observed to erode

the mushy zone by dissolution and fragmentation of dendrites. It was suggested that

these dendritic fragments served as the nuclei for the equiaxed grains found in freckle

chains. After solidification was completed, the jets formed the as-cast freckle trails. A

parameter $\Delta\varphi$ was derived to predict the effects of solidification variables on the freckle

formation probability:

$$\Delta\varphi = \frac{g\,\beta_c\Delta T_0\Delta C\Delta\rho}{6\,\beta_T G^2} \qquad (2.10)$$

where β_c and β_T are the volume coefficients for thermal and compositional expansion,

ΔT_0 is the equilibrium freezing range, ΔC and $\Delta\rho$ are composition and density

differences between the segregated and bulk liquids, G is the thermal gradient and g is

gravity. Eq. (2.10) shows that a high interdendritic density inversion ($\Delta\rho$) and low

thermal gradient (G) would increase $\Delta\phi$ and favor freckle formation. In Ni-Al and Ni-Ta

binary solidification experiments[17], the Ni-Al alloy was more prone to form freckles

than Ni-Ta alloy due to the significant density inversion from aluminum partitioning.

In separate research on the transparent analog NH_4Cl-H_2O, Hellawell *et al*[19,20]

also observed the convective jet (plume) in the bulk liquid and noticed that there is a

micro-segregation channel formed below the upwardly flowing plumes. These channels

originate, not within the dendritic array at any depth, but immediately ahead of the

growth front as a result of a perturbation of the less dense boundary layer into the bulk

liquid. Perturbations that develop into solute plumes in the bulk liquid would be

maintained by entraining the solute rich liquid in the mushy zone below the plumes, as

shown schematically in Figure 2-4. Solute rich liquid would locally depress the liquidus

temperature and remelt the local dendrites to form the open channels in the mushy zone.

Furthermore, Hellawell *et al* characterized the effects of thermal gradient, growth rate,

dendritic spacing, and interdendritic permeability on channel formation and correlated

those variables with the Rayleigh number (ratio of buoyant driving force to viscous

retarding forces within mushy zone) to determine a critical Rayleigh number of plume

nucleation occurrence. Thus

$$Ra = \frac{g\rho h^4}{\eta\kappa}(\beta_c \frac{dc}{dz} - \beta_T \frac{dT}{dz}) \qquad (2.11)$$

The first term in parentheses is the destabilizing factor related to the density

inversion (i.e., solutal gradient times the volume expansion coefficient due to

Freckle Defects Originate due to Convective Instabilities

The potential for convective instabilities can be
described by the combined Rayleigh Number
(ratio of buoyant to viscous forces):

$$Ra = \frac{\delta^3 \rho \, g}{\mu} \left(\frac{\beta_T \Delta T}{\alpha} + \frac{\beta_c \Delta C}{D} \right)$$

$$\delta = \frac{D}{v}$$
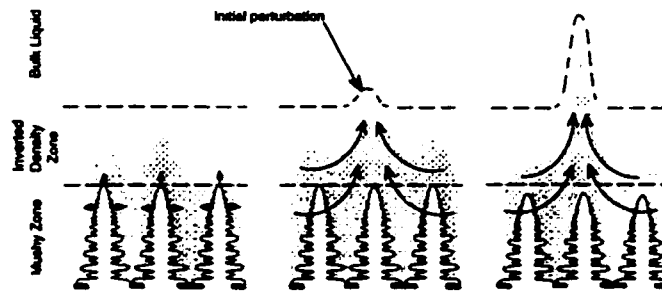
after
Sample and Hellawell(1984)
Sarazin and Hellawell(1988)

Figure 2-4. Casting defect freckling mechanism for lighter solute-rich segregation at

growth front proposed by Copley and Hellawell[19]

composition). The second term in parentheses is normally stabilizing (thermal gradient times the coefficient of thermal expansion) since hotter, lower density liquid exists in front of the mushy zone. Thus, normally segregating low-density solutes, or inversely segregating high density solutes, or low thermal gradients would all increase the value of Ra number and increase the tendency for freckle chains.

Tewari et al[24,29,75] investigated the effects of primary arm spacing and mushy zone length on the macrosegregation of Pb-Sn alloy during unidirectional solidification. Their results showed that increasing the primary arm spacing raised the extent of macrosegregation and favored freckle formation. Presumably this was because when the dendrite arm spacing is large, the permeability of the mushy zone is large and convection through the dendritic mush is easy. Tewari et al noted that more systematic experiments were necessary to investigate the detailed relations between primary arm spacings and freckle formation.

Heinrich et al[81,82,83] developed a computer model to simulate the unidirectional solidification of alloys with all-liquid region above a two-phase mushy zone possessing a lower density liquid phase. The results showed that there were two separate convection cells: one in the all liquid region and one counter-rotating cell in the mushy zone. The convective cell in the bulk liquid was normal buoyancy flow due to the radial thermal gradient. This cell can entrain the interdendritic liquid in the mushy zone and facilitate the development of thermosolutal plumes. The steady-state computational results showed liquid plumes emanating from within the mushy zone. After solidification, such plumes should exhibit freckle segregate phenomena. This result was in excellent agreement with

Hellawell's aqueous ammonium chloride solidification experiments. Unfortunately, Heinrich *et al* did not discuss the expected effects of the important solidification parameters such as thermal gradient, growth rate, crucible size, geometry and sample orientation, etc.

Recently Beckermann *et al*[90,91] developed a 2D computational model to simulate the formation of macro-segregation and freckles caused by multi-component thermosolutal convection during the directional solidification of Ni-based superalloy. It was concluded that the model provided a valuable tool in predicting freckle defects in DS of Ni-based superalloys. The Rayleigh number was again proposed to act as criterion to predict the probability of freckle segregates:

$$Ra_h = \frac{(\Delta\rho / \rho_0)g\overline{kh}}{\alpha v} \qquad (2.12)$$

A critical value of Rayleigh number of approximately 0.25 was found based on experimental data of one directionally solidified nickel-based superalloy. However, the authors pointed that additional experimental data were highly desired for different superalloys to further validate the proposed Rayleigh number criterion. The numerical model also showed that the probability of freckle formation would be doubled if the orientation of the mushy zone were tilted 10° with respect to gravity.

In order to establish a numerical criterion to predict the freckling onset conditions, Auburtin *et al*[76, 77] conducted directional solidification experiments on seven types of nickel-based superalloys, i.e., CMSX-11B, RENE88, NIM80A, WASPALOY, MM247 and a variation of IN718, at various angles to the vertical. The results showed that, under

similar solidification conditions, tilted castings exhibited freckles, whereas vertical castings were freckle-free. They also developed a modified Rayleigh number equation for predicting freckling conditions and ranked the order of freckling tendency from the highest probability as IN718, NIM80A, MM247, CMSX-11B, RENE88, WASPALOY. The approximate criterion values for the investigated Ni-base alloys were estimated to be 0.65~0.95. In addition, the composition analysis showed that the freckle chains might actually have a higher density than the bulk liquid.

James et al[79] also reported a high concentration of heavier element segregated to freckle chains in the study of the remelting processes for VAR (vacuum arc remelting) ingot 718 and ESR (electro slag remelting) ingot 625. In this case, in contrast to the phenomenon observed at model-alloys and Pb-Sn alloy, the channel liquid has higher density and tends to flow downward and to form freckle chains (Figure 2-5).

Pollock et al[30,78] conducted a wide range of directional solidification of multi-component single crystal superalloys to study the breakdown of single crystal growth. The results suggested that it was thermo-solutal convection promoting the breakdown of the single crystal structure as well as grain defects of mis-oriented columnar grains and freckles. As shown in Figure 2-6 from Pollock[78], the tendencies for mis-oriented columnar grains and freckles were seen to significantly increase when the primary dendrite arm spacing increased above approximately 320 μm. Pollock et al found that the nature and amount of solute played important roles in the formation of freckle segregates.
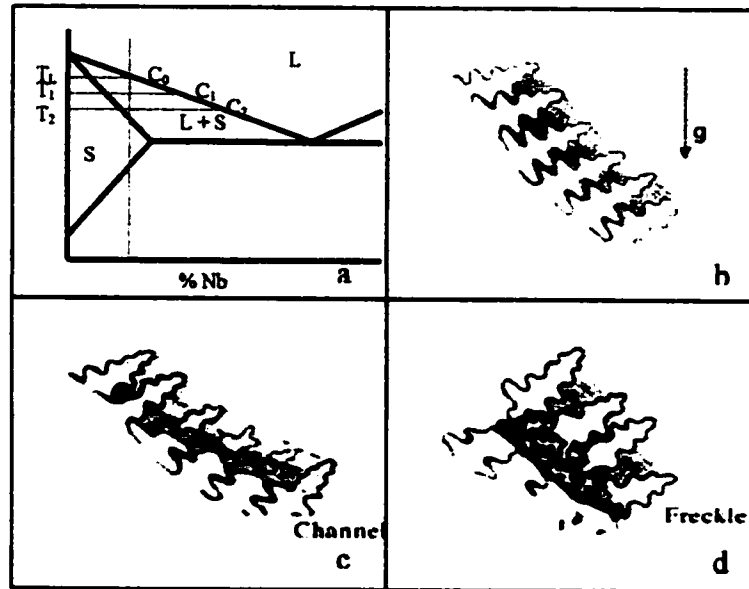
Figure 2-5 Freckle formation mechanism for denser solute-rich condition in the VAR and

ESR ingot nickel-based superalloys[79]
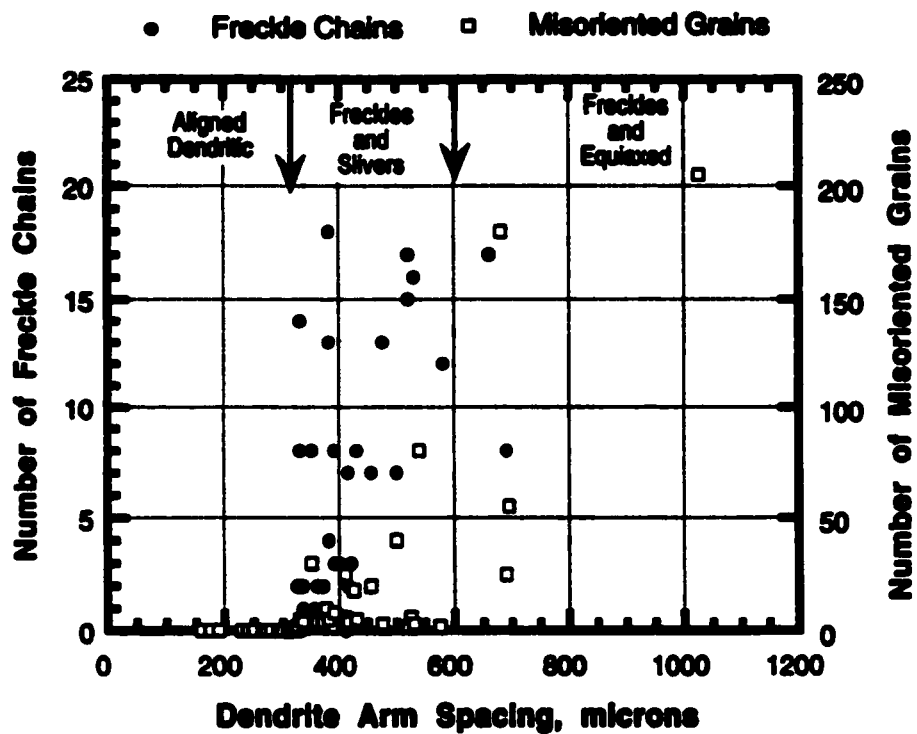
Figure 2-6 The effects of primary arm spacings on the freckle formation on DS SX-1

nickel-based superalloy[78]

In summary, all the previous investigations showed that freckle segregates are related to the upward or downward convective flow in the bulk and mushy zone liquids. Many variables can influence the convection, segregation and microstructural development during solidification, e.g.,

(1) Compositional Effects (C_0, k, β, α, η)

(2) Solidification Effects (G and V)

(3) Crucible Geometry and Orientation Effects

These variables are clearly interrelated but can be classified as two types: alloy variables (composition of alloy, solute partitioning, density inversion, and the thermophysical properties of the liquid alloy) and process variables (thermal gradient, growth rate, crucible diameter, crucible orientation, dendritic arm spacing, etc.). These variables will determine the microstructure during and after solidification and the propensity for the development of segregation defects. Figure 2-7 shows a schematic of the directional solidification process and the relevant non-dimensional parameters that are believed to control convection and freckle formation phenomena. A large number of experiments utilizing many alloy systems will be required to fully quantify the relationships among the dimensionless variables shown.
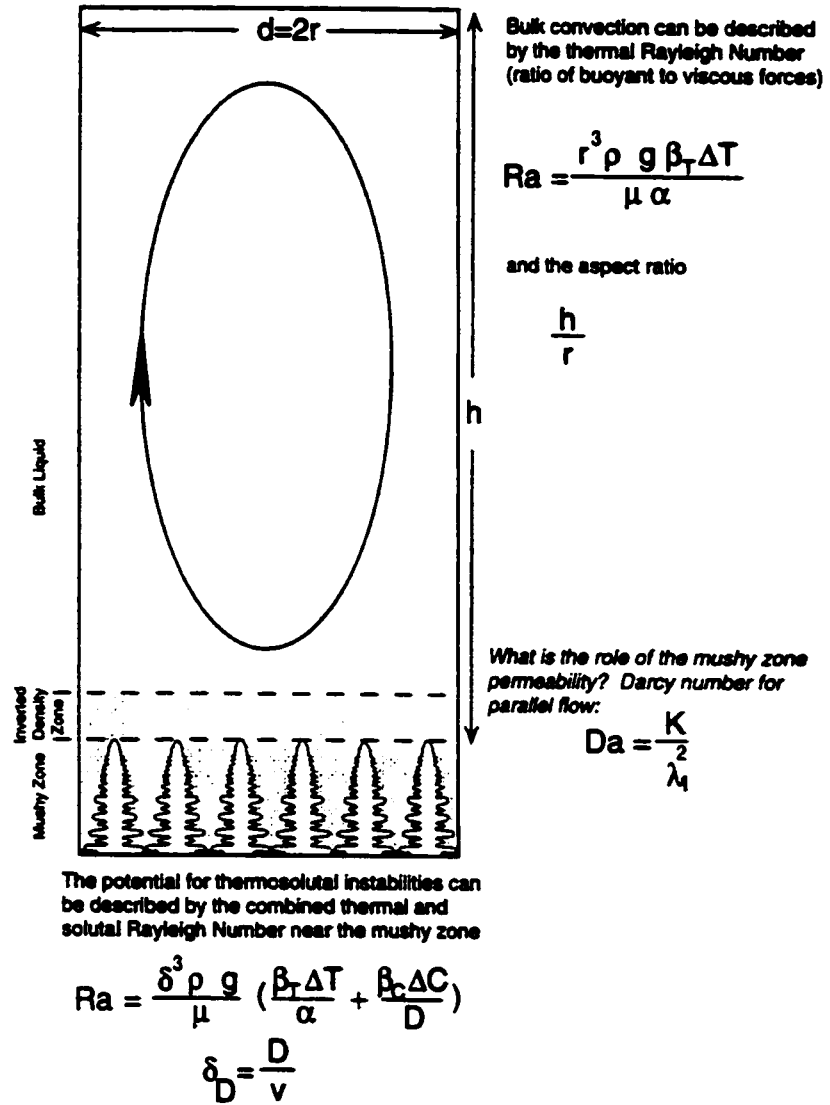
Figure 2-7. Dimensionless parameters related to convective flow inside mushy zone and

bulk liquid ahead of solidification front

CHAPTER 3

RESEARCH OBJECTIVES

The objective of this research are summarized as:

(1) To quantify the directional solidification parameters' effects on the microstructural development of an important engineering multi-component superalloy PWA 1484, by analyzing thermal gradient G and growth velocity V effects on development of the primary dendritic arm spacings and precipitate formation behavior.

(2) To experimentally investigate freckle formation mechanisms in the alloy PWA 1484 and evaluate the utility of dimensionless parameters that are proposed theoretically to predict the defect formation phenomenon.

CHAPTER 4.

EXPERIMETAL PROCEDURES

4.1 Alloy Selection

A typical commercial nickel-based superalloy PWA 1484 was selected as the experimental material. PWA 1484 is a secondary generation proprietary alloy of Pratt & Whitney Company and is utilized to produce directionally solidified and single crystal castings. The nominal and actual compositions of the alloy are listed in Table 4-1. It shows that there is a high concentration of heavy refractory elements such as tungsten, tantalum, and rhenium. The sample rods had a diameter of 1.9cm and length of 19~20cm. The rods were cast in ceramic mold from one heat, and the original microstructure in the rods was equiaxed.

Another type of nickel-based superalloy MM 247 was also selected as an experimental material for comparison. This alloy contains high concentration of Cr to improve oxidation resistance, and Hf to improve the transverse ductility by forming carbides at grain boundaries. MM247 is widely used to produce equiaxed and directionally solidified castings. The nominal and actual compositions of the alloy are also listed in Table 4-1. The MM247 samples had a diameter of 1.27cm and length of 19~20cm. For each sample, a ceramic sheath with diameter 0.2 cm and 10 cm length was placed at the center of the rod for inserting a thermocouple.

Table 4-1. The nominal and actual compositions of experimental alloys PWA 1484 and

MM247 (The actual composition data are provided by supplier:

Howmet Corporation, Whitehall, MI.)

	AL	Cr	Co	Mo	Ti	W	Ta	Re	Hf	Fe	C	B	Zr
PWA1484 (nominal)	5.6	5	10	2		6	9	3					
PWA1484 (actual)	5.7	4.96	9.88	1.89		5.86	8.74	2.98			0.0238	0.001	0.0028
MM247 (nominal)	5.5	8.3	10	0.7	1	10	3		1.5		0.15	0.015	0.05
MM247 (actual)	5.7	8.35	10.13	0.8	0.99	10	3.07		1.23	0.95	0.162	0.015	0.045

4.2 Casting Facilities

4.2.1 Casting Furnaces

A vertical Bridgman crystal growth facility at Auburn University was used to perform all directional solidification experiments. The facility (Figure 4-1) consists of two furnaces, a loading and withdrawal system, one mechanical vacuum pump, and the thermal monitoring system. The two furnaces create the vertical thermal gradient and force the directional solidification of crystal materials. The two furnaces are separated with an adiabatic insulator layer and connected with a loading channel in the diameter of 6.5 cm. The mushy zone will often be located within the adiabatic zone.

The top furnace is a ATS high temperature furnace with 3800 watts power capacity and can heat up to a maximum temperature of 1650°C. Two different geometrical furnaces are used in the experiments, an ATS Model 3350 box furnace with an adiabatic insulator layer of 13 cm thickness and ATS Model 3320 cylindrical furnace with an adiabatic insulator layer of 5cm thickness. The furnace operation functions, heating rate, cooling rate, and soaking at given temperatures, can be programmed and controlled with one temperature controller (ATS 2010).

The bottom furnace acts as booster furnace (model: WATLOW Full Cylinder Unit, 425 Watts power capacity), which can reach a maximum temperature of 1100°C. This furnace is used to adjust the applied thermal gradient. When this furnace is used, the gradient will be in the range of 10~40 °C/cm. When the booster furnace is removed and substituted with water-cooling coils, the gradient can reach a maximum of 120 °C/cm.
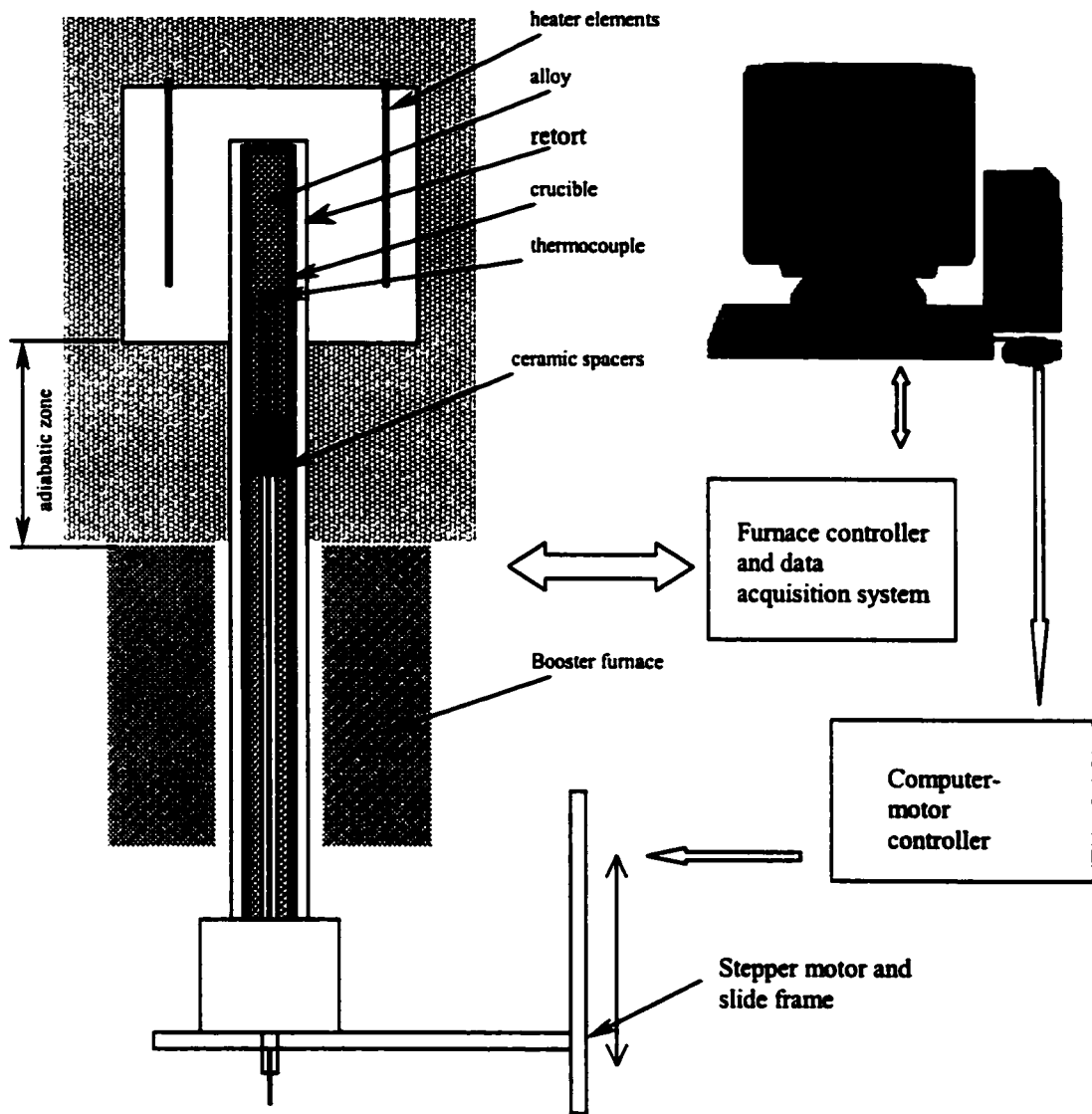
Figure 4-1. Vertical Bridgman crystal growth facility at Auburn University: featuring hot zone furnace, booster furnace, vacuum pump, mechanical withdrawal device, and thermal measurement.

4.2.2 Loading/Withdrawal System

Samples were loaded into and withdrawn out of the chamber of the furnace using

a mechanical system. Samples were contained in alumina crucibles and inserted in a

retort, which was sealed at the bottom to enable evacuation or purge with argon gas to

minimize oxidation of the alloys at elevated temperature. The retort is an alumina

ceramic tube with an inner diameter of 3.81 cm and length of 57 cm. The top 18 cm

length of the retort is in the chamber of the hot zone. Crucible spacers were used to raise

the alloys into the hot zone inside the retort. The sample, crucible and retort assembly

were attached to a Compumotor Drive system (Parker) that allows precise control of

sample withdrawal velocity using a computer. The withdrawal velocity utilized in this

study varied between 0.00005 cm/sec ~ 0.01 cm/sec. The withdrawal motion of samples

can also be programmed to change velocity or stay at one position for a given time.

The alumina crucibles for loading PWA 1484 samples had an inner diameter of

1.9 cm (out-diameter 2.54cm) and length of 25.4 cm. The samples were grounded slightly

so that a small gap existed between the sample and crucible inner wall. This gap ensured

that the thermal expansion of samples did not break the alumina crucible. For alloy

MM247 samples, the crucibles with an inner diameter of 1.27 cm and outside diameter

1.9 cm were used and fastened with cement so that the crucibles and samples would stand

rigidly within the retort.

While doing the quench experiment, the sample/crucible assembly was locked to

a metal-housing that was attached to a stage by a pin (Figure 4-2). The assembly was
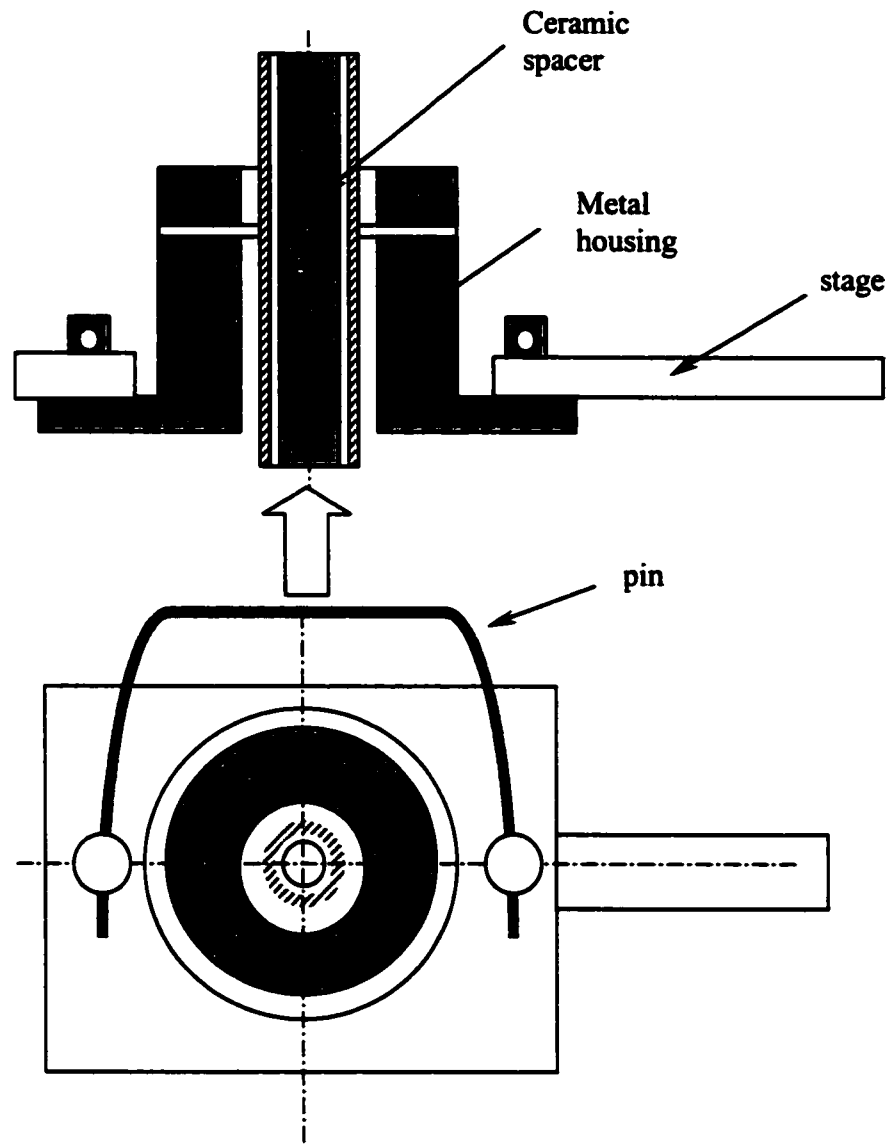
Figure 4-2 Mechanical clamp assembly designed to perform quench experiment by dropping sample/crucible into water.

loaded inside a mullite tube instead of the sealed retort. The argon atmosphere was provided by passing commercial purity argon gas at a very low flow rate through the mullite tube. When performing quenching, the pin was pulled out and the sample/crucible/metal-housing assembly dropped into the quenching water. All steps were the same as those used in the previous directional solidification process.

4.2.3 Thermal Measurement and Recording System

Temperature is obviously a critical variable for directional solidification. The successful implementation of temperature measuring and recording provided valuable data about the mushy zone location inside the adiabatic zone, the axial thermal gradients, and the radial thermal gradients that control the macroscopic shape of the growth interface. The arrangement of thermocouples is illustrated in Figure 4-3. Five B-type thermocouples were placed to record and monitor temperature at the given locations. To insert the alumina sheath and thermocouple, a hole with diameter of 0.64cm and depth of 10cm was cut at the center of the sample rod with EDM. Thermocouple #1 (or TC-1) was inserted at the center of the samples and shielded from the melt by an alumina sheath. TC-2 was located at 3 cm below the TC-1. The data of these two thermocouples were used to calculate the vertical thermal gradient and verify the repeatability of thermal profile. Thermal gradients were calculated using following equation:

$$G = \frac{T_1 - T_2}{L_1 - L_2} = \frac{T_1 - T_2}{(t_1 - t_2) \times V} \tag{4.1}$$

where T_1 was temperature of TC-1 at first reading time (t_1). T_2 was temperature of TC-1
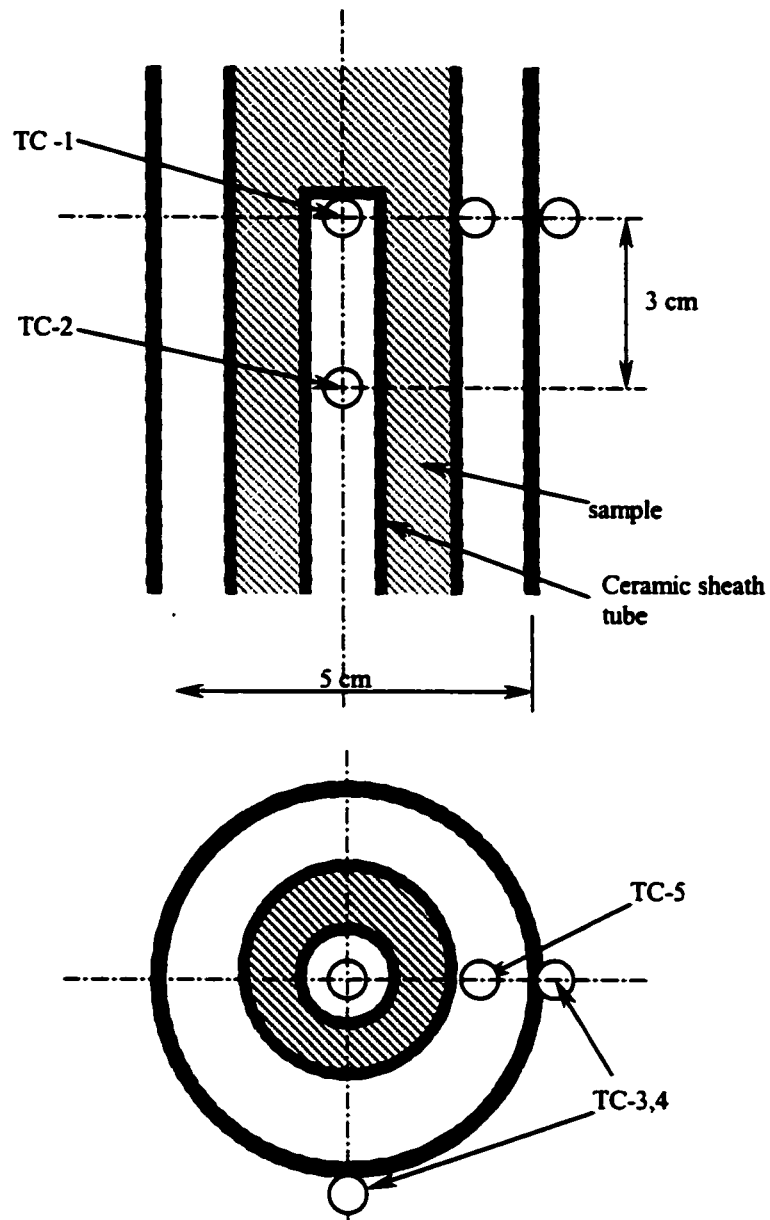
Figure 4-3. The arrangement of thermocouples in the directional solidification
experiments

at second reading time (t_2). V was the withdrawal velocity of the experiment. Hence the numerator indicates the temperature difference between any two points and the denominator indicates the distance between the two points.

TC-3 and TC-4 were located at the same vertical level as TC-1 but outside of the retort at positions perpendicular to each other. The data of these two thermocouples were used to assess the radial thermal distribution. TC-5 was installed outside of the sample crucible to evaluate the radial thermal gradient for the sample/crucible assembly.

4.3 Sample Casting Procedures

All solidification experiments were carried out using the following procedures at a given withdrawal velocity and furnace temperature.

a) Sample was loaded into crucible. The bottom of the crucible was sealed with cement, which was then heated and cured for 30 minutes. After that, the crucible with the sample was inserted into the retort, which was sealed with flanges.

b) The thermocouple wires were connected to a feed-through at the flanges.

c) The sample/ crucible and retort assembly was attached to the stage driven by the mechanical system and loaded into furnace chamber.

d) Figure 4-4 shows the heat profile utilized in the process. During the temperature range from 25 °C to 350°C of TC-1 reading, the retort was pumped and purged with Ar repeatedly with a 5 minute interval in order to remove any residual air inside the retort.
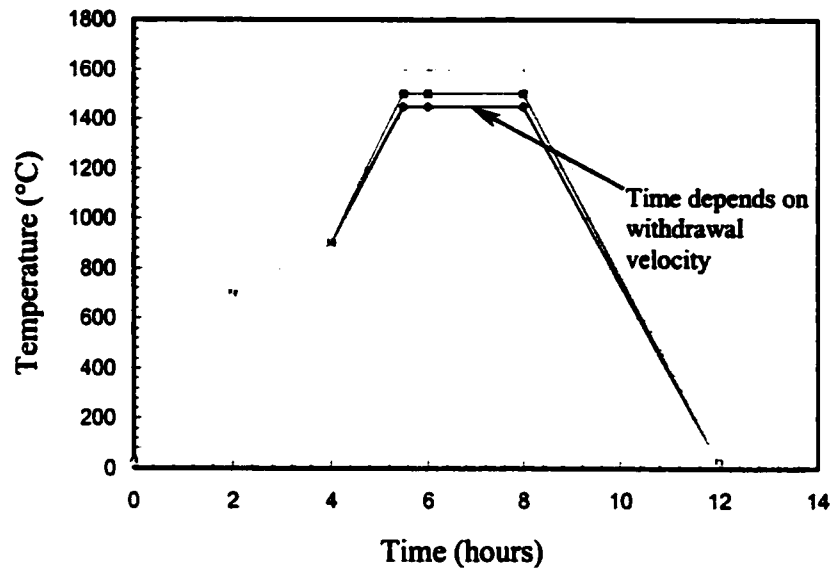
Figure 4-4. Heating and cooling schedules for the hot zone furnace for melting

alloys and directional solidification process

e) When the temperature reading of TC-1 reached 350 °C, the valve connected to the pump was closed and the valve connected to argon gas was turned on until the completion of the experiment.

f) Within the temperature range from 700°C to 900 °C, the heating rate was set as low as 100 °C/hr, which is necessary considering the larger thermal expansion of alumina ceramics in this temperature range.

g) After reaching the desired temperatures, i.e., 1450, 1500,1550,1600°C, the samples were soaked for at least 60 minutes prior to initiating withdrawal and solidification so that the thermal distribution of liquid metal could reach equilibrium.

h) Sample assembly was withdrawn from the furnace at a given velocity until the whole sample moved out of the furnace. Then the sample was allowed to cool in air.

4.4 Specimen Characterization

After completing solidification, the exterior of each sample was visually inspected to check whether freckle chains were present. Visual inspection was conducted on the as-cast and etched samples. Macroetching was accomplished by immersing the entire bar in a solution of 50ml HCl + 2ml HNO$_3$ + 5 gm FeCl$_3$ for approximately 2 minutes. Sample bars were then rinsed and dried.

Samples were sectioned at selected locations where steady-sate solidification was indicated by the thermocouple responses. Transverse sections, perpendicular to the growth direction, were cut 15 cm from the bottom of the samples. Longitudinal sections 2cm long in the growth direction were also cut from the center of the cylindrical bar and immediately adjacent to the transverse section. The sectioned pieces were mounted, ground and polished using standard metallographic techniques. All polished samples were etched for metallographic examination using a fresh solution of 10 ml HCl + 10 ml HNO_3 + molybdic acid 0.3 gm+15 ml distilled water.

Metallographic examination was performed with an Olympus PME3 inverted metallurgical microscope and a JEOL840 scanning electron microscope (SEM)

The transverse samples were used to determine the primary dendrite arm spacing (PDAS or λ_1), and longitudinal sections for the assessment of secondary dendrite arm spacing (SDAS or λ_2). PDAS (λ_1) was calculated by using the relationship $\lambda_1 = (A/N)^{0.5}$, where A is the area of the region within which the dendrite number N will be counted. SDAS (λ_2) was calculated using SDAS (λ_2)= N/L, where L is the length of well-aligned dendritic trunks and N is the number of second dendritic arms within the segment L.

The chemical analysis of segregation, precipitates and freckle chains was conducted using an energy dispersion spectrometer (EDS) microprobe attached to the SEM operated at 20 kV. The analysis used a Tracer Northern 5500 analyzer and LINK ISIS software with an ultra-thin window detector (UTW). The final composition result of each phase was the average of at least 5 data points. The equilibrium partition coefficient of each element was evaluated according to $k = C_S/C_L$. The composition at the center of a

dendritic trunk was used as that of the first solid to freeze at the liquidus temperature, that is, C_s. The composition at the center of the interdendritic region was used as that of the last liquid to freeze, that is, C_L. The freckle spots were marked and then analyzed using EDS.

CHAPTER 5.

RESULTS AND DISCUSSION

5.1 As-cast Microstructure Development of Directional Solidification Nickel-based Superalloy PWA1484

5.1.1 Directional Solidification Morphology Development

A number of PWA 1484 cylindrical bars were remelted and then directionally solidified in the Bridgman crystal growth facility. A wide range of solidification variables was utilized in order to simulate phenomena occurred in manufacturing as much as possible. Thermal gradients from 10 °C/cm to 110 °C/cm and growth velocities from 0.00005cm/s to 0.01 cm/s were utilized so that both dendritic and cellular microstructures could be produced. All process parameters employed are listed in Table 5-1.

Figure 5-1 shows typical cooling curves obtained as sample solidification proceeds. The mushy zone for this alloy can be estimated as the temperature range 1330 ~ 1400°C indicated by TC-1 or TC-2. The cooling curves (additional figures for various conditions are provided in the Appendix) show that the mushy zone location varies with growth velocity of a sample. The higher the solidification velocity, the further away from the hot zone was the position of the mushy zone. The displacement of the mushy zone results in changes of the spatial temperature distribution and interface geometry, and influences the microstructural development.

50

Table 5-1 Solidification matrix with calculated thermal gradients and measured arm

spacings

Exp.#	Furnace Temperature (°C)	Withdraw Velocity (cm/sec)	Thermal Gradient (°C/cm)	Cooling Rate (°C/sec)	PDAS (μm)	SDAS (μm)	Freckles (Yes/No)
20	1600	0.01	17	0.17	454	42.8	N
21	1600	0.005	30	0.15	362		N
23	1600	0.0025	35	0.088	376	78.6	N
22	1600	0.001	36	0.036	359	NA	N
24	1600	0.0005	40	0.02	360	NA	N
33	1550	0.005	28	0.14	355	49.6	N
32	1550	0.0025	36	0.09	372	66.6	N
31	1550	0.001	38	0.038	353	NA	N
30	1550	0.0005	38	0.019	364	NA	N
29	1500	0.01	15	0.15	470	43.4	N
25	1500	0.005	20	0.1	422		N
26	1500	0.0025	28	0.07	385	65.4	N
27	1500	0.001	28	0.028	395	NA	N
28	1500	0.0005	28	0.014	400	NA	N
38	1470	0.01	12	0.12	511	44.6	N
37	1470	0.005	18	0.09	434	52.2	N
36	1470	0.0025	21	0.053	413	NA	N
35	1470	0.001	23	0.023	408	NA	N
34	1470	0.0005	25	0.013	420	NA	N
Quench#1	1600	0.0001	40	0.004	383	NA	N
Quench#2	1600	0.00005	40	0.002	450	NA	N
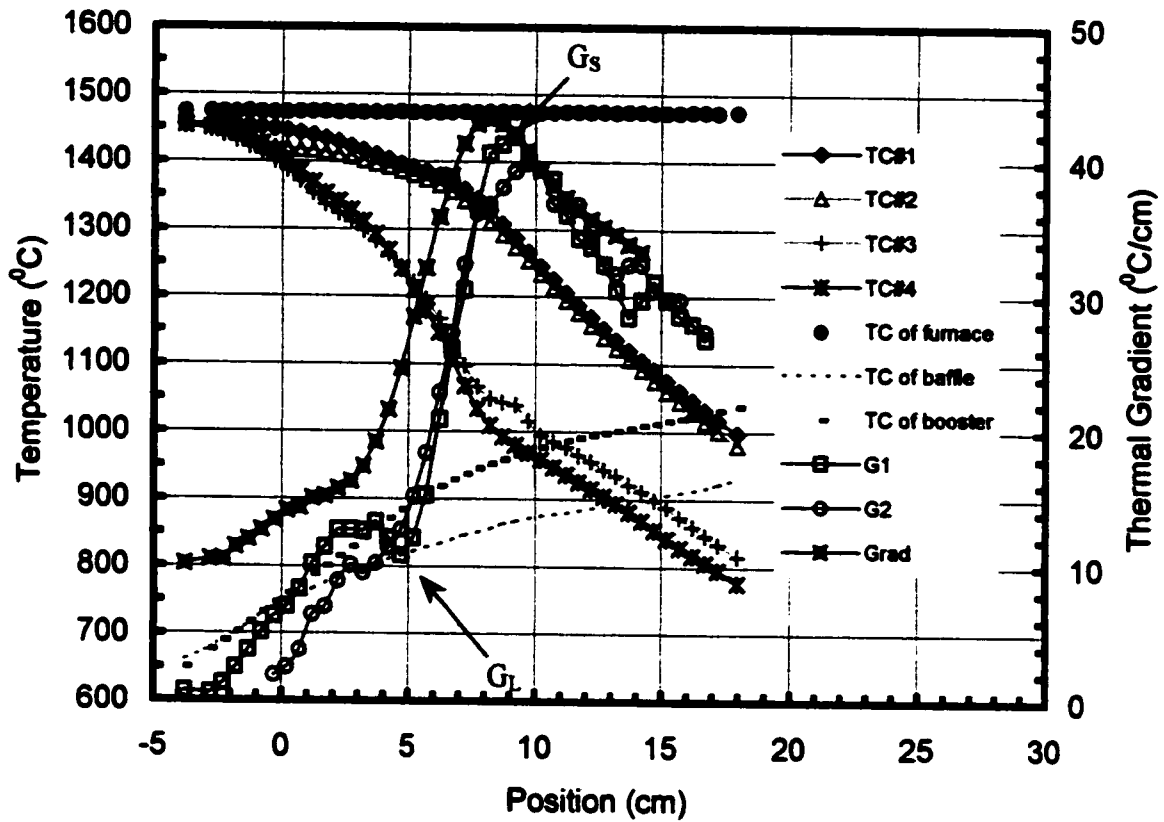
Figure 5-1. Typical thermal cooling curves for DS experiment of PWA 1484. The curves were obtained with growth velocity V= 0.01 cm/s, G_L= 12 °C/cm. Axes x=0 indicates the start point of adiabatic zone (G1, G2: longitudinal thermal gradient from TC-1 and TC-2 individually according to the equation (4.1) at the page of 43)

The axial thermal gradient is calculated from the temperature data of TC-1 or

TC-2 using Equation (4.1). Calculated results of thermal gradients for all samples are

plotted with the thermal profiles (Figure 5-1 and Appendix). It can be seen that the axial

thermal gradient varies over the mushy zone i.e., at the temperature range from $1400^{\circ}C$ to

$1330^{\circ}C$. In all experiments, the gradient at the tip of dendrites or cells (G_L) is small.

Behind the tip, the gradient increases in approximately linear fashion until the solidus

temperature at the bottom of the mushy zone. The thermal gradient at the tip of dendrites

or cells (G_L) is utilized in further analysis of growth behavior since the dendritic/cellular

arm spacings and morphologies are significantly influenced by the behavior at the tip

region. The thermal gradients in the Table 5-1 are G_L for all samples.

Figures 5-2, 5-3, and 5-4 show typical PWA 1484 microstructures produced under

given conditions. The top figures are microstructures of transverse sections perpendicular

to growth direction, while the bottom figures are of longitudinal sections, parallel to the

growth direction. The growth velocity (V) and thermal gradient (G_L) are indicated below

the pictures. The basic solidification microstructures of these samples at room

temperature are comprised of dendritic or cellular cores ($\gamma+\gamma'$) along with eutectic ($\gamma+\gamma'$),

metal carbides (MC) distributed throughout the interdendritic area. Some interdendritic

porosity is also evident. All dendrite or cellular cores exhibit excellent alignment with the

axial thermal gradients imposed.

Figures 5-2 (a, b, c) illustrate the microstructural features for samples solidified at

thermal gradient of 17~25 $^{\circ}C/cm$. The microstructure transitions from flanged cells (V=

0.0005cm/s) to well-developed dendrites (V=0.01 cm/s) with the increase of growth

Figure 5-2(a). Transverse and longitudinal section microstructure of PWA 1484

sample grown at G=25°C/cm and V=0.0005 cm/s (400μm: ⟶)
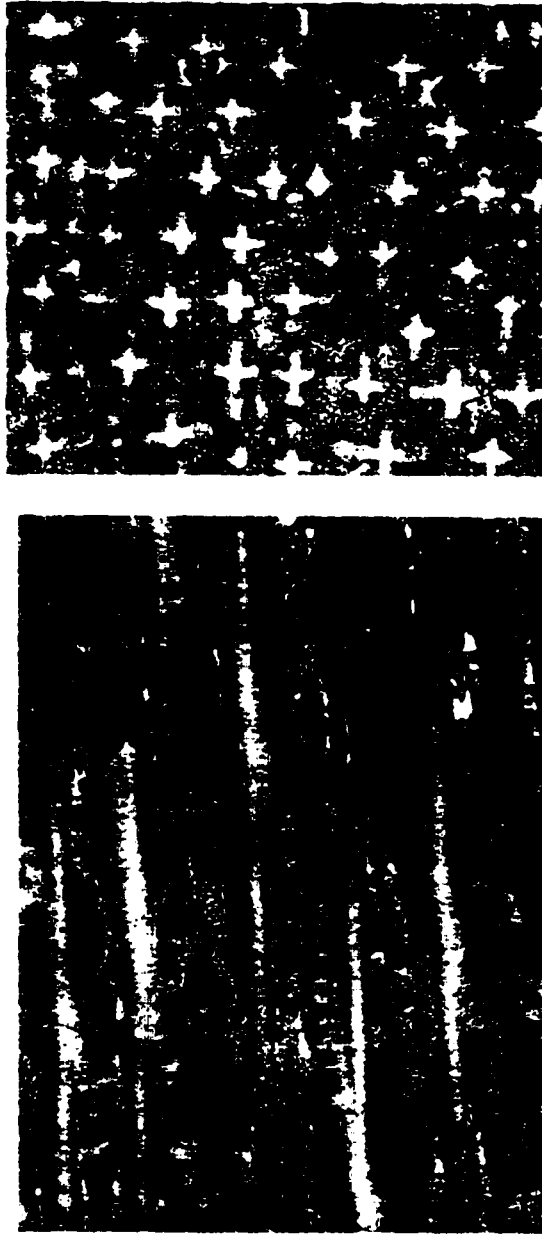
Figure 5-2(b) Transverse and longitudinal section microstructure of PWA 1484

sample grown at G=23°C/cm and V=0.001 cm/s (400μm: ━━━)

Figure 5-2(c) Transverse and longitudinal section microstructure of PWA 1484 sample

grown at G=17°C/cm and V=0.01 cm/s (400μm: ▬▬▬)

velocity. At a growth velocity of 0.01 cm/s (Figure 5-2c), there are large secondary

dendrite arms and well-developed tertiary arms. At a growth velocity of 0.0005 cm/s

(Figure 5-2(a)), the secondary branch arms are almost non-discernable in the longitudinal

section; the transverse section shows the "cross" dendrites, which are often referred to as

flanged cells.

Some authors characterize microstructures like those shown in Figure 5-2(a) as

cellular dendrites. The experimental velocities for transition from cellular to dendritic

growth can be difficult to evaluate as there is often inconsistency on the terminology

employed in the literature. Some researchers prefer to describe a microstructure as

dendritic only when secondary branches can be discerned, e.g., Flemings[52]. Cells grow

without significant regard to the crystallographic orientation of the crystal structure.

However, Kurz and Fisher[92] note that there is a range of intermediate forms (dendritic

cells and cellular dendrites) when various degrees of crystallographic directionality

persist in the growth form even though no secondary arm development has occurred. The

sample shown in Figure 5-2(a) exhibits microstructures where the underlying

crystallographic orientation is clearly important in the growth process, but no secondary

dendritic arms were exhibited in the as-cast conditions.

Figures 5-3(a, b, c) illustrate the development of microstructure at the high

thermal gradients of 54~91 °C/cm. A transition from flanged cells to dendrites is again

observed as V increases. However, there is one significant difference between Figure 5-2

(c) and Figure 5-3 (c). The secondary arms are not as well developed in Figure5-3 (c) as
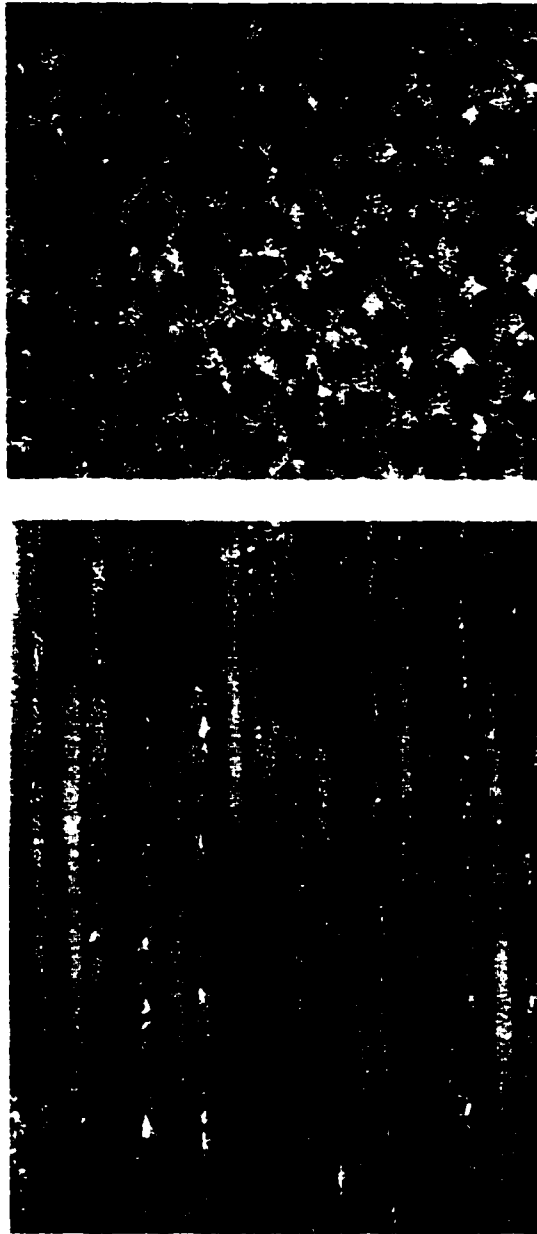
Figure 5-3(a) Transverse and longitudinal section microstructure of PWA 1484 sample

grown at G=54°C/cm and V=0.0005 cm/s (400μm: ━━)
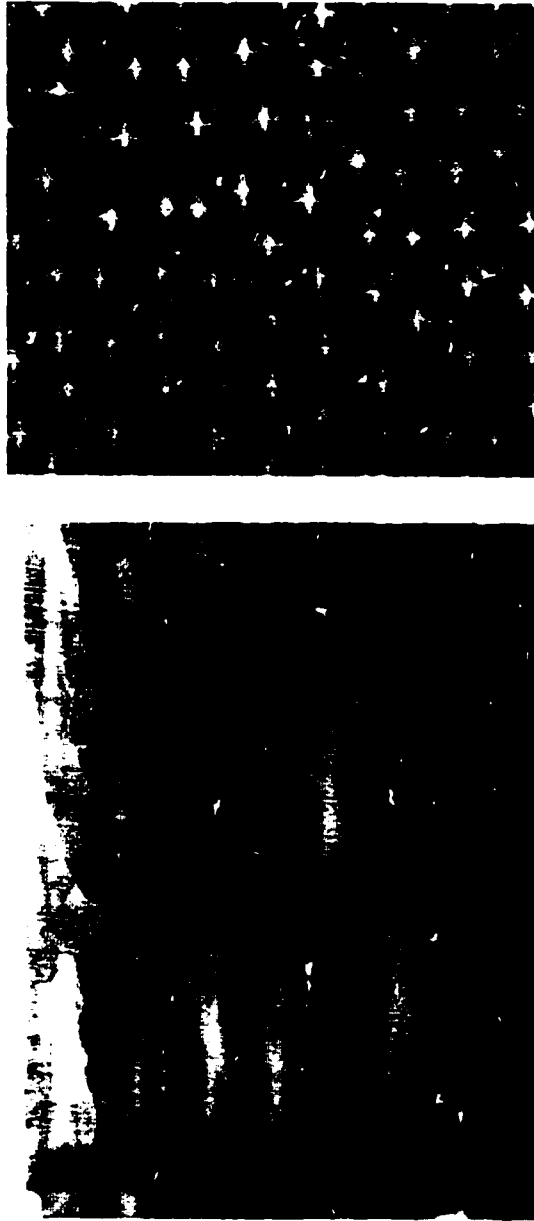
Figure 5-3(b). Transverse and longitudinal section microstructure of PWA 1484 sample
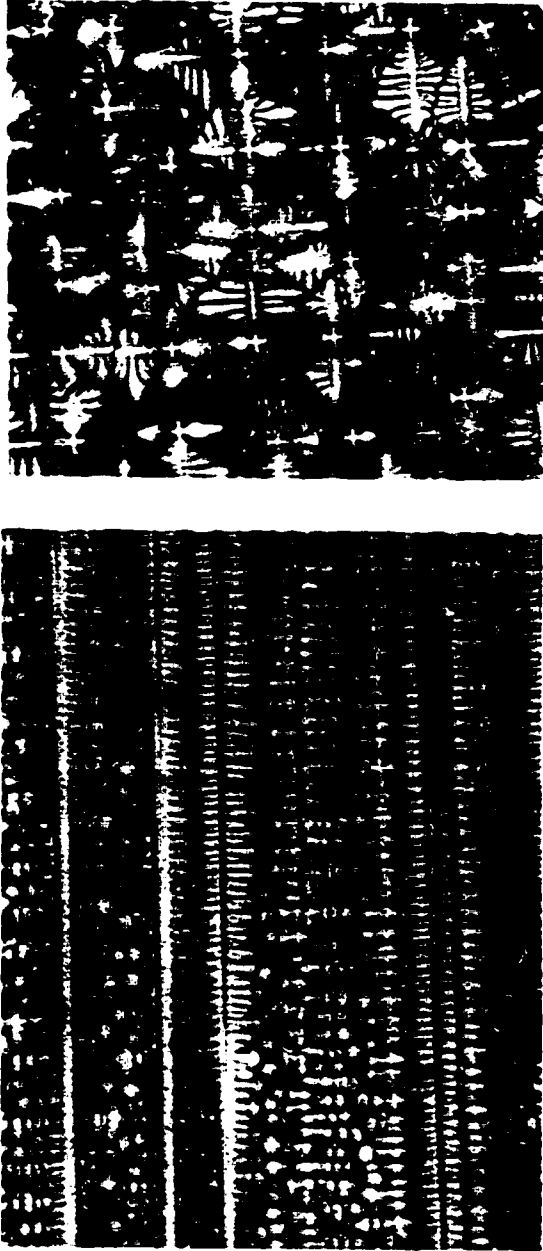
grown at G=70°C/cm and V=0.001 cm/s (400μm: ━━━)
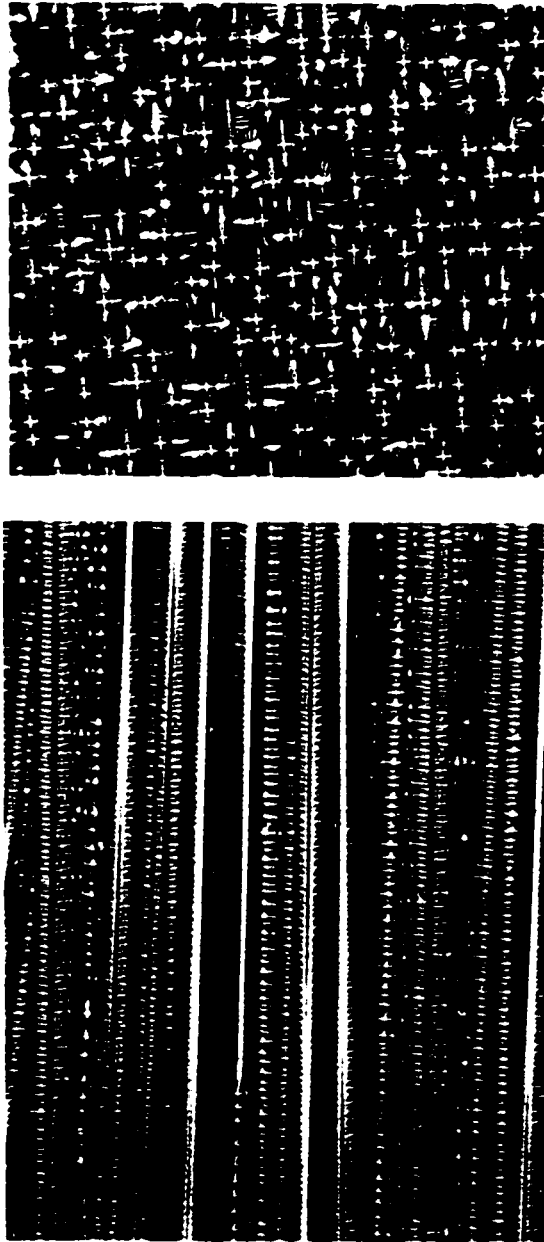
Figure 5-3(c) Transverse and longitudinal section microstructure of PWA 1484 sample

grown at G=91°C/cm and V=0.01 cm/s (400μm: ━━)

those at Figure 5-2 (c), and the arm spacings are much smaller in Figure 5-3 (c) (see the detailed discussion in the next section). Both were grown at a growth velocity as 0.01 cm/sec, but under different thermal gradients. It has been shown that the primary arm spacings decrease with increasing thermal gradient [35,93] and cooling rate [25, 31, 43, 52, 59, 67, 94-96].

Samples were also grown at V= 0.0001 and 0.00005 cm/s with thermal gradient G = 40 °C/cm. Each sample was grown for approximately 6 cm and then quenched to preserve the mushy zone microstructures. Transverse and longitudinal sections of these samples are shown in Figure 5-4. Examination of the cells near their tips in the longitudinal section shows evidence of secondary arms on some cells. It also seems probable that the flanged cells shown in Figure 5-2, 5-3 likely also exhibited secondary arms near their dendrite tips and that this morphology degenerated into the flanged cells seen at room temperature.

In order to provide insight into the morphological transition, the present results are plotted in Figure 5-5 with the previously published data of other nickel-based superalloys[28]. Figure 5-5 shows the transition between dendrites and equiaxed grain structures in this investigation goes to much lower G/V values than previous reports. More work is needed to quantitatively define the transition between dendrites and equiaxed grain structures.
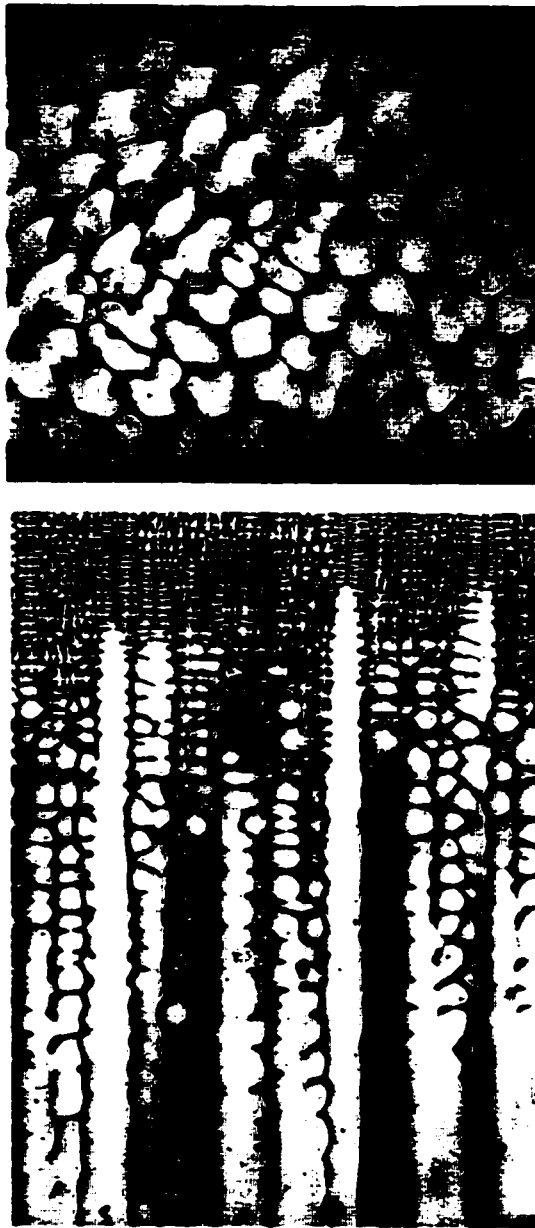
Figure 5-4 (a) Transverse and longitudinal section microstructure of PWA 1484 sample

grown at G=40°C/cm and V=0.0001 cm/s (666μm: ━━━)

Figure 5-4 (b) Transverse and longitudinal section microstructure of PWA 1484 sample

grown at G=40°C/cm and V=0.00005 cm/s (666μm: ━━━)
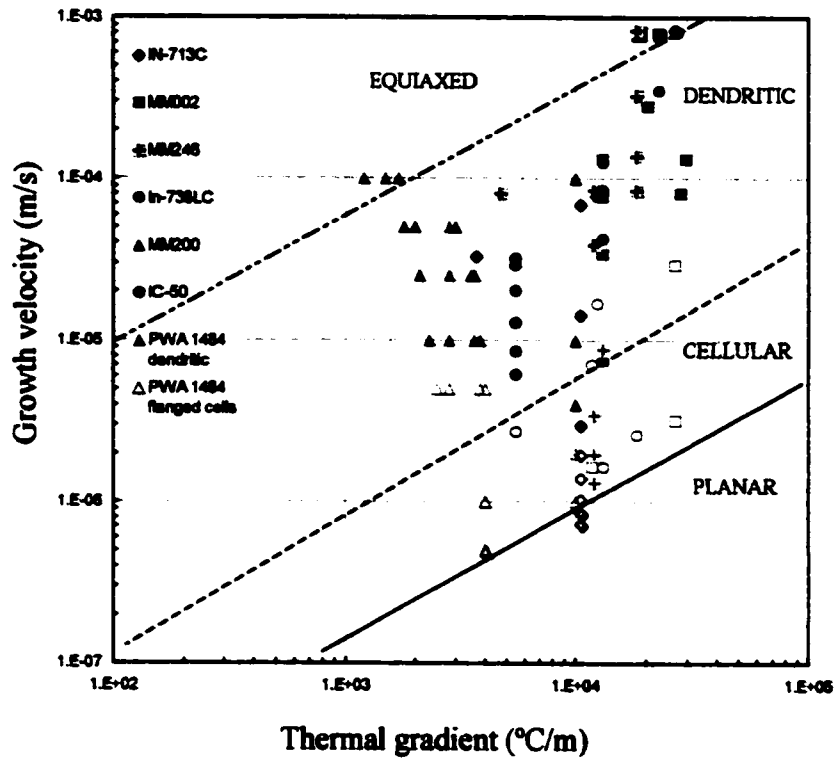
Figure 5-5. Planar- cellular- dendritic- equiaxed morphology transition chart for nickel-based superalloys[28] (solid marks: dendritics; open marks or light background colors: cellular; shadow marks at lowest velocities: planar or near-planar growth; shadow marks at the highest velocities: equiaxed grains)

5.1.2. Primary Arm Spacing (λ_1)

The primary arm spacings (λ_1) of dendrites or cells are usually correlated with

three different process parameters, $G^{-1/2}V^{-1/4}$ ($m^{-0.25}sec^{0.25}K^{-0.5}$), cooling rate GV (°C/s),

and growth velocity V (cm/s). The PWA 1484 data are evaluated with respect to each of

these below.

Figure 5-6 illustrates the primary cells/dendritic arm spacings (λ_1) of PWA 1484

correlated with the process parameter $G^{-1/2}V^{-1/4}$ (Note: $G^{-1/2}V^{-1/4}$ is the independent

variable in the Hunt (Eq. 2.4) and Kurz and Fisher (Eq. 2.6) models for dendritic growth).

The velocities utilized and the morphologies of each sample's microstructure at room

temperature (flanged cellular, mixed cellular/dendritic, or dendritic) are identified by the

symbols in Figure 5-6. At the highest values of $G^{-1/2}V^{-1/4}$ (i.e., lowest cooling rate), the

samples exhibit cellular microstructures after cooling to room temperature. At the lowest

values of $G^{-1/2}V^{-1/4}$ (i.e. highest cooling rates), the samples exhibit well-aligned dendritic

microstructures with secondary arms. Intermediate values of $G^{-1/2}V^{-1/4}$ yielded samples

that displayed mixed results. Intermediate values of $G^{-1/2}V^{-1/4}$ utilizing high velocities

(i.e., 0.005 and 0.01 cm/sec and low gradients) produced dendritic microstructures.

Intermediate values of $G^{-1/2}V^{-1/4}$ with a low velocity of 0.0005 cm/sec produced

flanged-cellular microstructures. Intermediate values of $G^{-1/2}V^{-1/4}$ with an intermediate

velocity of 0.001 cm/s produced microstructures with mixed flanged-cellular and

dendritic growth. The results of Figure 5-6 show two distinct growth regimes: (1)

dendritic growth with a marked dependence of λ_1 on the imposed process
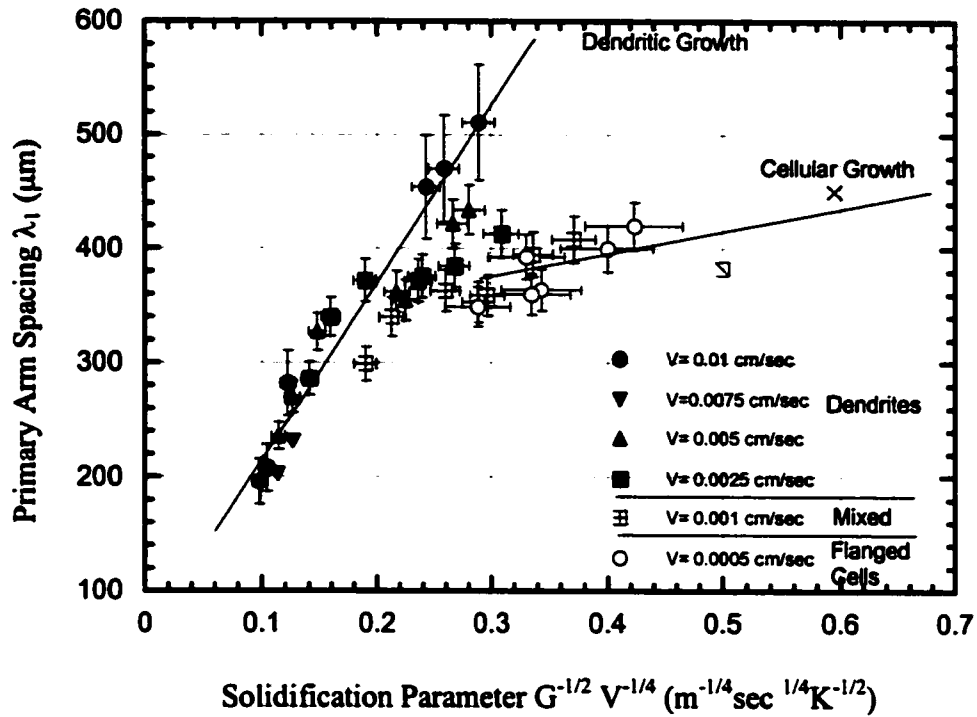
Figure 5-6 Primary dendritic arm spacings of DS PWA 1484 evaluated against

solidification parameter $G^{-0.5}V^{-0.25}$ ($m^{-1/4}$ $s^{1/4}$ $K^{-1/2}$). Two solid lines represent the

tendencies of the development of arm spacings, and are approximated

to the experimental data. (mark X: sample grown at 0.00005 cm/sec; mark◁ :

sample grown at 0.0001 cm/sec)

parameter $G^{-1/2}V^{-1/4}$ and (2) flanged cellular growth with a much smaller dependence of λ_1 on the imposed process parameter $G^{-1/2}V^{-1/4}$.

Figure 5-7 shows that very large dendritic spacings are available at low solidification velocity and low thermal gradients (or high $G^{-0.5}V^{-0.25}$). One superalloy IN718 sample cylinder of diameter 0.6 cm and 5 cm length was previously frozen with approximate values of $V = 10^{-5}$ cm/s and G~ 1°C/cm. Although only a single primary dendrite developed, extensive secondary and tertiary arms are present. The secondary arm lengths grew as large as the sample macro-dimensions giving $\lambda_1 > 6000\mu m$.

Numerous experiments of solidification[42,46,93] have shown the exponents of growth velocity V and thermal gradient G are often not simple constants of -0.5 and -0.25, but can vary with process conditions. Bouchard and Kirkaldy[46] summarized exponential relationships of primary arm spacing with G and V for various binary alloys in steady-state heat flow solidification. Variations of -0.37~-0.54 for the exponent of G and -0.11 ~ -0.75 for V's exponent were found. McCartney and Hunt[93] stated that convective mixing during solidification plays an important factor in the variation of exponents. In McCartney and Hunt's investigation, a specially designed Al-Mg-Si alloy was selected to perform directional solidification experiments so as to minimize gravitational fluid flow in the liquid. The result showed exponents of -0.55 and -0.28 for G and V, respectively, very close to the theoretical values. A number of directionally solidified superalloy experiments[32,44,96,98,99] have shown there are good linear relationships to evaluate λ_1 with $G^{-1/2}V^{-1/4}$, although the measured V exponents are not exactly -0.25. Generally, all these experiments were conducted at high G of 100 ~
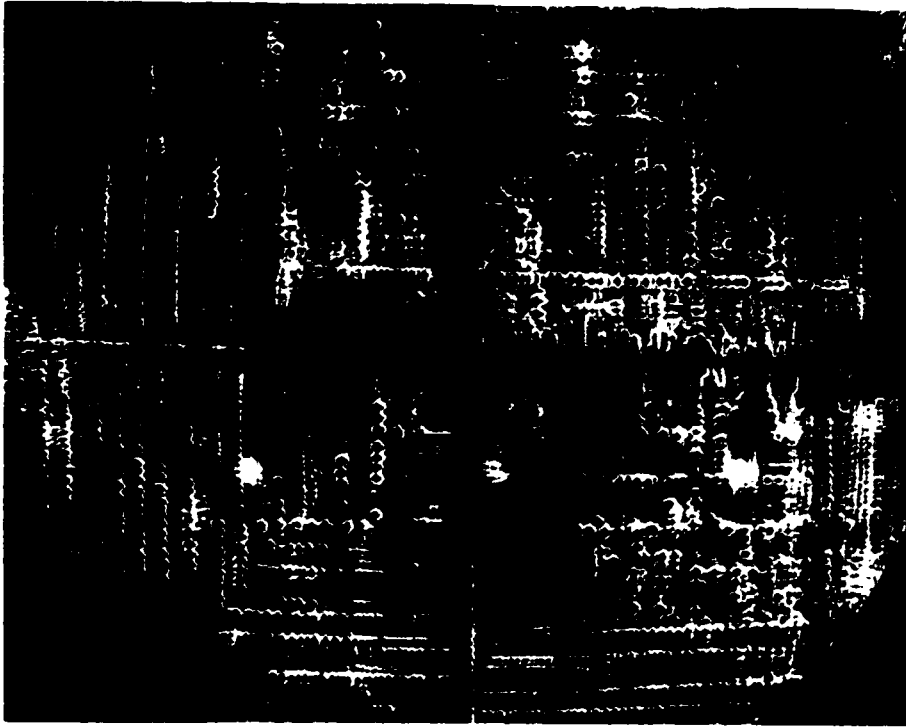
Figure 5-7. An as-cast single crystal IN718 nickel-based superalloy with extremely large

primary dendritic branch arms and high order branch arms (500μm: ━━━)

200 °C/cm, except IC 50 (Ni$_3$AL) with 54 °C/cm[28]. The present work shows one linear relationship for samples with well-developed dendritic microstructure, and another linear relationship for samples with flanged cells.

Figure 5-8 shows the dendritic/cellular arm spacings (λ_1) versus the cooling rate GV. The result is similar to Figure 5-6. There are two tendencies of arm spacing development; dendritic growth with a strong marked dependence of λ_1 on the imposed cooling rate and flanged-cellular growth with a decreased dependence of λ_1 on the cooling rate.

In order to better understand the individual roles of V and G, as opposed to their coupled effects (as exhibited by the theoretical growth parameter $G^{-1/2}V^{-1/4}$ and cooling rate GV), the experimentally determined primary spacings are plotted versus V in Figure 5-9. The gradients achieved in the samples are also shown in the Figure 5-9 and lines approximating constant G for five representative thermal gradients have been estimated and are included. As noted before, dendritic microstructures are exhibited at V> 0.001 cm/s while flanged-cellular microstructures are exhibited at V< 0.001 cm/s. Mixed microstructure of cells and dendrites are seen at V = 0.001~ 0.0025 cm/s.

Figure 5-9 shows that for all thermal gradient G > 28°C/cm, λ_1 decreases with increasing growth velocity V, as expected. Also slopes of λ_1 -V or exponents of V decrease with decreasing imposed thermal gradient G. Figure 5-10 shows the exponents of V for various thermal gradients. As the imposed gradient G increases, the exponent of V appears to be approaching the theoretical value of a_d = -0.25. Similar exponents of V
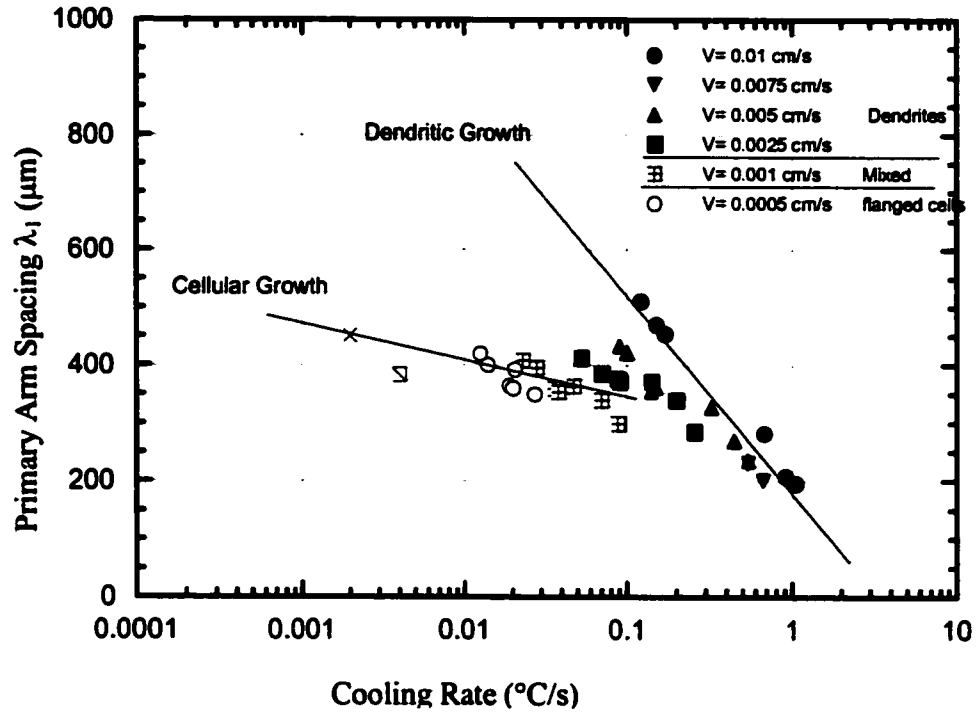
Figure 5-8. Primary arm spacings correlated with cooling rate (°C/s) for DS PWA

1484. Two solid lines represent the tendencies of the development of arm spacings, and

are approximated to the experimental data. (mark X: sample grown at 0.00005 cm/sec;

mark ⊠ : sample grown at 0.0001 cm/sec)
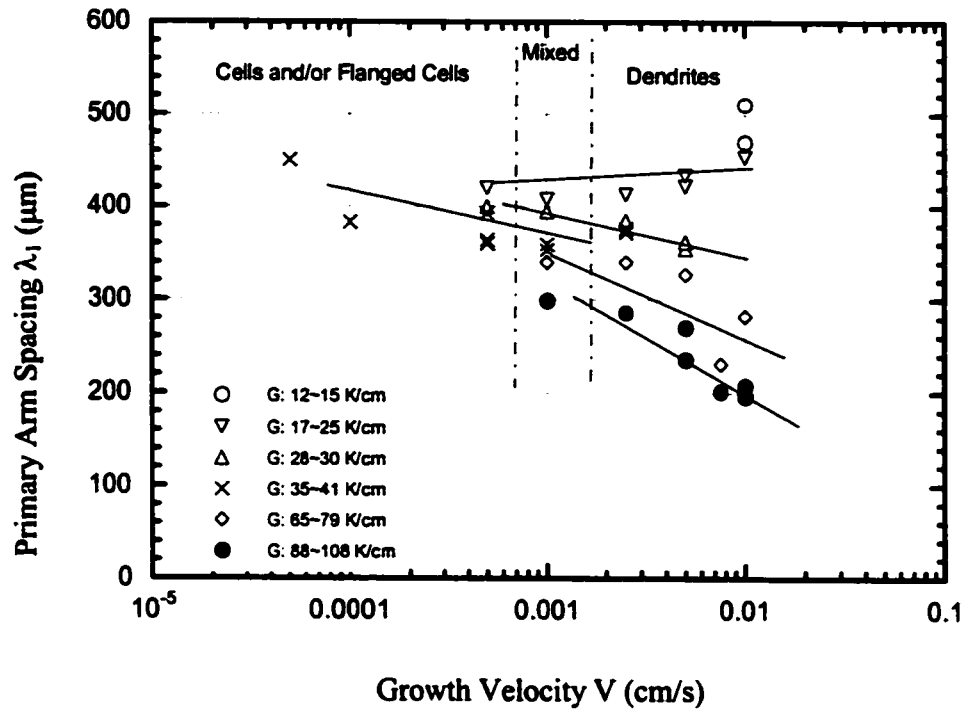
Figure 5-9. Primary arm spacing grouped in terms of gradient and evaluated versus growth velocity
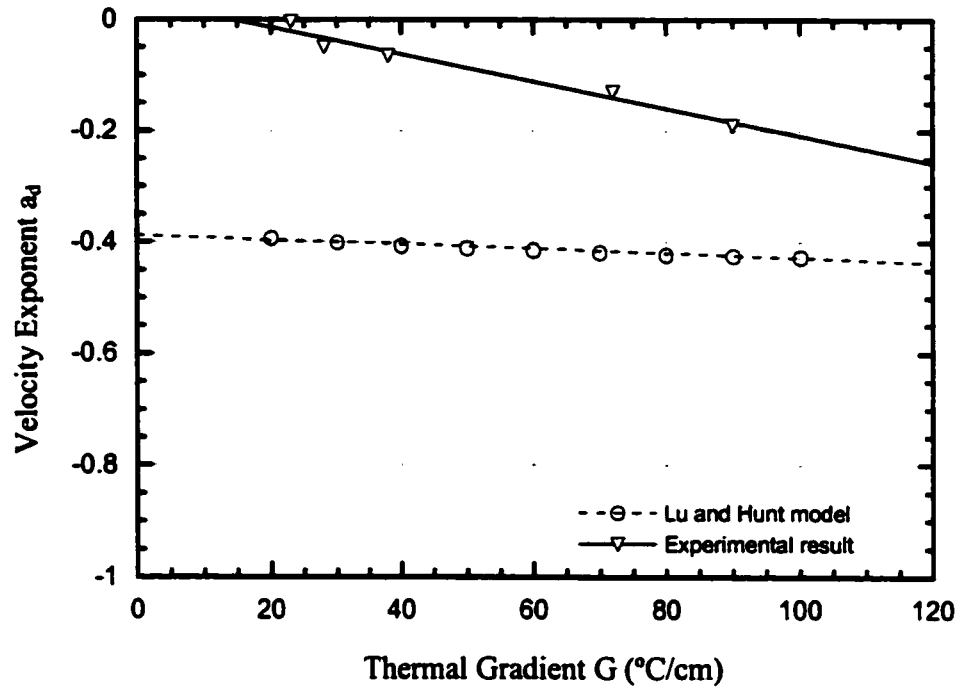
Figure 5-10. The dependence of the experimentally determined velocity exponent a_d with applied thermal gradient (Triangle: experimentally determined a_d; Circle: a_d estimated from Lu/Hunt analytic expression)

were found under high gradients by Kim[28] (-0.17) and Ma/Sahm[44] (-0.19). However,

for G = 17~25°C/cm, primary arm spacings λ_1 first decrease with increasing V for 0.0005

<V< 0.001 cm/s but then unexpectedly increase with increasing V for V> 0.001 cm/s. For

velocities as low as these, theoretical considerations indicate that the primary arm spacing

should always decrease with an increasing velocity[40,41,42], unless the thermal gradient

also decreases with increasing velocity as reported by Jamgotchian et al[100] and Grugel

and Zhou[49]. Significant decreases in experimental thermal gradient cannot explain the

unusual behavior seen in the present samples as the axial thermal gradient is reasonably

constant at 20~25 °C/cm.

The primary arm spacing results were compared to earlier intuitive models

proposed by Hunt[40], Kurz and Fisher[41], as well as against the recent theoretical models

proposed by Ma and Sahm[44], Lu and Hunt[42,43].

The physiochemical properties (D, Γ, ΔT_0, and k) of PWA 1484 required for

comparing the primary arm spacing data are shown in Table 5-2.

Table 5-2 Thermo-physical parameters of PWA 1484 employed
for theoretical analysis of arm spacings

k	0.83
D (cm^2/s)	2×10^{-5}
Γ (°C *cm)	1×10^{-5}
ΔT_0(°C)	70

k was evaluated using the Scheil equation and the solid-fraction data of PWA 1484. A 2.5 cm long and 1.9 cm diameter sample of PWA 1484 with a thermocouple inserted in the center was melted and frozen 6 times. The cooling curves obtained were evaluated by the method of Backerud [97] to identify the fraction solid f_s vs. temperature relationship. The maximum and minimum experimental curves thus obtained are shown in Figure 5-11. ΔT_0 of PWA 1484 is found to be 70 °C. The fraction solid vs. temperature relationship was estimated using Scheil's [46] equation, assuming that the liquidus and solidus are straight lines, viz.,

$$f_s = 1 - [\frac{T_m - T}{T_m - T_L}]^{\frac{1}{k-1}} \tag{5.1}$$

A pseudo-binary partition coefficient of $k = 0.83$ is seen in Figure 5-11 to give good agreement with the observed solidification behavior. Such a pseudo-binary partition coefficient is in general agreement with the elemental partition coefficients shown in Table 5-3 (page 102).

The Gibbs-Thomson coefficient Γ is approximately 1 X 10^{-5} cmK for many alloys [92]. This value was utilized in the theoretical estimations below. The mean diffusion coefficient D in the liquid was determined following the theory of constitutional supercooling where $D = \frac{\Delta T_0 V_c}{G}$ [92]. The critical velocity V_c for planar growth was estimated as $V_c = kV_t$ following Kurz and Fisher [41]. V_t is the approximate transition velocity for cellular-to-dendritic growth.
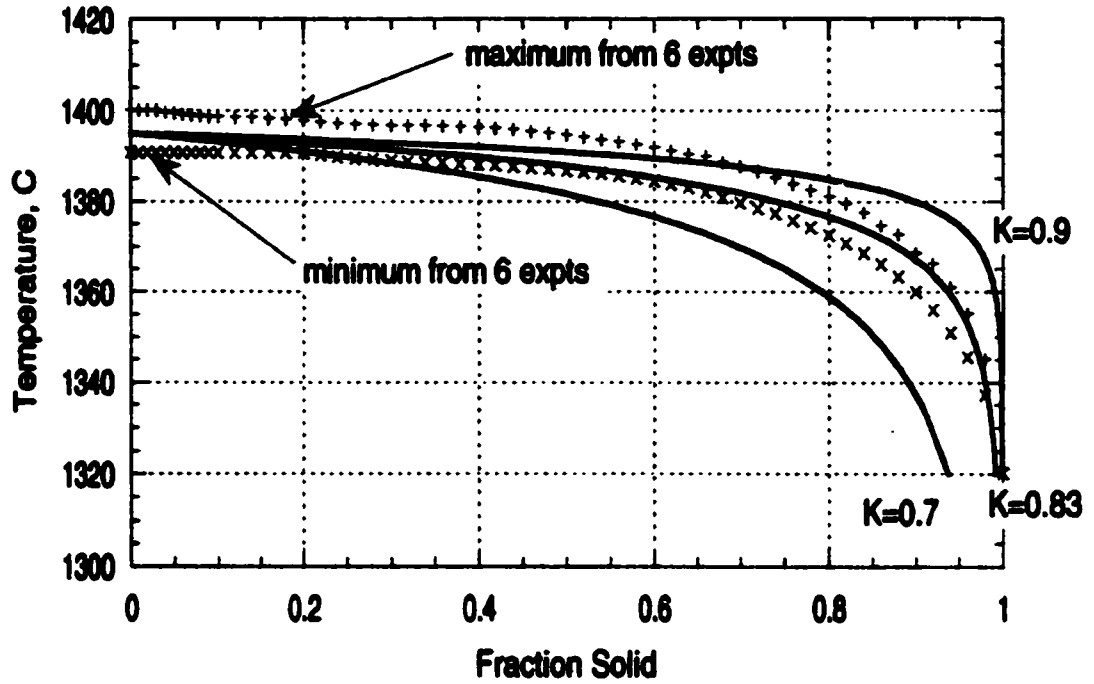
Figure 5-11. Temperature vs. fraction solid relationship for PWA 1484: minimum and maximum of a sample melted and frozen 6 times as well as estimates using Scheil's equation

Figures 5-12(a, b, c) compare experimental primary arm spacings data with the

theoretical models of Hunt[40], Kurz and Fisher[44], and Ma and Sahm[44] utilizing

equations (2.4), (2.6), (2.9), respectively. Ma and Sahm's theory provided the best

prediction of both the primary dendritic arm spacing data as well as the dependence upon

V under high gradients (Figure 5-12 (a), G~100 °C /cm) and medium gradients (Figure 5-

12(b), G~70 °C /cm). However none of these theories satisfactorily explained the

unexpected increasing λ_1 with increasing V seen at low thermal gradients.

The analytic expressions for cellular and dendritic spacings from Lu and Hunt's

more recent numerical results[42,43] are plotted in Figure 5-13 separately. According to

their model, the actual spacing for any condition could be any value between the array

stability limit (a minimum and equal to equation (2.7)) and the upper spacing limit for

either cells or dendrites. The upper spacing limit is typically twice the minimum array

stability limit. In Figure 5-13a (high thermal gradient) and Figure 5-13b (low thermal

gradient), the cross-hatched area represents the available spacings for the given

conditions. Good agreement is seen between the predictions of Lu and Hunt's model and

the experimental data for conditions of dendritic growth at high thermal gradient. As

before, poor agreement is exhibited by Lu and Hunt's model for the decreasing

dependence of λ_1 on V at low thermal gradients. The unusual behavior is examined more

closely in the following discussion:
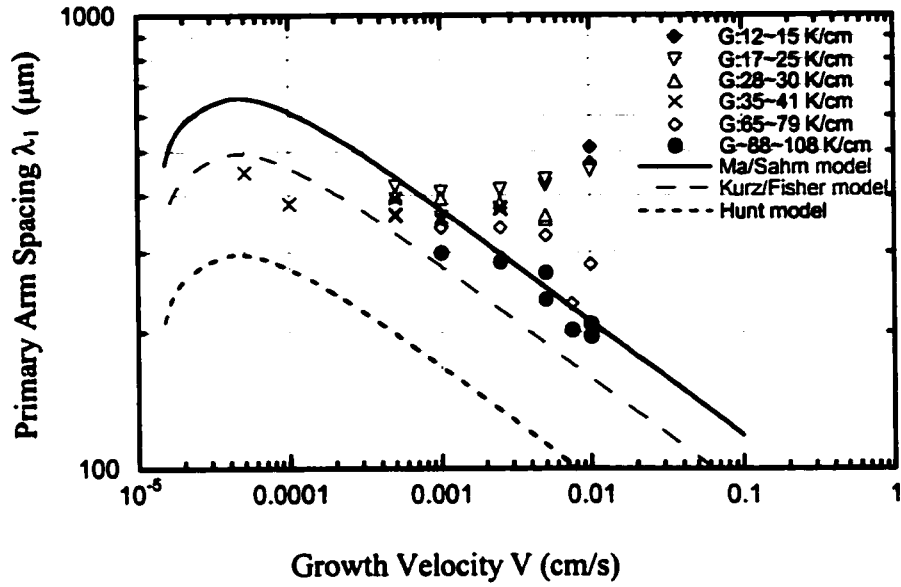
(a) G = 100 °C /cm
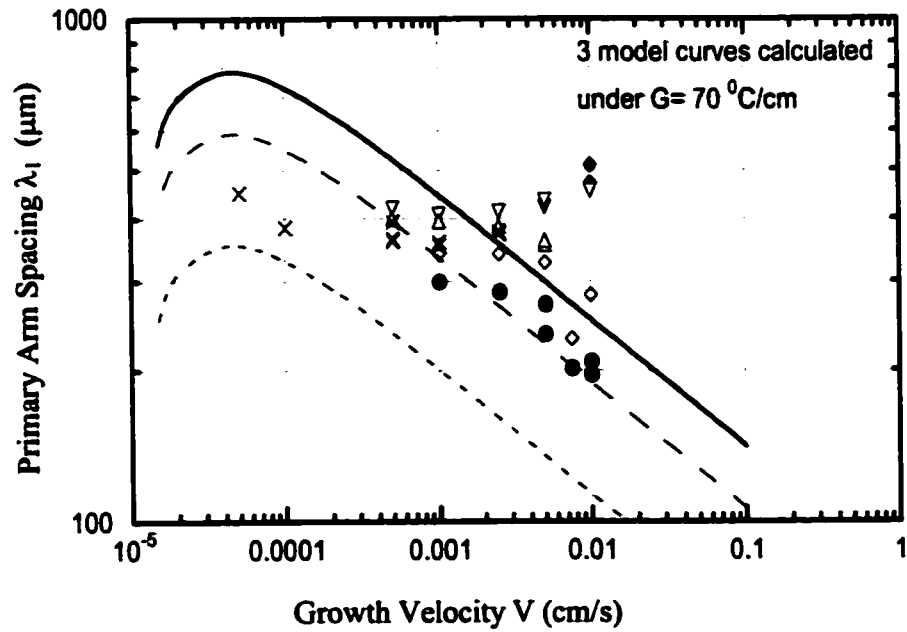
(b) G = 70 °C /cm
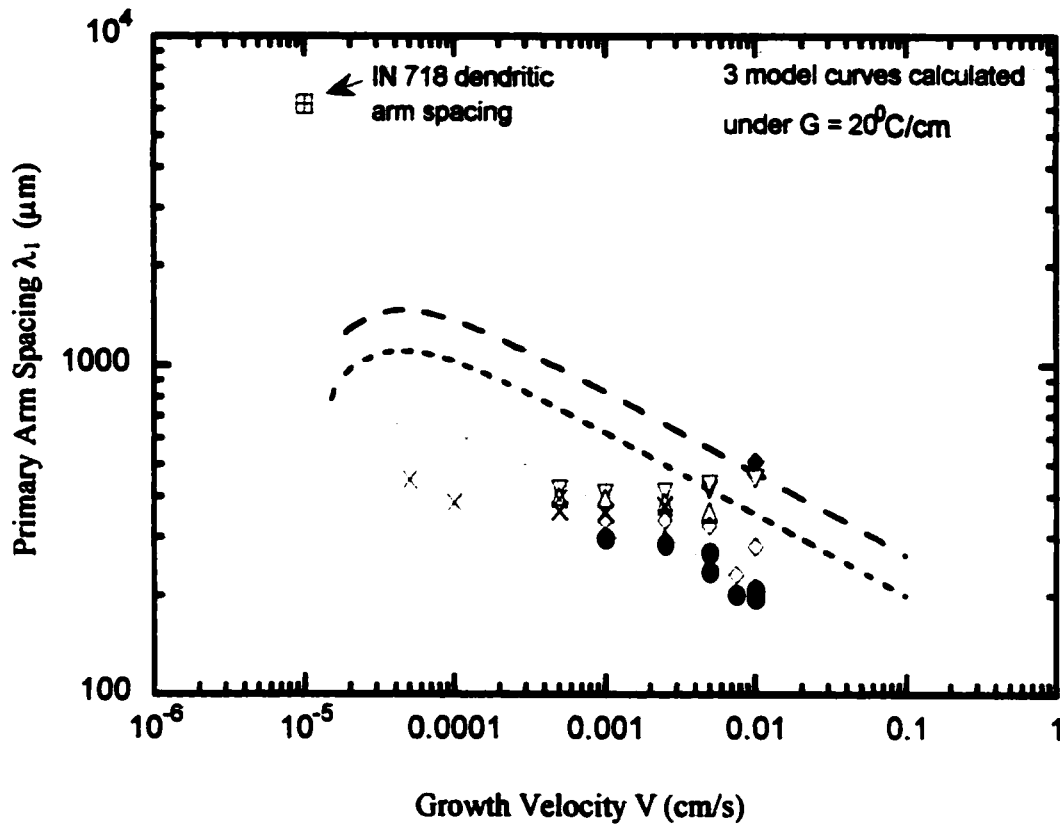
(c) G= 20 °C /cm

Figure 5-12. Comparison of the growth velocity dependence of primary arm spacings of

PWA 1484 with theoretical predictions at various gradients (a) G=100 °C /cm,

(b) 70 °C /cm, and (c) 20 °C /cm
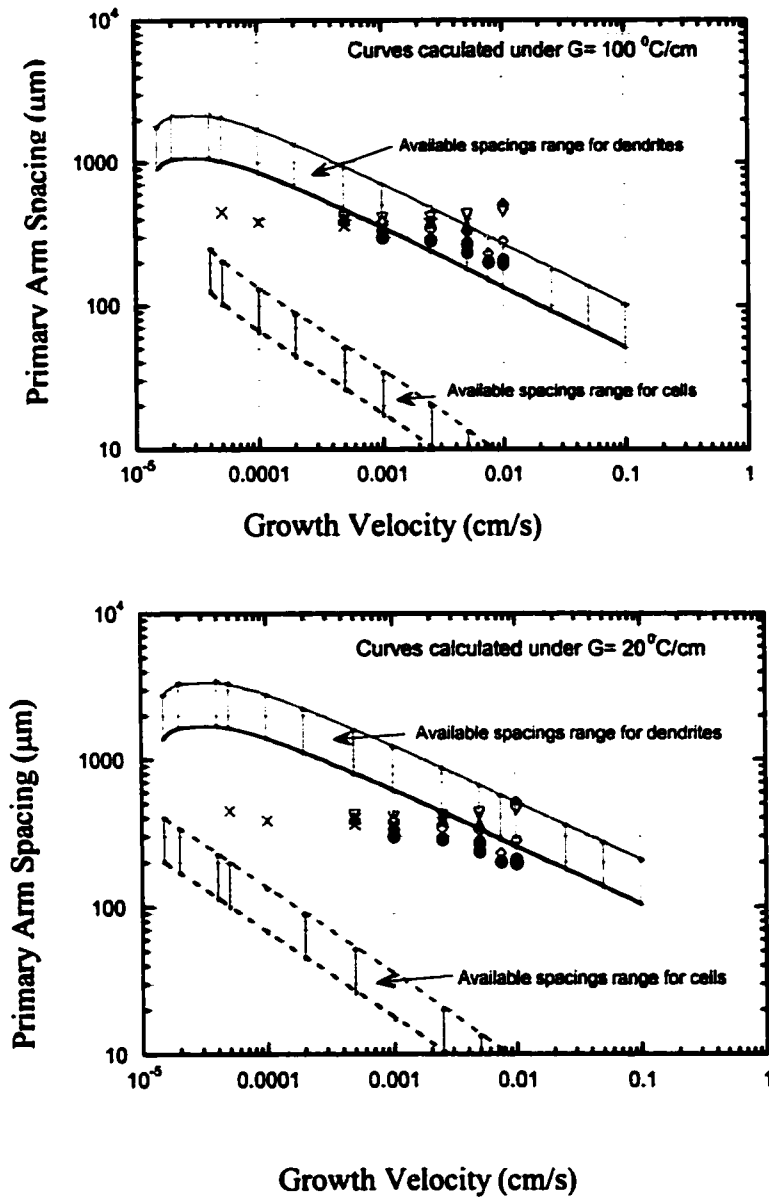
Figure 5-13. Comparison of the growth velocity dependence of the primary spacing of

PWA 1484 with theoretical prediction from numerical models of Lu/ Hunt

(A) Cell and Dendrite transition

It is well known that directional solidification microstructures will transition from planar to cellular to dendritic as the velocity increases for the range of velocities considered here. Previous research [42,43,98,101,102] has shown that at intermediate ranges of velocity, cells and dendrites can co-exist and spacings are intermediate to those predicted for dendritic and cellular growth. McCartney and Hunt[93] reported a discontinuous range between dendrite and cell spacings for their neutrally buoyant Al-Mg-Si alloy directional solidification experiments. Lu and Hunt's[42,43] numerical calculation also showed that two spacing solutions were possible at a given solidification condition: (i) one solution for dendrite growth with a larger value of λ_1, and (ii) another solution for cellular growth with a smaller value of λ_1. The samples grown at low velocities in the present experiments (i.e., 0.001 and 0.0005 cm/s) typically exhibit flanged-cell microstructures (i.e., Figure 5-3a) for all investigated thermal gradients and the observed spacings are between the values predicted by Lu and Hunt's numerical calculation for steady dendritic or cellular growth. Additional theoretical work is clearly needed to address the complex problem of mixed mode growth.

(B) Effects of Off-Axis Heat Flow

The theoretical models proposed by Hunt[40], Kurz and Fisher[42], and Hunt and Lu[43] assume no transverse thermal gradients and neglect the growth of secondary arms.

Only the Ma and Sahm model[44] incorporated the phenomenon of secondary arm growth during dendritic solidification, even though transverse thermal gradients (G_T) are

also assumed to be negligible. In this model, the dendrite tip radius of the side arms was assumed to be equal to the dendrite tip radius of the primary trunks and the growth velocity of the side arms was assumed to be related to the longitudinal growth velocity V by $V_S=V(1-V_C/V)$, where V_C is the critical velocity for planar interface instability. It seems reasonable to assume that if $G_T>0$, then the mean side arm growth velocity would be increased. With such a modification, Ma and Sahm's analysis could be applicable to growth conditions where the dendrites are not aligned with the thermal gradient.

Grugel and Zhou[49] investigated the effects of off-axis heat flow on the primary dendrite spacings for succinonitrile-1.4 and 4.7 wt. pct. water alloys and found good empirical correlation between the spacings and the angular relationship between the dendrite growth direction and the total thermal gradient. Grugel and Zhou defined the orientation angle ϕ such that

$$\tan(\phi) = \frac{G_T}{G} \qquad (5.2)$$

where G_T is the thermal gradient in the transverse direction and G is the thermal gradient in the longitudinal direction. These researchers found that the primary spacings increased with misalignment angle from 0-40° for constant conditions of composition, velocity, and thermal gradient. For increasing angles from 50-70°, the secondary arms assumed the roles of primary arms and the spacings rapidly decreased. Grugel and Zhou correlated λ_1 with the heat flow geometry and found for the succinonitrile-1.4 wt. pct. water alloy that

$$\lambda_1(\phi) = \lambda_1(\phi = 0) + 120\tan^2\phi \quad (\mu m) \qquad (5.3)$$

where the 120 factor is an empirically determined fitting parameter. Thus the primary

spacings of the samples in the misaligned thermal field were equal to the theoretical

spacings during aligned growth (ϕ=0) plus a correction factor that depended upon the

misalignment angle ϕ. Although the data were limited, Grugel and Zhou found a

correction factor of approximately $260\tan^2\phi$ for misaligned growth in succinonitrile-4.7

wt. pct. water alloy. Thus the factor in front of the $\tan^2\phi$ term does not appear to be

constant. More work on the basis of this factor is clearly needed.

High growth velocities during directional solidification can move a sample's

mushy zone down and out of the adiabatic zone, thus producing non-negligible transverse

(i.e., radial) thermal gradients, especially when the axial thermal gradients being utilized

are themselves quite low. In this case, the growth interface changes to a concave surface

instead of a flat plane (Figure 5-14). Heat flux lines are not straight outside of the

adiabatic zone where a radial thermal gradient exists. This radial gradient could promote

and accelerate the growth of secondary arms, which, in turn, would block and suppress

the growth of neighboring primary arms and enlarge the primary arm spacings.

An experiment was conducted to investigate the longitudinal (G) and radial (G_r)

thermal gradients in the Bridgman-type furnace for a number of withdrawal velocities.

Thermocouples were placed along the centerline and along the outside of a sample. The

test was performed at a furnace setting of 1200 °C. Figure 5-15 shows typical cooling

curves measured during testing. Analysis of thermocouple data shows that when

$G < 30$ °C /cm, the ratio of transverse to longitudinal thermal gradient (G_r /G) varied

(a)

(b)
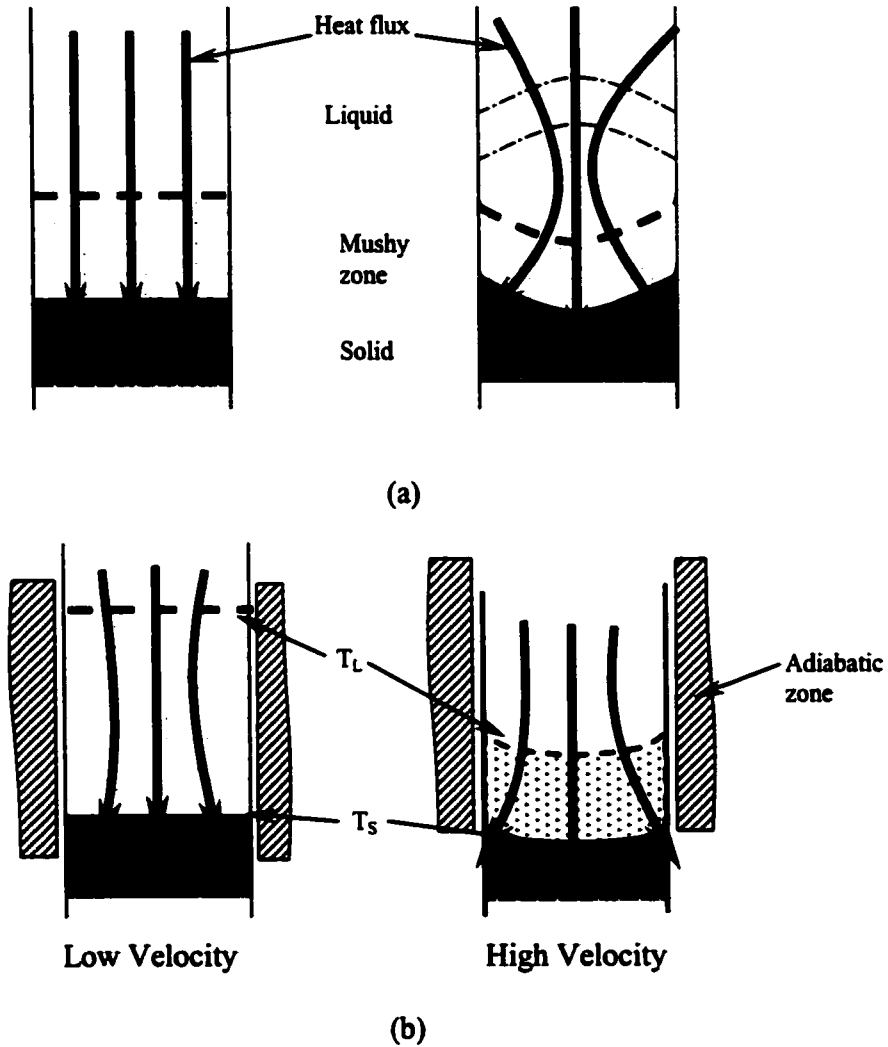
Figure 5-14. (a) Schematic mechanism of growth interface morphology transiting from

flat to concave or convex caused by heat flux directions and mushy zone position. (b) the

displacement of the position of mushy zone at adiabatic zone at various velocities, and

corresponding radial thermal gradients at mushy zone.
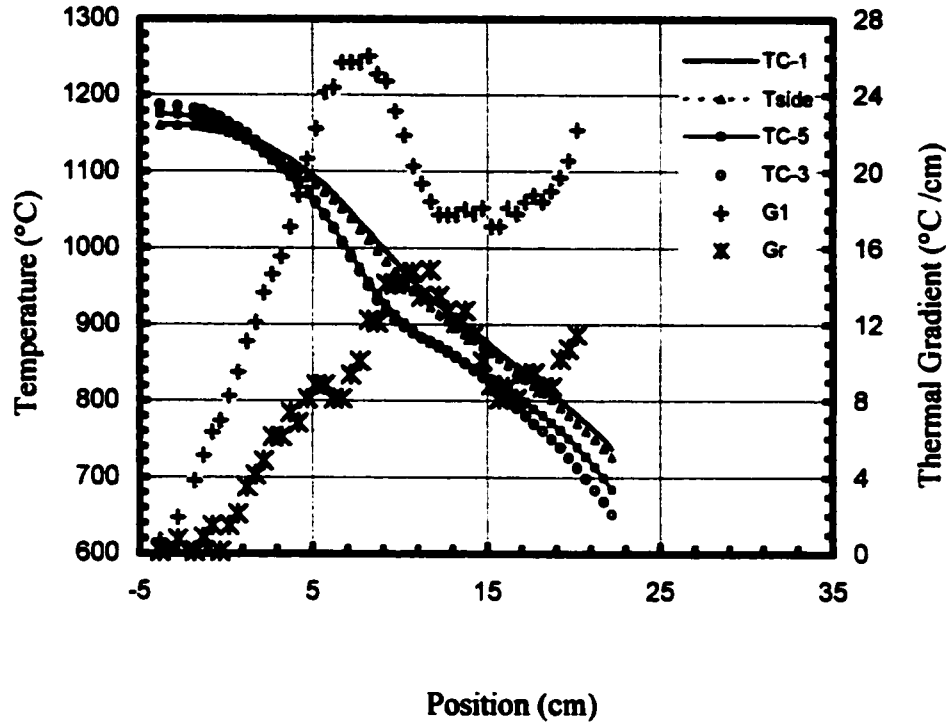
Figure 5-15. Cooling curve profiles showing one transverse thermal gradient at radial

direction of a cylindrical sample. The sample was withdrawn from hot zone at condition

of 27°C /cm (G) and 0.01cm/s (V). (G_T: radial gradient, G: axial gradient). x=0 is the exit

position of hot zone.

from 0.4, 0.3, and 0.2, respectively for velocities of 0.01, 0.005, 0.001 cm/s. Thus G_r/G increased for increasing velocities, as expected.

Significant radial thermal gradients should increase the primary spacings along the outside edge of the samples. Figure 5-16(a) shows the spacing distribution for a high velocity sample and a low velocity sample grown at low imposed gradient $G \sim 20°C/cm$. The measurements were performed along two mutually perpendicular diameters. The top two curves (diamonds) were measured on a sample grown at 0.01 cm/s. The bottom two curves (triangles) represent the spacing distribution from a sample grown at 0.0005 cm/s. The high velocity sample exhibits the greatest radial thermal gradient and the greatest variation in primary dendritic arm spacing, as expected. The low velocity sample exhibits the smallest radial thermal gradient and uniform primary dendrite arm spacing. Figure 5-16(b) shows additional spacing data including data from high G_L samples. At high G_L (>30°C /cm), the observed dendritic arm spacings were uniform regardless of velocity.

Misalignment of growth direction and thermal gradient provides for enhanced growth of the secondary arms that find themselves rotated closer to the maximum thermal gradient. Conversely, secondary arms on the opposite side will find their growth retarded since they are rotated away from the maximum thermal gradient. In the limit of a complete rotation through 90°, the secondary arms would obviously become primary arms. Such conditions could be realized by rapid withdrawal of a sample from the furnace followed by air cooling. Quantitative theoretical treatment of the effects of such misalignment would require numerical modeling the coupled solute/ thermal diffusion fields at the dendrite tips.
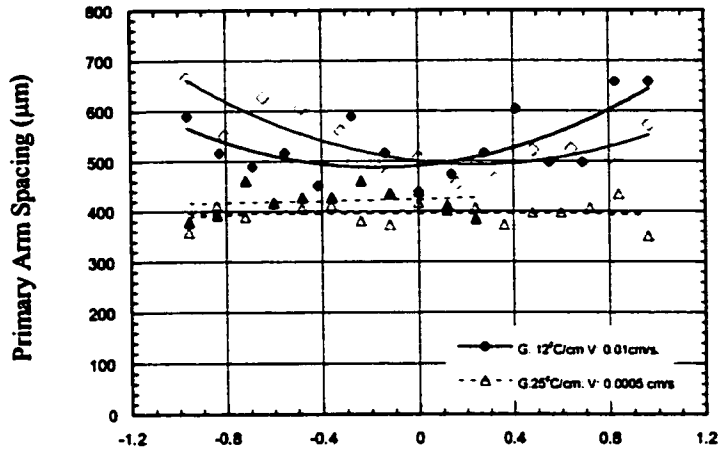
(a) Position Along Diameter Lines (cm):
x=0 marks the cylinder center
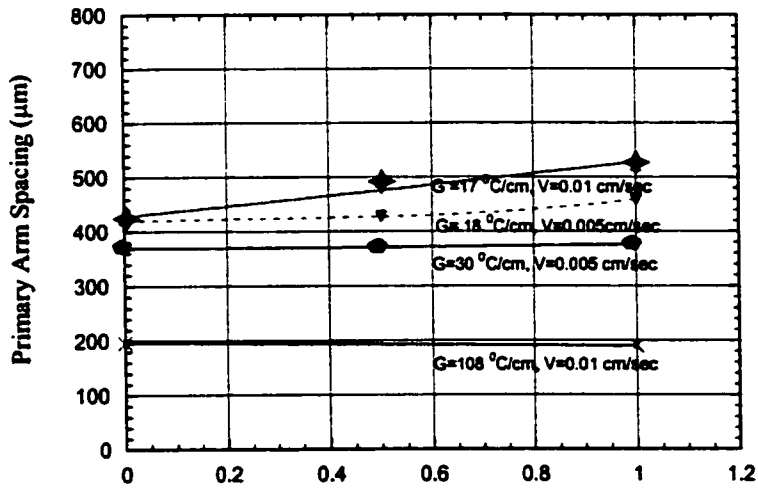
(b) Position Along Diameter Lines (cm):
x=0 marks the cylinder center

Figure 5-16. Illustration of existing radial thermal gradient effects on the primary spacings along outside edge of samples: (a) Diamond marks: arm spacing measured from sample grown at 12°C /cm, 0.01cm/s; Triangle marks: arm spacing measured from sample grown at 20°C /cm, 0.0005cm/s; (b) Comparison of arm spacing distributions along diameter lines for samples grown at various solidification conditions

5.1.3 Secondary Dendritic Arm Spacing (λ_2) (SDAS)

Figure 5-17 shows the relationship of secondary dendritic arm spacings λ_2 with the cooling rate. This relationship indicates a monotonic decrease in λ_2 with increasing cooling rate. By using regression analysis, the exponent (m) of cooling rate $\lambda_2 = C(GV)^m$ was found to be -0.38, which is close to the theoretical result and previously published data for nickel-based superalloys (-0.33)[13, 34]. Figure 5-17 also contains other published data of superalloys, which are in good agreement.
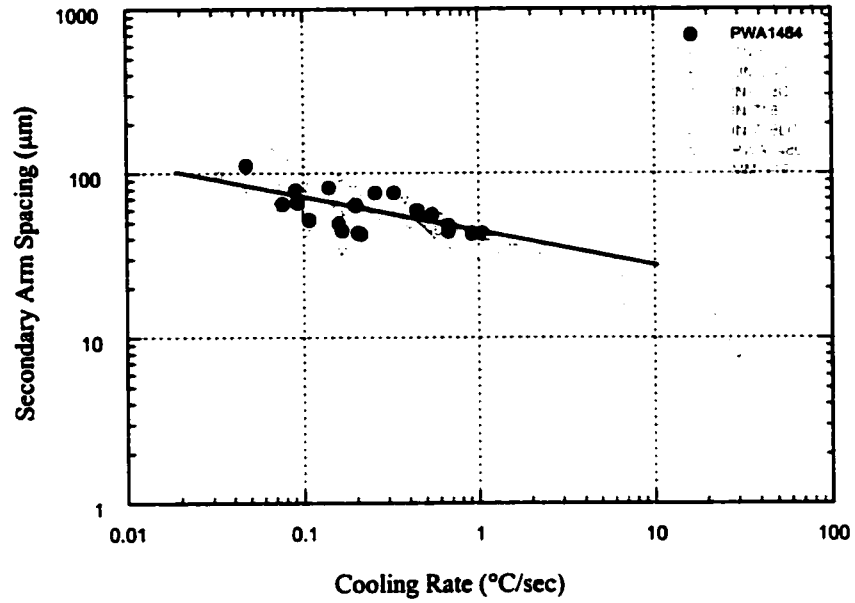
Figure 5-17. Illustration of secondary arm spacings with cooling rate for DS PWA 1484

and other nickel–based superalloys

5.1.4 Precipitated Phases in As-cast DS PWA 1484

As indicated in the cooling curves (Figure 5-1 and graphs in the Appendices), after the solidification from $T_L = 1395°C$ to $T_S = 1335°C$, the sample was continuously exposed to high temperature environment for a certain time, the amount of time of which samples exposed to high temperature can be determined by the thermal gradient and the growth velocity of sample. When the growth velocity is lower, the sample is exposed to the high temperature environment for longer time and the microstructure exhibits more coarsening. However, the cooling process after solidification would not affect the primary dendritic/cellular arm spacings that are determined during solidification.

(5.1.4.1) γ' Precipitate Formation

There are two types of γ' constituents in the directionally solidified PWA 1484 superalloy: A) the γ' precipitated from γ matrix (i.e., the dendrites) to relieve the over-saturated γ phase matrix during the cooling process directly after solidification; B) the γ' particles nucleate from the residual eutectic melt and are present in the inter-dendritic region. The size and morphology of both γ' constituents vary with the cooling rate as reported.

(A) γ' Precipitates in the Cells/Dendrites

Figure 5-18 (a, b) illustrates γ' precipitates in one sample, which was grown for approximately 6 cm at G= 40°C /cm, V= 0.01 cm/s and then quenched in water. Figure 5-18(a) shows the microstructure located at the tip of the dendritic trunks of mushy zone.
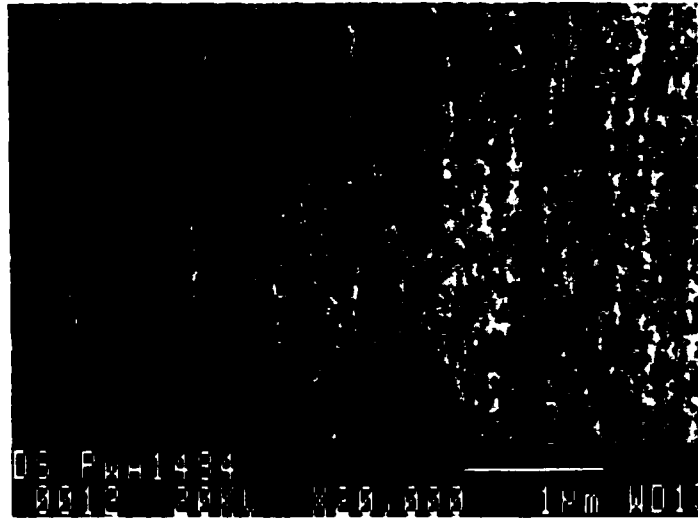
(a)
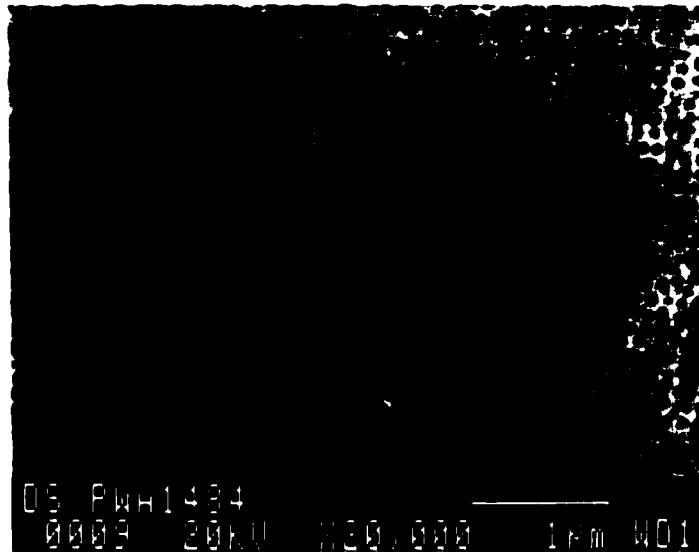
(b)

Figure 5-18. γ′ precipitates located at the tip of (a) dendritic trunks and (b)

interdendritic region of mushy zone of the PWA 1484 sample grown about 6 cm at G=

40°C /cm, V= 0.01 cm/s and quenched in water.

Fine uniformly distributed spheroid γ' precipitates were formed. These initial spheroidal

γ' precipitates are believed to have nucleated from the solid matrix during quench instead

of from the melt. The first deposited dendritic/cellular matrix of PWA1484 should be

only γ phase. Bhambri et al[63] reported similar phenomenon in their study of DS Inconel

713C alloy. In their study, the uniformly distributed spheroidal γ' precipitates were also

observed at the tips of the dendritic trunks. However, there were no γ' precipitates

observed in splat-cooled samples. Figure 5-18 (b) shows the microstructure at the tip of

interdendritic region of the mushy zone. It shows larger γ' precipitates were formed

compared with those shown in Figure 5-18(a).

Figure 5-19(a) displays the microstructure located at the center of dendritic trunks

from a sample grown at G= 15°C /cm, V= 0.01 cm/s and cooled in the air. It can be seen

that the γ' precipitates exhibit a cuboidal geometry. Figure 5-19(b) shows the

microstructure at interdendritic regions, where neighboring individual γ' precipitates have

coalesced together and the geometry is more irregular.

Figure 5-20(a, b) shows the γ' precipitates in the dendritic trunks and inter-

dendritic region from a sample grown at G= 28°C /cm and V= 0.0005 cm/sec and cooled

in air. In this case, γ' precipitates are large irregular particles with the interdendritic

particles being significantly larger than the dendritic particles.

(a)
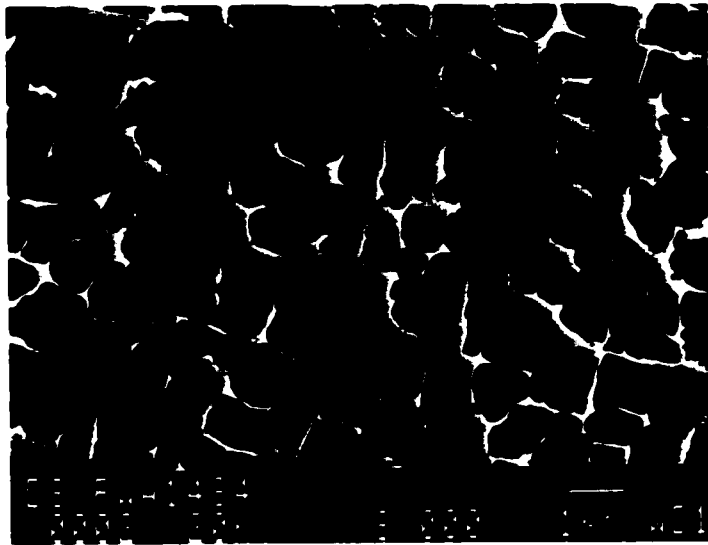
(b)

Figure 5-19. γ′ precipitates located at the tip of (a) dendritic trunks and (b) interdendritic

region of mushy zone of a PWA 1484 sample grown at G= 15°C /cm, V= 0.01 cm/s and
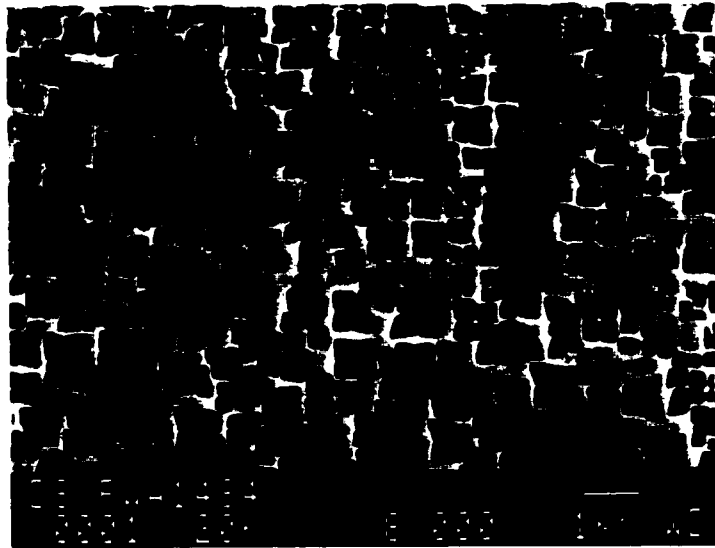
cooled in air

(a)

(b)
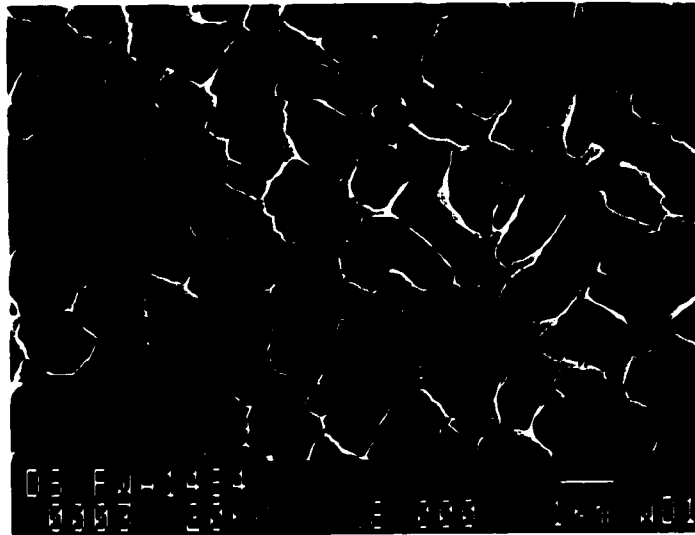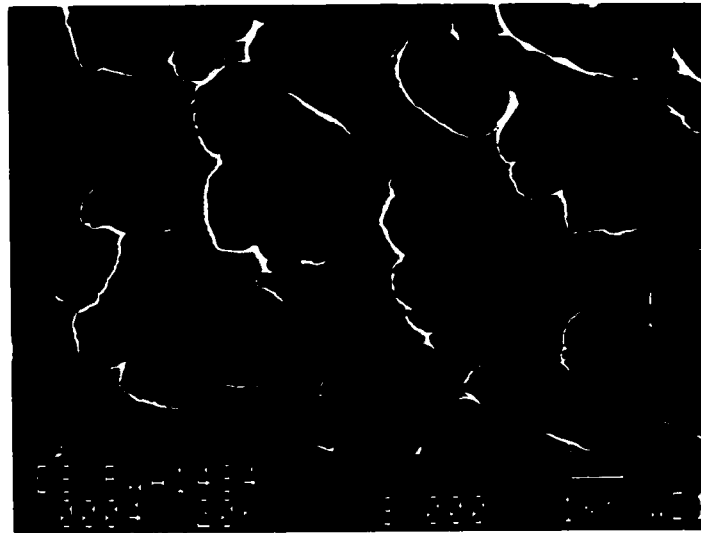
Figure 5-20. γ′ precipitates located at the tip of (a) dendritic trunks and (b)

interdendritic region of mushy zone of a PWA 1484 sample grown at G= 28°C /cm,

V=0.0005 cm/s and cooled in air

(B) Interdendritic Precipitates

Previous investigations have shown that the eutectic pools are formed in very short temperature range ($\Delta T = 5K$) above the eutectic temperature[62,73]. When the cooling rate is high enough, the solute-rich residual liquid is supercooled to eutectic temperature, and a high density of eutectic ($\gamma'+\gamma$) nuclei are produced. During solidification, those nuclei form the small fan-like eutectic microstructures with lamellar γ phase inside. Figure 5-21 shows the typical eutectic $\gamma'+\gamma$ observed in a sample, which was grown at G= 15°C/cm and V=0.01 cm/s.

When the cooling rate is comparatively low and the local solidification time becomes longer, the eutectic microstructure can become divorced, as shown in Figure 5-22(a, b). The difficulty of nucleating γ' allows the γ phase to "overshoot", taking Ni and other γ forming elements from the eutectic liquid, and leaving the residual liquid rich in γ' forming elements.

Neither normal nor divorced eutectics are desirable in the production of DS superalloy components. Both are detrimental to mechanical properties of the alloy since they consume necessary strengthening elements for alloy. Successful heat treatment after solidification is required to dissolve these phases. Eutectic constituents can also be suppressed by eliminating segregation during directional solidification.
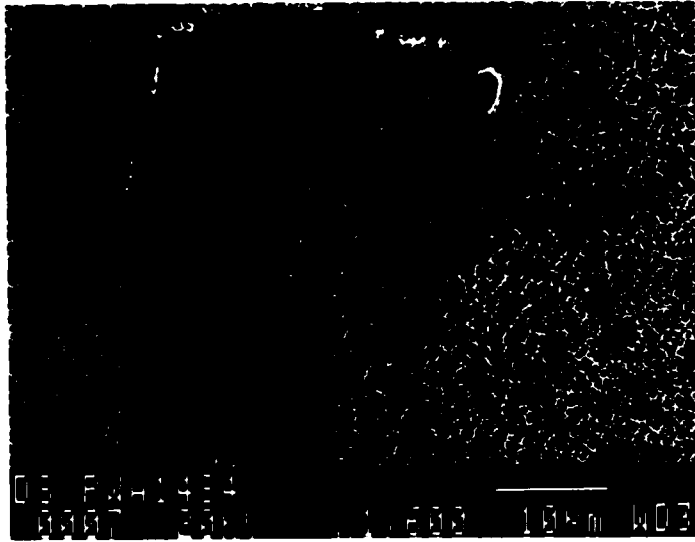
Figure 5-21 Typical eutectic γ'+γ pool located at interdendritic region from a

sample grown at G= 15°C/cm and V=0.01 cm/s and cooled in air
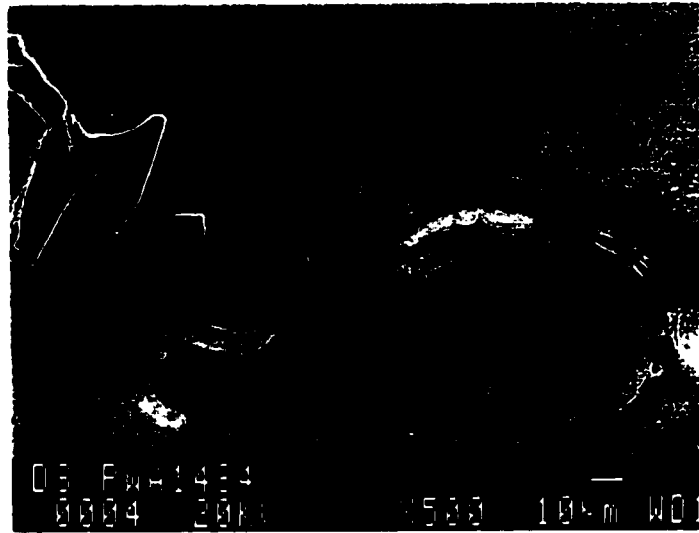
(a)
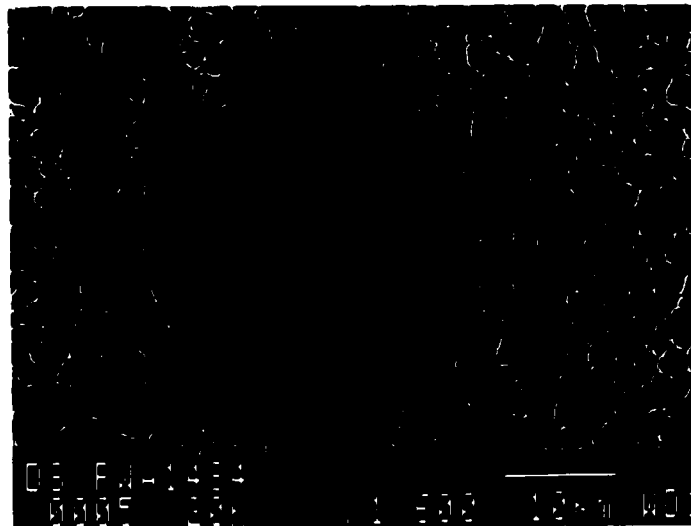
(b)

Figure 5-22. Typical divorced eutectic γ′ colony observed in a sample grown at

G = 28°C /cm, V=0.0005 cm/s and cooled in air. (a) γ′ with a few of lamellar γ phase; (b)

γ′ without lamellar γ phase.

(5.1.4.2) Metal Carbides

Figures 5-23 (a, b, c) show some typical carbides (MC) observed in the DS PWA1484 superalloy samples. MC carbides form only in the interdendritic areas. Compositional data from EDS experiments indicated M = Ta for as-cast PWA 1484(see Table 5–3 at page 102). The morphology and size of the carbides are dependent on the cooling rate during and after solidification. Carbides can be classified in several types in terms of their morphology, i.e., script, plate-like, or blocky. Generally, at high growth velocities, the carbides have smaller sizes and exhibit a script morphology. At low growth velocities, the alloys are exposed to high temperature for longer times and carbides will coarsen to larger sizes with blocky or plate-like geometries elongated in the growth direction.

When the velocity is sufficiently low (solidification will be near planar interface conditions), the formation of carbides will be suppressed and only a few large blocky carbides are present (Figure 5-23(c)). These carbides are occasionally "connected" by very fine MC chains (Figure 5-24), which existed along the grain boundaries. This is because the growth interface of the sample grown at 0.00005 cm/sec does not exhibit a perfect planar interface, so there are still shallow valleys along the interface and grain boundaries. Those valleys and grain boundaries become solute-rich areas and provide favorable chemical conditions for carbide formation.

(a) V= 0.01 cm/s

(b) V=0.0005 cm/s

Figure5-23 (a, b) Typical metal carbide morphologies observed in samples grown

at 0.01 cm/s (script) and 0.0005 cm/s (plate-like)
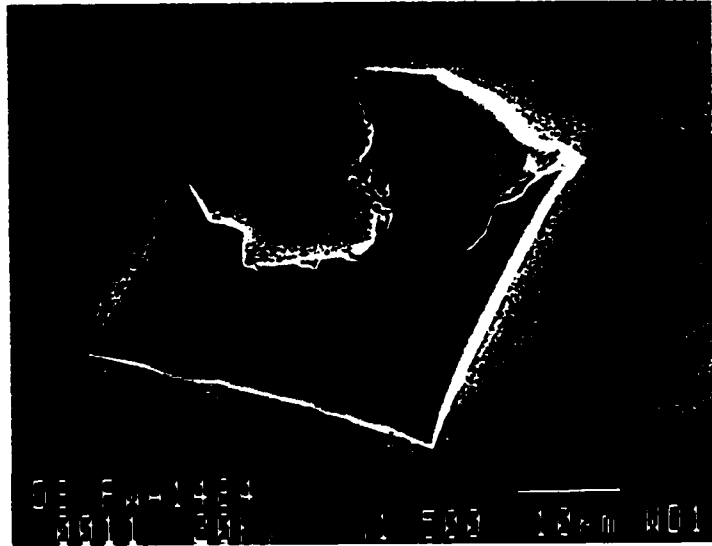
Figure5-23 (c) Typical metal carbides morphologies observed in a sample grown

at 0.00005 cm/s (blocky)

Figure 5-24 Small carbide chain along grain boundary observed in a sample

grown at V=0.00005cm/s

The velocity dependence of the present MC geometry indicates that the solidification variables have a significant effect on carbide growth. The longer the cooling time after solidification (i.e., lower cooling rate), the larger the size and the more regular geometry carbides will exhibit.

5.2 Segregation Effects on Freckle Defect Formation

5.2.1 Segregation in As-cast DS PWA 1484

Elemental distributions in as-cast DS PWA 1484 were measured with energy

dispersive spectroscopy (EDS) using a JEOL 840 scanning electron microscope on

transverse and longitudinal sections of an as-cast sample. The composition of dendrite

trunks, interdendritic regions, and other second phases (MC, γ', γ) were analyzed on a

sample grown at V = 0.0005cm/s and G = 40 °C/cm. These results are listed in Table 5-3.

The EDS results show that Ta, Mo and Al segregate to the interdendritic regions

while W and Re segregate inversely to the dendrites. The carbides are found to be mainly

tantalum carbides. Due to the segregation, the compositions of γ' precipitates and γ

matrix in the dendritic trunks are not the same as those in the interdendritic regions. The

equilibrium partition ratio (κ) can be used to describe the degree of segregation during

alloy solidification. In this study the approximate partition ratio is estimated in terms of

$\kappa = C_s/C_L$ where C_s is the concentration of an element at the center of a dendrite and C_L is

the concentration at the center of the interdendritic region. These results are listed in

Table 3 and exhibit good agreement with published data for simple binary nickel-base

alloys.

Figure 5-25 shows the results of composition analyses from different transverse

sections from the bottom to the top of one as-cast sample. These results indicate that little

macrosegregation occurred during solidification. This indicates minimal convection

within the sample during solidification.

Table 5-3. Composition distribution data on as-cast DS PWA 1484

(V= 0.0005 cm/s and G = 40 °C/cm.)

	COMPOSITION							
	Al	Cr	Co	Mo	Ta	W	Re	Ni
nominal	5.66	4.96	9.88	1.89	8.74	5.86	2.98	60.03
average	4.88	5.51	9.17	2.31	9.11	8.09	3.45	57.49
dendrite($\gamma+\gamma'$)	4.51	5.28	9.57	1.93	7.43	9.55	4.7	57.02
dendritic γ	2.23	8.77	12.6	3.09	2.77	11.6	8.59	50.29
dendritic γ'	6.28	2.8	7.15	1.16	10.7	7.25	1.41	63.25
inter-dend.($\gamma+\gamma'$)	5.07	5.65	9.07	2.24	10.4	7.39	2.58	57.62
inter-dend. γ	2.57	10.1	12.1	4.89	4.03	8.84	5.78	51.67
inter-dend. γ'	6.61	2.35	6.53	0.87	15.3	5.05	0.19	63.19
eutectic γ'	6.85	2.04	6.37	0.82	17.6	3.62	0.29	62.6
carbide					95.9			4.14
partition κ	0.89	0.93	1.06	0.86	0.72	1.29	1.82	
partition κ^*	0.91	1.09	1.06		0.77	1.17	1.47	

*average alloy composition (wt %): data measured at Auburn University using EDS.

*Partition ($\kappa=C_S/C_L$): effective equilibrium partition ratio calculated in this work.

*Partition (κ^*): effective equilibrium partition ratio determined by Ref [26]
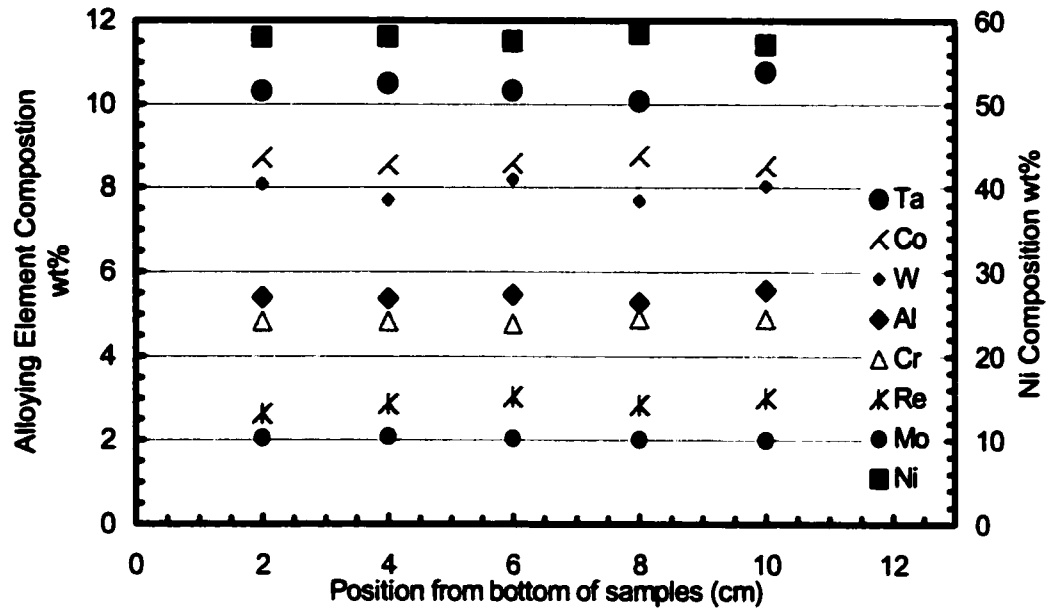
Figure 5-25. The result of composition analyses at different transverse sections from the

bottom to the top of a sample cast at V= 0.0005 cm/s and G = 40 °C/cm

5.2.2 Casting Defect Freckling Experiments

A series of PWA 1484 cylindrical samples were directionally solidified under a wide range of parameters (Table5-1). Figure 5-26 shows the typical polycrystalline, well-aligned macrostructure of those samples. Higher growth velocities typically yielded smaller grain sizes in the alloy. When grown at a velocity of 0.00005 cm/s (G=40°C/cm), a sample with bi-crystals was produced. At high velocity of 0.01-0.005 cm/s, many sliver and isolated equiaxed grains were formed at the perimeter surface of the samples (Figure 5-26). The large supercooling caused by high velocity enables equiaxed grains to nucleate in competition with the primary dendrites. Such a grain could become a sliver defect if it were misaligned with growth direction.

Industrial experience with this alloy indicates that freckle defects are a common problem. However, no freckle chains were observed on any of the cylindrical PWA 1484 samples. Since freckle chains are believed to result from buoyancy perturbations at the growth front, additional directional solidification experiments were conducted with special measures that were utilized to attempt to enhance potential buoyancy instabilities and form defects.

(5.2.2.1) Non-continuous growth

Non-steady growth conditions (starting and stopping of the mushy zone) were believed to contribute to the buoyancy instabilities that cause freckle chain defects. Three growth velocities, namely, 0.01, 0.001, 0.0005 cm/s were selected to run the non-continuous growth directional solidification. In all three cases, furnace temperature was set at 1550°C and booster furnace was above 1000°C to keep the thermal gradient as low as possible. As the samples were withdrawn from the furnace, unlike previous operations, withdrawal occurred for a given distance (i.e., 1 inch), then stopped for 7 min., and
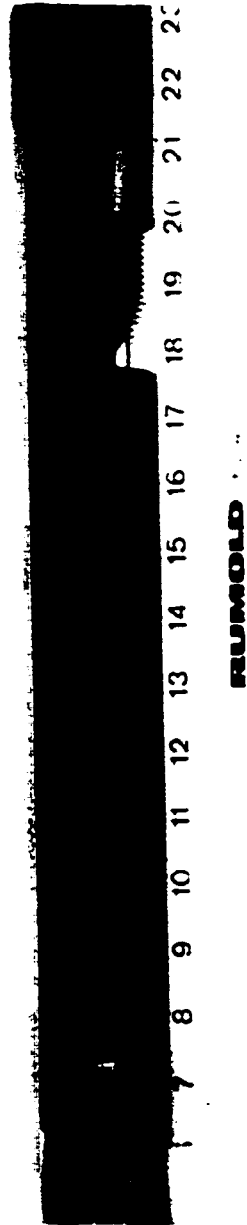
Figure 5-26. Illustration of one typical macrostructure of as-cast DS PWA 1484

(V=0.01cm/s; G= 25 °C /cm)

then withdrawal resumed at the same velocity and distance until suspended again and so on, until the whole sample moved out of the furnace. Figure 5-27 shows the typical cooling curves for non-continuous solidification.

(5.2.2.2) Mechanical Perturbations During Solidification

When a sample is continuously withdrawn from furnace, a mechanical perturbation was applied by shaking the retort and sample assembly. In this way, mechanical perturbations were created at the interface. Three growth velocities, namely, 0.01, 0.001, 0.0005 cm/s were selected, and in all three cases, furnace was set at 1550°C and booster furnace was above 1000°C. The retort was shaken 5-10 times repeatly by hand at every displacement of 2.54 cm (1 inch) until the whole sample was withdrawn from the furnace. The angles of the retort were about 5° to the vertical during shaking.

(5.2.2.3) Solidification Perturbations due to Change of Section Size

Figure 5-28 illustrates section size changes of a cylindrical sample. When a solid/liquid interface goes through the decreased cross section, the heat flux would be enhanced and there is an increase in longitudinal gradient G, whereas at the increased cross section, the strong heat flux would be relieved and hence a decrease in gradient G. Under either condition, the equilibrium status should be disturbed, and perturbation at the interface would be expected. Two growth velocities, namely, 0.01, 0.001cm/s were selected, and in both cases, the furnace was set at 1550°C and booster furnace was above 1000°C.

However, no freckle defects were observed on the surface of any of these samples. It is obvious that these attempts were not sufficient to produce the freckles.
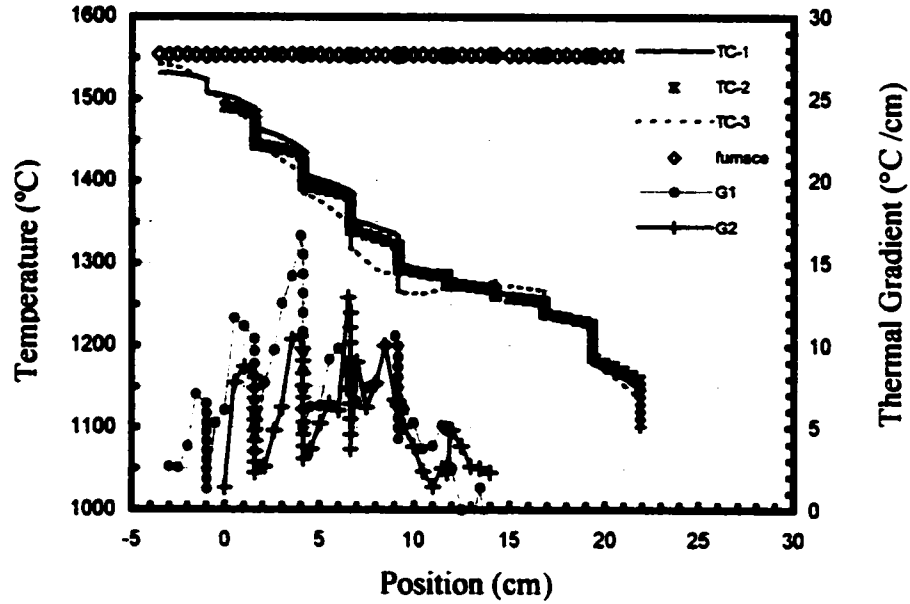
Figure 5-27. Typical thermal cooling curves for non-continuous growth DS experiment of PWA 1484 (a sample with withdrawal V=0.01cm/s and G ~ 5~10°C/cm). x=o represents the exit position of hot zone.
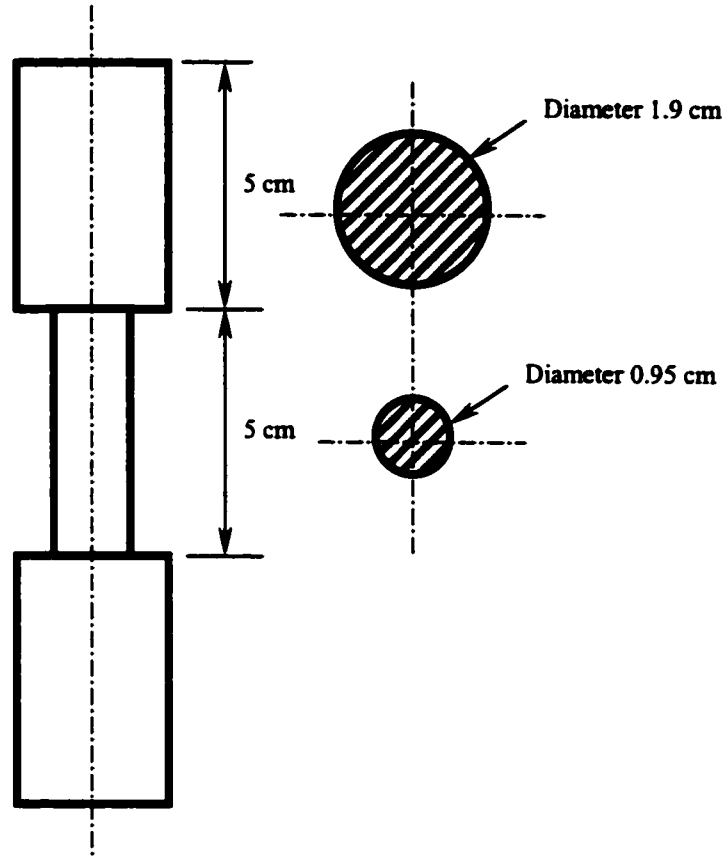
Figure 5-28. Illustration of cylinder sample of PWA 1484 with section size changes

(5.2.2.4) Directional Solidification of MM247

MM247 is also a nickel-based superalloy used commercially to produce turbine blades. Nominal and actual compositions of MM247 are listed in Table 4-1 (at the page 38). MM247 cylindrical bars were remelted and directionally solidified under the conditions listed in Table 5-4. Samples were macro-etched with 100ml HCL + 10 ml H_2O_2. Although freckle chains were observed at the surface of the sample (Figure 5-29) grown at V= 0.0005 cm/s, the other two higher velocity samples did not have freckle chains on the surface.

Figures 5-30(a, b, c) illustrates transverse section microstructures of directionally solidified MM247. The process parameters are also marked below the pictures. It shows that as-cast DS MM247 has very similar microstructural features as that of DS PWA1484. At high growth velocity i.e., 0.005cm/s, well-developed dendrites with secondary branch arms are formed in the sample, while the dendritic trunks transition to simple cross dendritic and flanged-cellular morphologies when the velocity decreases to 0.0025 and 0.0005 cm/s, respectively.

Whitesell[103] studied the arm spacing development of DS MM247. In that investigation, MM247 cylinders were remelted and directionally solidified in a Bridgman type furnace. Figures 5-31 and 5-32 illustrate the dependence of arm spacings (λ_1 and λ_2) on the process parameters $G^{-0.5}V^{-0.25}$ and cooling rate GV (°C/s). Obviously, there is no significant difference in λ_1 and λ_2 between MM247 and PWA1484.

Table 5-4. MM247 directional solidification process parameters and microstructural

results

	Run #1	Run #2	Run #3
Velocity V (cm/s)	0.005	0.0025	0.0005
Thermal gradient G (°C/cm)	24	32	35
Cooling rate (°C/s)	0.12	0.08	0.0175
Primary arm spacings (λ_1 μm)	470	500	495
Secondary arm spacings (λ_2 μm)	58	85	na
Temperature at hot zone (°C)	1600	1600	1600
Temperature at booster furnace (°C)	~1000	~1000	~1000
Freckle defects	no	no	yes
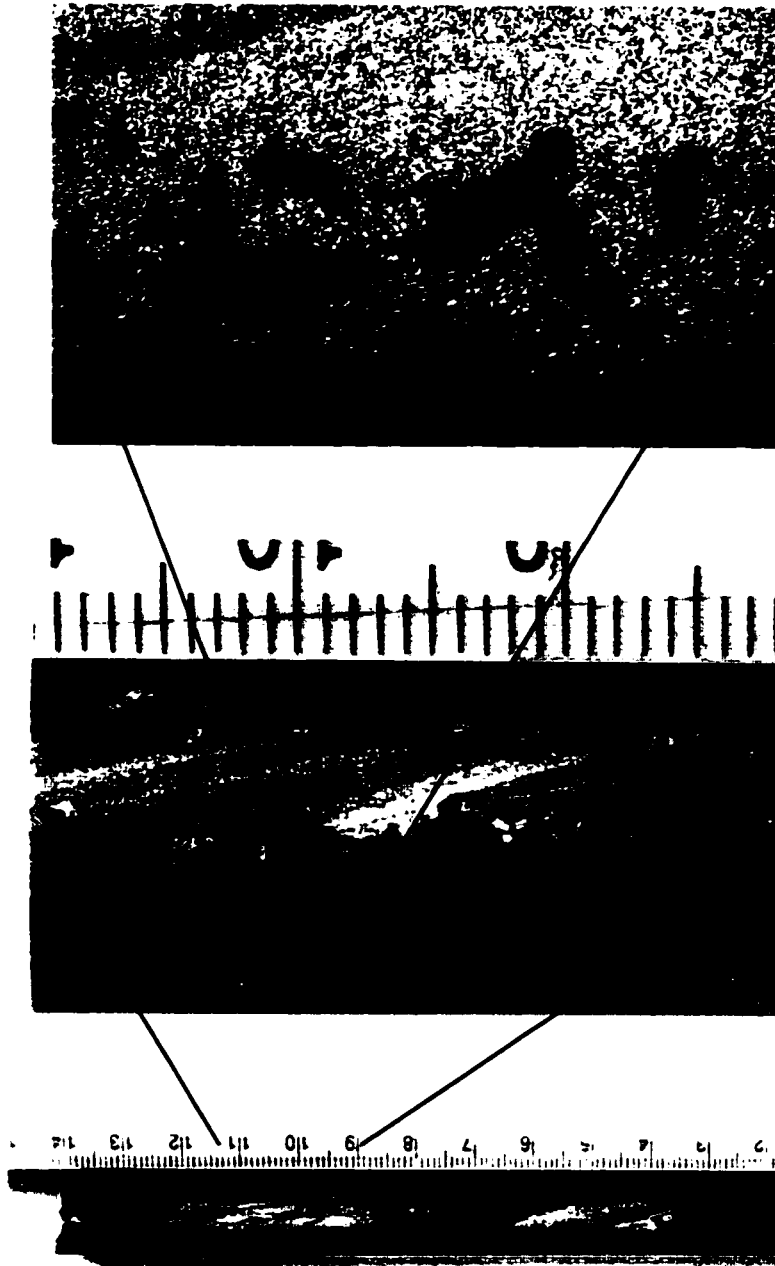
Figure 5-29. Illustration of freckle chains observed on the surface of DS MM247 sample
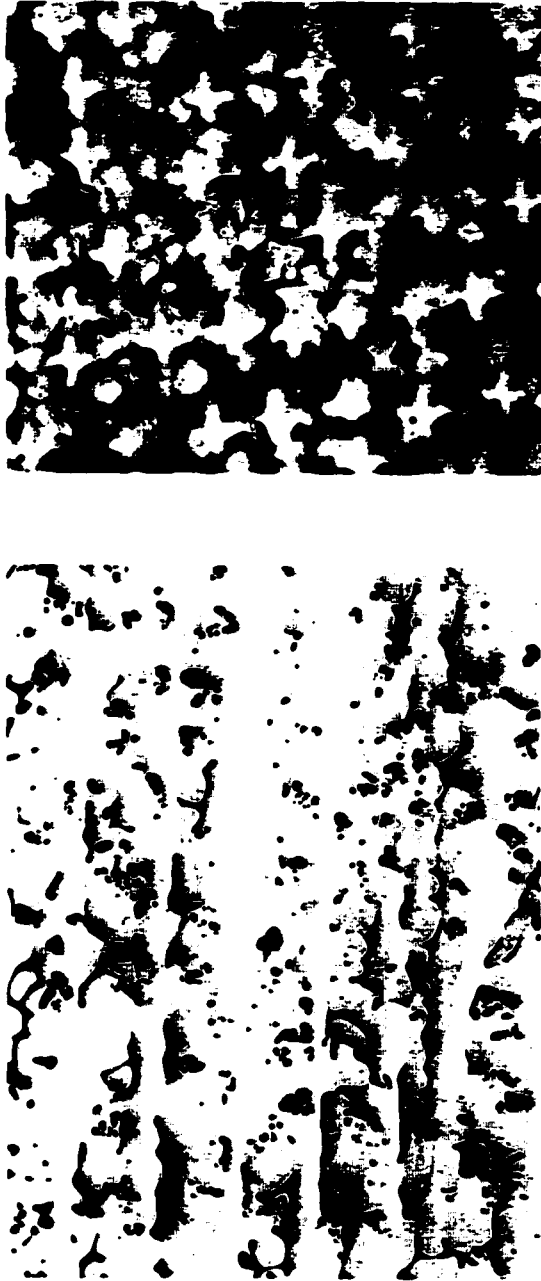
Figure 5-30(a). Transverse section and longitudinal section microstructure of DS MM247

sample grown at V=0.0005 cm/s and G=35 °C /cm (400μm: ▬▬▬)
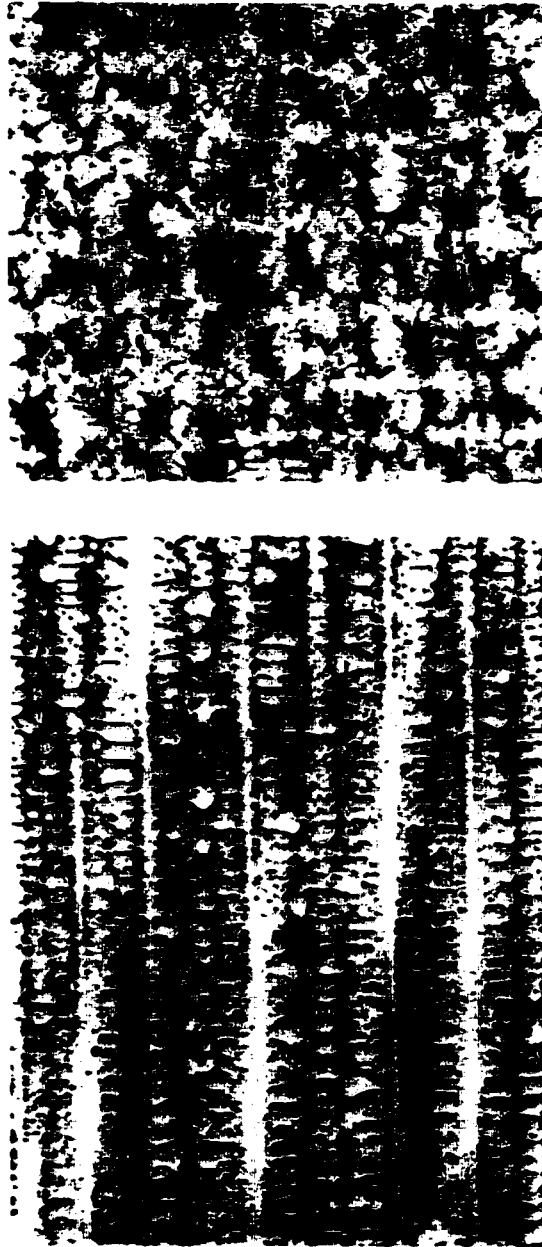
Figure 5-30(b). Transverse section and longitudinal section microstructure of DS MM247

sample grown at V=0.0025 cm/s and G=32 °C /cm (400μm: ▬▬)
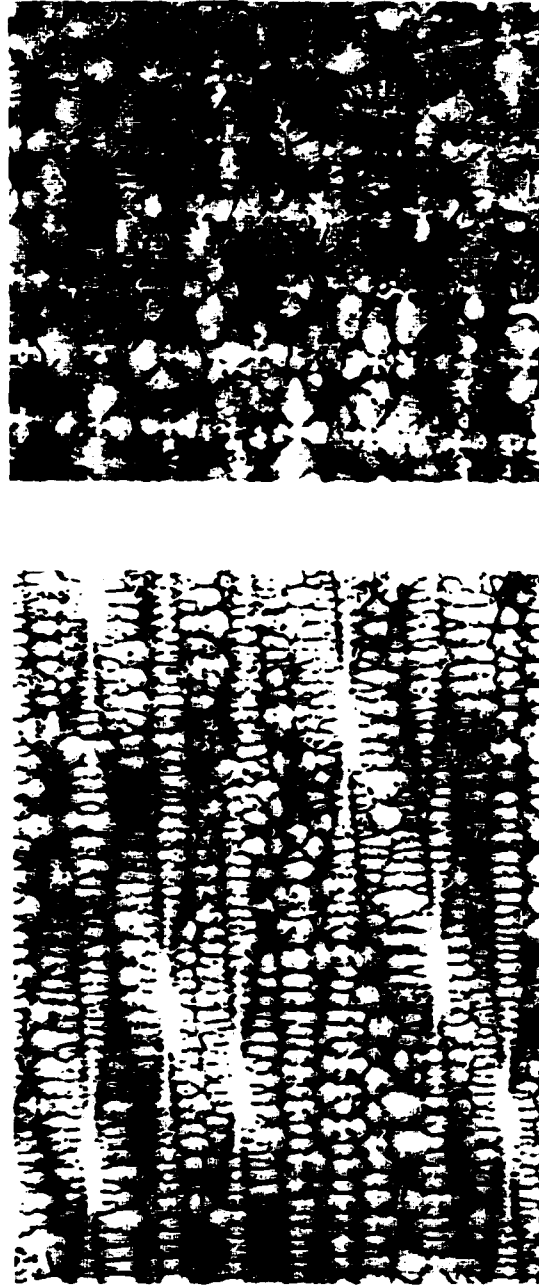
Figure 5-30(c). Transverse section and longitudinal section microstructure of DS MM247

sample grown at V=0.005 cm/s and G=24 °C/cm (400μm: ▬▬▬)
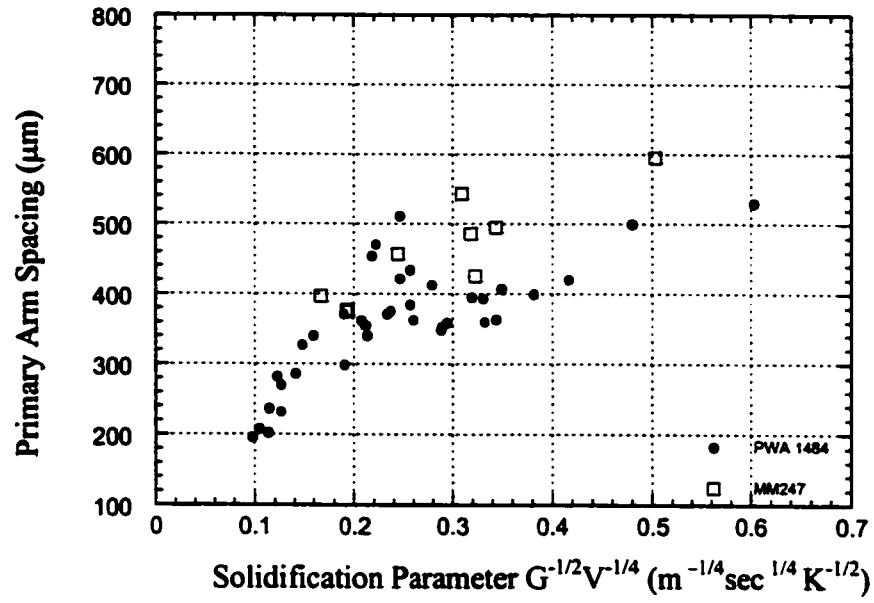
Figure 5-31 Primary dendritic and cellular arm spacings of DS MM247 and PWA1484

correlated with solidification parameter $G^{-0.5}V^{-0.25}$ $(m^{-1/4} \, sec^{1/4} \, K^{-1/2})$ [103].
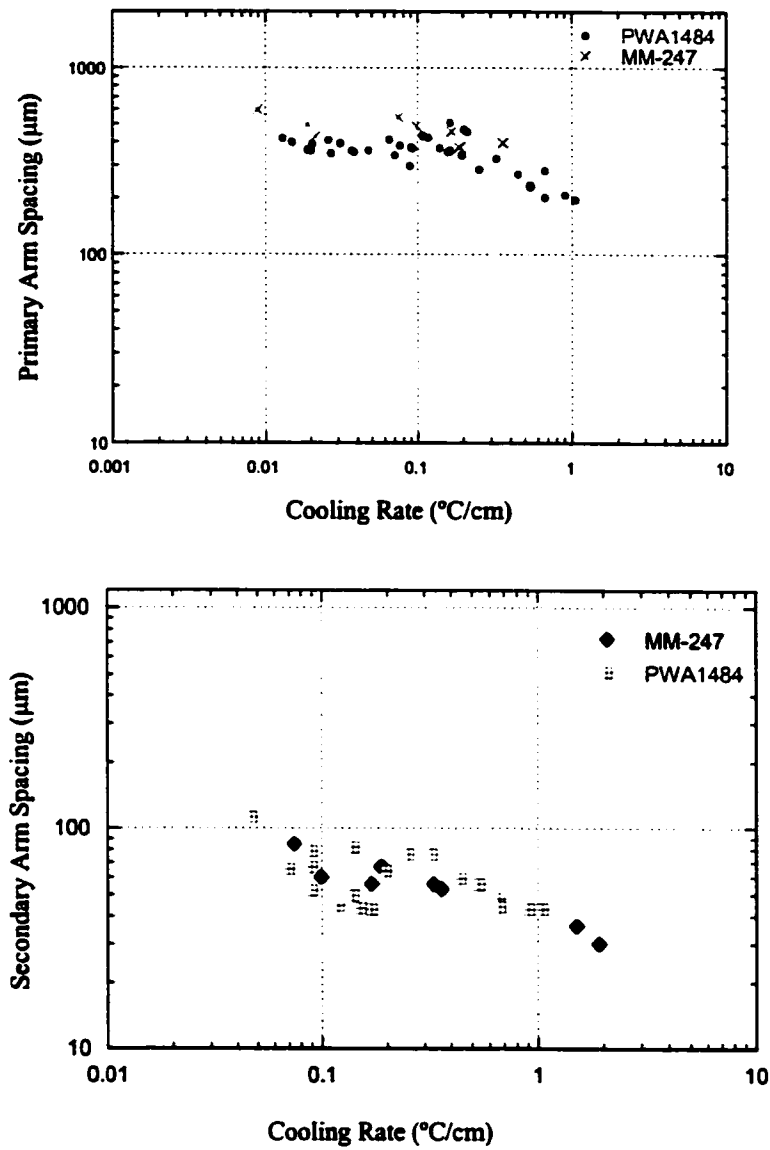
Figure 5-32. Primary arm spacings of DS MM247 and PWA1484 correlated with cooling

rate GV (°C/s) [103]

The secondary phases found in as-cast MM247 samples include eutectic ($\gamma'+\gamma$) pools, divorced eutectic γ' and metal carbides MC. It is observed that, for the sample grown at 0.005 cm/s, there are plenty of small size eutectic ($\gamma'+\gamma$) pools and script metal carbides MC, while for the sample grown at 0.0005 cm/s, there are plenty of divorced eutectic γ' and block shape carbides MC.

The compositions at different regions and precipitates were analyzed using the same procedures as that for DS PWA 1484 samples. The phase compositions and partitioning results are similar to PWA1484 and are listed in Table 5-5.

(5.2.2.5) Furnace Design Effects

Table 5-6 gives the numbers of samples with freckle chain defects and the conditions under which the samples were grown. These results show that freckle defects are formed only in the samples of alloy MM247 and that most of the samples with freckle defects were grown in the cylindrical furnace. Compared with the box furnace, the cylindrical furnace has the adiabatic zone with the thickness of 5 cm, while the box furnace adiabatic zone has a thickness of 13 cm. This difference resulted in the displacement of mushy zone out of the adiabatic zone.

Figure 5-33 shows the positions of the mushy zone in the adiabatic zone for the two furnaces and also speculates on the qualitative geometry of the growing interfaces of DS samples. The figure shows that the mushy zone shifts down when the growth velocity and/or the temperatures of furnace are increased. It also shows the mushy zone of DS samples grown in the box furnace are located in the upper section of the adiabatic zone

Table 5-5 Composition distribution at data on an as-cast DS MM247 sample grown at

V=0.0005 cm/s and G=35°C/cm

	Al	Ti	Cr	Fe	Co	Mo	Hf	Ta	W	Ni
nominal	5.50	1.00	8.30	0.00	10.00	0.70	1.50	3.00	10.00	60.00
average	5.05	1.02	9.42	0.13	8.80	0.97	1.63	3.27	13.32	56.38
dendrites	4.86	0.61	8.26	0.10	9.49	0.77	1.05	1.80	15.10	57.93
inter-dend.	5.13	1.04	9.96	0.08	8.86	0.84	2.65	3.22	11.37	56.85
MC	0.00	10.57	0.42	0.11	0.00	0.83	14.09	61.39	11.46	1.30
freckle	5.18	0.88	7.89	0.09	8.79	0.78	1.55	3.19	13.16	58.53
Partition k	0.95	0.59	0.83	1.25	1.07	0.92	0.40	0.56	1.33	1.02

Table 5-6. Summary of the number of freckling samples and the corresponding

experimental conditions

	Freckling ratio		Thickness of the insulator's bottom (cm)	Position of mushy zone (cm)	Growth velocity (cm/sec)	Thermal gradient (°C /cm)
	MM247	PWA 1484				
Box furnace	1/5	0/5	13	1.5 ~ 9	0.0005	25~40
Cylindrical furnace	5/8	0/2	5	4.5 ~ 8	0.0005	35
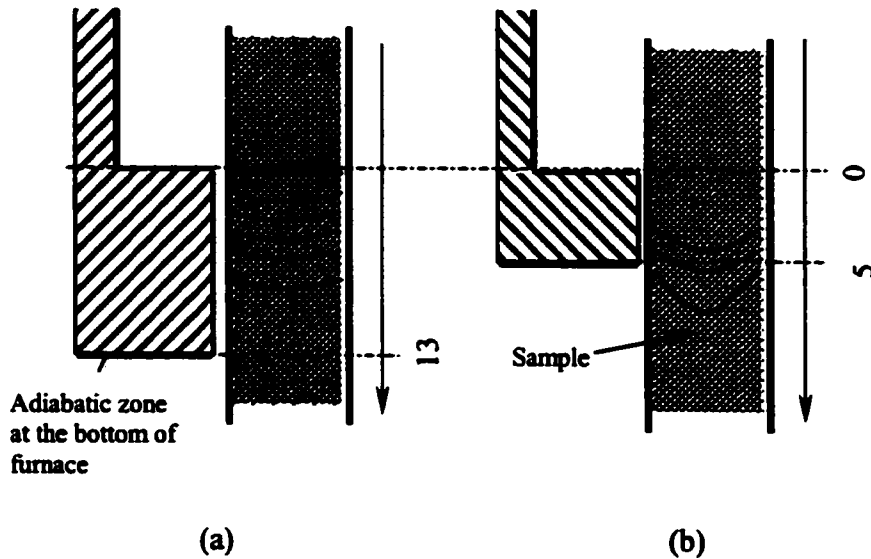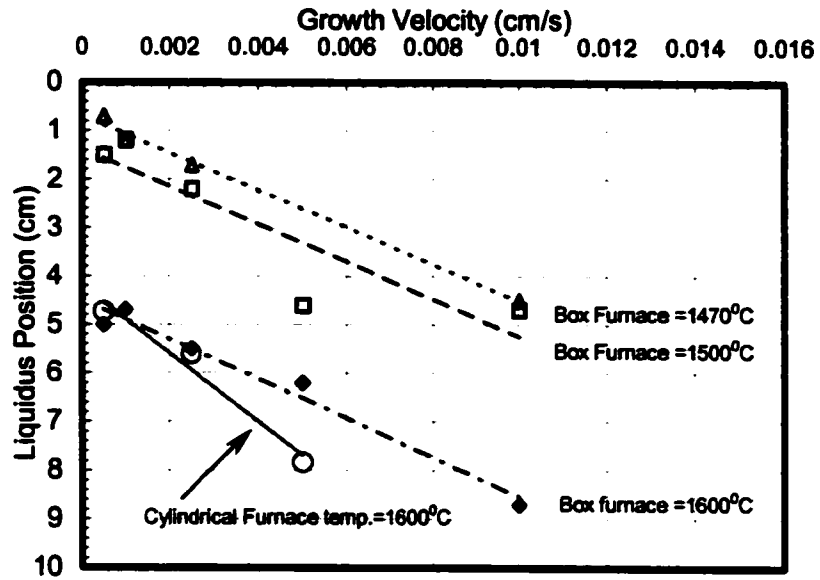
Figure 5-33. The displacement of the mushy zone in/or under adiabatic zone in the DS experiments: Position y=0 indicates the exit position of the chamber of hot zone. Diamond, square, and triangle marks indicate the position of mushy zone in box furnace (a); Circle marks indicate the position of mushy zone in cylindrical furnace (b)

(1.5 ~ 9cm) while the mushy zone of DS samples in the cylindrical furnace are outside

the adiabatic zone. As a result, the samples grown using the cylindrical furnace would be

expected to have larger radial thermal gradients at the growing interface than those grown

in the box furnace. Larger radial thermal gradients could create a convective flow inside

the mushy zone and result in the formation of freckle defects[77,85,90, 91].

5.2.3. Discussion of Freckle Formation Mechanism

(5.2.3.1) Rayleigh Number Calculation for Investigated Alloys

As discussed in the literature review, formation of freckle chains is the result of upward convective flow in the mushy zone. However there are many variables that can influence the convection, segregation, and microstructure development during solidification. Those variables include alloy variables (composition, solute partitioning, stable or unstable density inversion, and thermophysical properties of the liquid alloy) and process variables (thermal gradient, growth velocity, sample size, growth orientation, and spatial thermal distribution). The influences of these variables inter-relate in a very complex manner and the interaction makes it difficult to analyze the effect of each variable individually. Therefore dimensionless parameters that usually include systematic chemical and physical properties, have been suggested to evaluate their combined effects on freckle formation.

The most popular dimensionless parameter for freckle formation tendency is the Rayleigh number in the mushy zone. Rayleigh number represents the ratio of buoyant force to viscous force for the flow, and is often utilized to characterize the onset of fluid flow in unstable systems. The higher R_a, the stronger is the convective flow in the liquid.

Rayleigh number for freckling tendency can be expressed as:

$$R_a = \frac{(\Delta\rho/\rho_0)g\overline{K}h}{\alpha v} \tag{5.3}$$

as proposed by Worster[104] and adopted by Bergman [21], Sung [85], and Beckerman [90,91]. $\Delta\rho$ is the density difference between the interdendritic liquid and the bulk liquid ; ρ_0 is

liquid alloy density at a given temperature; $\bar{K}$ describes the mushy zone permeability; h is the local depth of mushy zone from the tip of cells/dendrites; g is gravitational acceleration; α and v are thermal diffusivity and kinematic viscosity of liquid alloy, respectively.

This equation, which correlates variables including alloy composition, partitioning, mushy zone morphologies, process conditions, and alloy thermophysical properties, is used in this study.

The term of $(\Delta\rho/\rho_0)$ in Equation (5.3) represents the liquid density inversion caused by chemical segregation over the mushy zone and is given by:

$$\frac{\Delta\rho}{\rho_0} = \frac{\rho_0 - \rho_T(h)}{\rho_0} \qquad (5.4)$$

where ρ_0 is the liquid density at the tip of dendrites or cells, or the density of the bulk alloy at the liquidus temperature (i.e., 1400°C for PWA 1484). $\rho_T(h)$ is the liquid density at location below the tip at given distance h, evaluated at the local temperature T and segregated liquid concentration. In order to simplify the calculation, the local liquid density over the mushy zone is assumed to be a linear relationship from liquidus to solidus. The measured compositions at interdendritic or cellular regions from the present DS samples (Table 5-3) are used as the eutectic liquid concentrations at the bottom of mushy zone to calculate density $\rho_{Ts}(H)$, where H indicates the height of the mushy zone. $\rho_T(h)$ is determined by $[\rho_0 - \rho_{Ts}(H)] \ast h/H$.

The liquid density calculations followed the approach proposed by Sung and Poirier[105].

$$\rho = \frac{\sum M_i X_i}{\sum V_i X_i + \Delta V^M} \qquad (5.5)$$

$$V_i = \frac{M_i}{\rho_i^0}[1 + 0.01 \times f(T)]^3 \qquad (5.6)$$

$$f(T) = a_0 + a_1 T + a_2 T^2 + a_3 T^3 \qquad (5.7)$$

where M_i is the atomic weight of element i (g/mol) of the alloy; X_i is the atomic fraction

of element i; V_i (cm^3/mol) is the molar volume of each pure element i; ΔV^M is the

mixing volume and M is the number of elements; ρ_i^0 (g/cm^3) is the density of each

element at 20 ^{0}C; $a_0 \sim a_3$ are thermal expansion coefficients for the elements of the

superalloy; T (K) is the local temperature. The relative values for the refractory elements

can be found in Sung [105]. The X_i of each element are calculated using actual measured

compositions listed in Table (5-3) for PWA 1484 and Table (5-5) for MM247. The

density inversion and local density of PWA 1484 and MM247 calculated are shown in

Table 5-7.

Table 5-7. Calculated density inversion over mushy zone and liquid density at the solidus

and liquidus temperature for PWA 1484 and MM247 alloys

	MM247		PWA 1484	
	T_L=1613K	ρ=7.872 (g/cm^3)	T_L=1673K	ρ=8.409 (g/cm^3)
	T_S=1553K	ρ=7.816 (g/cm^3)	T_S=1603K	ρ=8.385 (g/cm^3)
$(\Delta\rho/\rho_0)^H$ (wt %)	0.0071		0.00285	

The terms $\overline{K}$ and h in the Equation (5.3) describe the morphology at the front of solidification interface. h refers to the depth of mushy zone measured downward from the tip of dendrites or cells. For a given thermal gradient, $h = \dfrac{T_L - T}{G}$, and T_L is liquidus temperature.

As noted above, $\overline{K}$ denotes the mean liquid permeability over the mushy zone, and is evaluated by using the equation:

$$\overline{K} = K_0 \times \frac{(1 - \overline{\varepsilon_s})^3}{\overline{\varepsilon_s}^2} \tag{5.8}$$

where $K_0 = 6 \times 10^{-4} \lambda_1^2$, and λ_1 is the primary arm spacing[21,90,91]. Here actual measured λ_1 from a specific sample is used for calculation of K_0. Also in the equation (5.8) ε_s is the average solid fraction at the mushy zone height h and is given by $\overline{\varepsilon_s} = \dfrac{1}{h} \int_0^h \varepsilon_s dy$ [50,90].

Local solid fraction ε_s is estimated from PWA 1484 solid fraction data (Figure 5-10). Calculated values of ε_s and $\overline{\varepsilon_s}$ over the mushy zone are listed in Table 5-8.

Table 5-8. Solid fraction of PWA 1484 Ni-based superalloy

T_L-T(K)	1	2	3	5	10	13	19	28	40
ε_s	0.05	0.1	0.2	0.4	0.6	0.7	0.8	0.9	0.99
$\overline{\varepsilon_s}$	0.025	0.045	0.086	0.162	0.32	0.397	0.515	0.628	0.73

The remaining terms α and v in the Equation (5.3) represent the thermal

diffusivity and kinematic viscosity of the liquid respectively. An approximate value of

$\alpha v = 5 \times 10^{-12} m^4 / s^2$ is used throughout this study in evaluating the Rayleigh

number[85,91,92]. g is gravitational acceleration and equals 9.81 m/s^2.

After the determination of all the factors in Equation (5.3), Rayleigh numbers

were calculated for several directional solidification samples. The detailed processing

parameters for these samples are listed in Table 5-9

Table 5-9. Directional solidification parameters and results for PWA 1484 and

MM247 employed for theoretical estimation of Rayleigh numbers

		G (K/m)	V (cm/s)	ΔT_0 (K)	λ_l (μm)	$(\Delta\rho/\rho_0)^H$	$g/\alpha v$ (m^2/s)	Freckle
PWA 1484	Sample #1	2800	0.005	70	355	0.0029	1.962×10^{12}	No
	Sample #2	3500	0.0025	70	376	0.0029	1.962×10^{12}	No
	Sample #3	3800	0.0005	70	364	0.0029	1.962×10^{12}	No
MM 247	Sample #1	2400	0.005	60	470	0.0071	1.962×10^{12}	No
	Sample #2	3200	0.0025	60	500	0.0071	1.962×10^{12}	No
	Sample #3	3500	0.0005	60	495	0.0071	1.962×10^{12}	Yes

In terms of equations (5.3) ~ (5.8), and the variables are provided from Table 5-6 ~ Table 5-8, Rayleigh number can be calculated as follows:

$$R_a = \frac{(\Delta\rho/\rho_0)^k g\overline{K}h}{\alpha\upsilon}$$

$$= (\frac{\Delta\rho}{\rho_0})^H \times \frac{h}{H} \times (\frac{g}{\upsilon\alpha}) \times \frac{K_0(1-\overline{\varepsilon_s})^3}{\overline{\varepsilon_s}^2} \times h$$

$$= (\frac{\Delta\rho}{\rho_0})^H \times (\frac{g}{\alpha\upsilon}) \times 6\times10^{-4} \times \lambda_1^2 \times \frac{(1-\overline{\varepsilon_s})^3}{\overline{\varepsilon_s}^2} \times \frac{h^2}{H} \tag{5.9}$$

$$= 6\times10^{-4} \times (\frac{\Delta\rho}{\rho_0})^H \times (\frac{g}{\alpha\upsilon}) \times \frac{(1-\overline{\varepsilon_s})^3}{\overline{\varepsilon_s}^2} \times \lambda_1^2 \times \frac{(\Delta T/G)^2}{(\Delta T_0/G)}$$

$$= 6\times10^{-4} \times (\frac{\Delta\rho}{\rho_0})^H \times (\frac{g}{\alpha\upsilon}) \times \frac{(1-\overline{\varepsilon_s})^3}{\overline{\varepsilon_s}^2} \times \frac{1}{\Delta T_0} \times \frac{1}{G} \times \lambda_1^2 \times \Delta T$$

Figure 5-34 illustrates the variation of Rayleigh number with solid fraction through the mushy zone for selected DS PWA 1484 and MM 247 alloys. Under similar solidification parameters (i.e., thermal gradient and growth velocity), the estimated values of Rayleigh number of DS MM247 are larger than those of DS PWA 1484. Hence the growth front of PWA 1484 is predicted to be more stable than that of MM 247. This is consistent with the experimental observation that freckle chains are seen only on the surfaces of some of MM 247 samples but none on any PWA 1484 samples. Rayleigh number increases with solid fraction, reaches a maximum at around 10% solid fraction, and then decreases with increasing solid fraction. This can be explained since the Rayleigh number is proportional to both permeability and density inversion over mushy zone. The permeability decreases with increasing solid fraction (i.e., deeper to the mushy zone) while the density inversion increases with solid fraction.
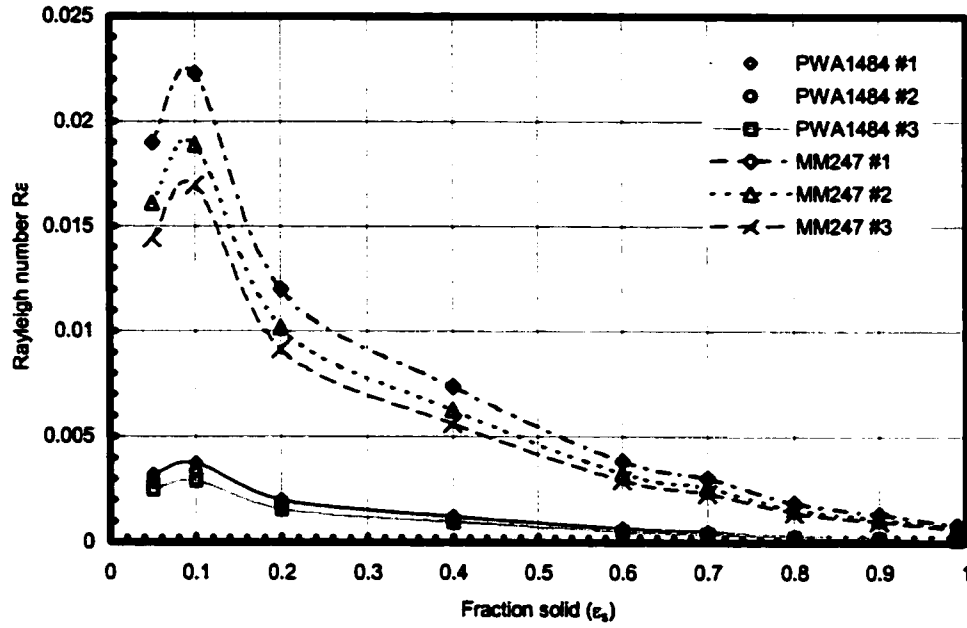
Figure 5-34. Illustration of calculated Rayleigh number with solid fraction in mushy zone

for DS MM247 and PWA 1484 under various conditions

Further research is required to better understand the permeability and density

inversion over the mushy zone in order to confidently calculate Rayleigh numbers. For

example, Hellawell [20] and Tewari [24] reported critical Ra in the range of 0.063~0.07 for

the onset of thermal-solute convection in the DS Pb-Sn alloys, while Burgman [21]

reported values around 35~50 for DS Pb-Sn alloys. Beckermann [90] proposed critical Ra

= 0.25 for Ni-based superalloy, while Sung [105] calculated the value to be approximately

25 for a nickel-based superalloy N5.

(5.2.3.2) Effects of Process Variables on the Freckle Formation:

(A) Effects of Alloy Compositions and Partitioning (k)

It is obvious from the equation $R_a = \dfrac{(\Delta \rho / \rho_0)g\overline{K}h}{\alpha v}$ that larger density inversion

$\dfrac{\Delta \rho}{\rho_0}$ of the segregated solute-rich liquid results in larger system Rayleigh number, and

increases the probability of forming convective flow and freckle chains.

The density inversion is determined by alloy composition and the segregation of

alloying element during solidification. Such chemical segregation can cause the local

liquid density to decrease if light elements are preferentially rejected out from (i.e. for a

partition coefficient less than unity) or if heavy elements are preferentially incorporated

into the solid (i.e., for a partition coefficient greater than unity). In simple Pb-Sn binary

alloys and NH_4CL-H_2O, the density inversions are significant, therefore freckle chains

are readily formed[18-21, 24].

The multi-component superalloys are more complex since every element has its own partition coefficient. Both light elements and heavy elements can segregate to the liquid. The density inversion is the sum of the results of all the individual element segregations. For alloy MM247, chemical analysis shows the heavy element tungsten segregates to the solid. This leads to the density inversion ahead of the growth interface. In PWA 1484, heavy elements rhenium and tungsten segregate to dendritic / cellular trunks too. However, tantalum segregated to the liquid and compensated for the density loss caused by the depletion of W and Re. Therefore the density inversion ahead of the interface is minimized. Addition of Ta in PWA 1484 creates a stable growth condition and minimizes the probability of forming freckles as well as strengthens the alloy by increasing the volume percentage of γ' precipitates.

In addition, chemical reactions during solidification can also influence the density inversion. There are more carbides formed in MM247 than in PWA 1484. The formation of carbides can consume more of the heavier elements i.e., Hf and W, and decrease the liquid density. This could increase the density inversion of MM247 and promote the convective flow and freckle formation.

(B) Effects of Process Conditions (G, V)

The process conditions (G, V) directly affect the morphology and permeability of the mushy zone. The morphologies can be characterized with primary arm spacing λ_1, secondary arm spacing λ_2, mushy zone height (h), and dendritic or cellular trunks contour shapes which are related to the solid-fractions. Generally, large arm spacings λ_1 lead to

high permeability and allow convective flows to penetrate readily into the mushy zone, and assist the formation of channels and freckles.

As shown by the freckle phenomena among the MM247 samples, freckle chains only exist on the surface of the sample grown at 0.0005 cm/s. Compared with the samples grown at the higher velocities of 0.005 and 0.0025 cm/s, the 0.0005cm/s sample had larger arm spacings (~500μm) and flanged cellular trunks which are presumably less resistive to the convective flow through the array of trunks (refer to Figure 5-30).

Pollock[30] investigated the breakdown of single crystal solidification in high refractory nickel-based superalloy and found that the freckle chains occurred only when the primary arm spacing exceeded a critical value, i.e., 320μm. Tewari[29] studied the influence of primary arm spacing and mushy zone length on the macrosegregation during directional solidification of Pb-Sn binary alloys and found that the extent of macrosegregation increased with increasing primary arm spacings and the freckles were suppressed when primary arm spacings were small. Sarazin[20] also noted that an increase of thermal gradient and growth velocity decreases the primary spacing and reduces the tendency for freckle formation.

(C) Effects of Non-Axial Thermal Gradients

Freckle chains have not been observed on any DS PWA 1484 sample in the present investigation, where the thermal distribution during solidification is axisymmetric and the growth interface is stable. The axial thermal symmetry is evidenced by microstructure development, i.e. axial symmetric arm spacings distribution and well-

aligned dendrites or cells. This type of thermal symmetry can suppress potential

perturbations and convective flow ahead of the growing interface. In this study, transients

in crucible shaking, start/stop withdrawal, and section size changes all failed to perturb

the stable situation in PWA 1484 DS. Therefore the solute-rich liquid at the front of the

growing interface did not form upward plumes or channels and no freckles were

produced.

When the heat flux across the growing interface is non-symmetric, the situation

can be different. Auburtin et al[76,77] reported a study on freckle formation and freckle

criteria in superalloys. These researchers demonstrated when the inclination angle

between the growth front interface and gravity is not zero, the tilted DS samples

exhibited freckles in contrast to the vertical samples which did not have freckles.

Beckermann et al[90] stated that even a small inclination (less than 10°) could

significantly lower the critical Rayleigh number and induce freckle chain formation.

In a report by Overfelt et al[14], freckle chains were observed on the surface of an

elliptical PWA 1484 sample. Figure 5-35 illustrates that the freckle chains extend from

middle height to top, and contained small equiaxed grains and porosity. The freckle

chains are about 1mm wide. In this investigation, the directional solidification of PWA

1484 alloy was conducted in Howmet Corporation's commercial directional casting

facility in Whitehall, ML. (Figure 1-3). One cluster of 6 vertical circular and elliptical

cylinder samples was arranged as shown in Figure 5-36 with the important dimensions
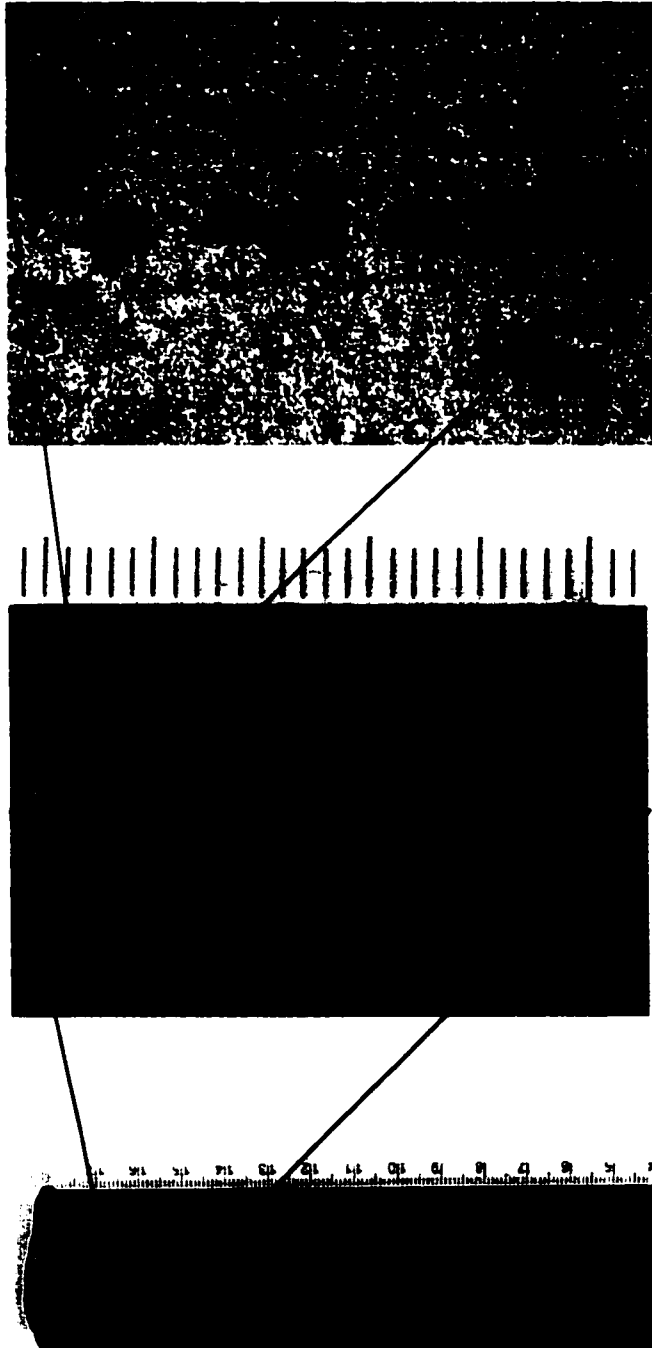
marked.

Figure 5-35. Illustration of freckle chains observed on the surface of DS PWA 1484 elliptic cylindrical sample[14]
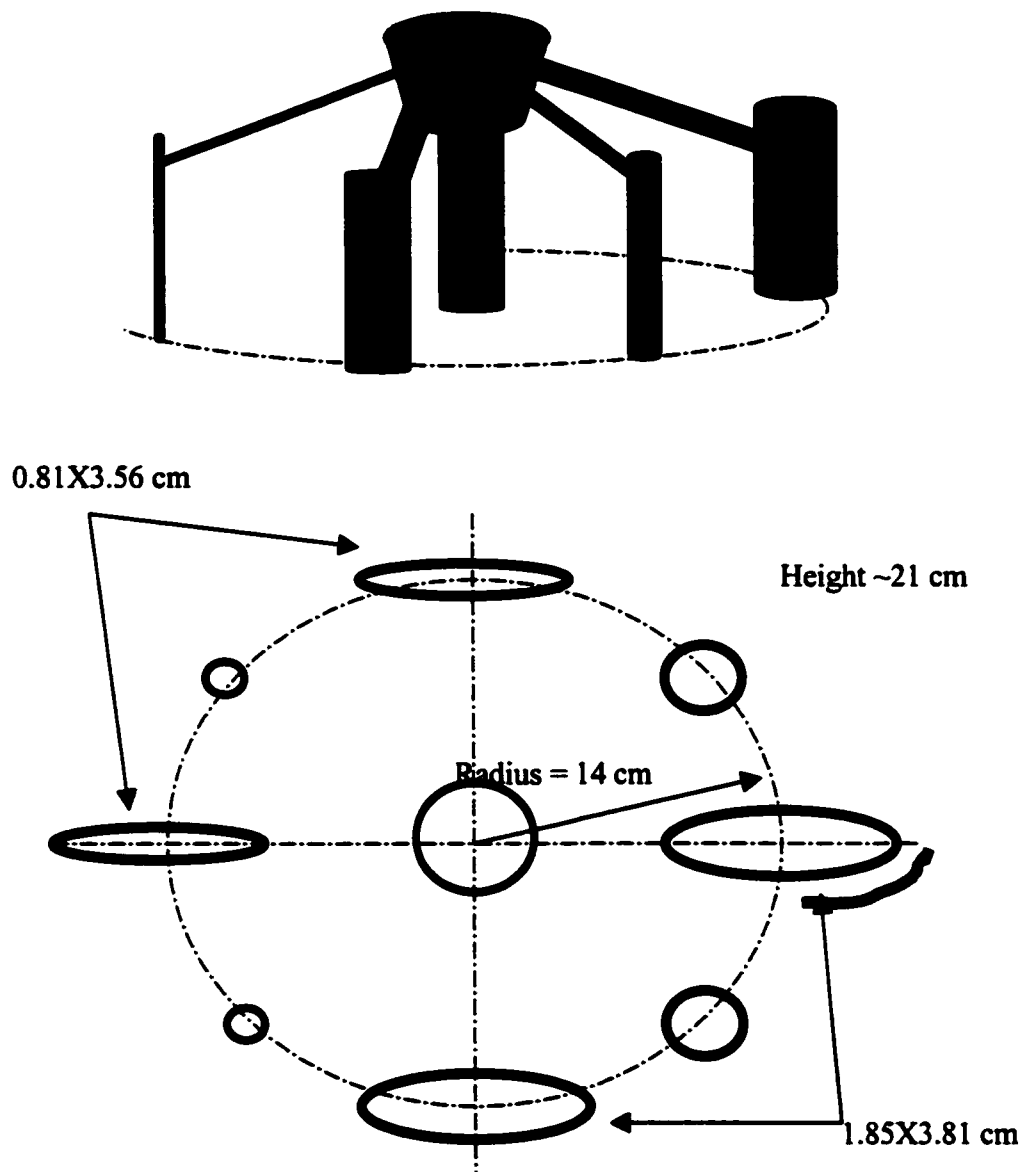
Figure 5-36. Illustration of an investment cast cluster of samples.

The casting result shows that only the largest elliptical sample with the major axis radially orientated exhibited freckle chains on the surface. The chains were on the surface toward the outside of the cluster. All the samples in the cluster were located along a perimeter line and hence there was no axial thermal symmetry in any sample. The lack of axial thermal symmetry in the largest elliptical cylinder is believed to be especially significant. It is well known that the natural convective flow direction in the liquid is downward in the low temperature region and upward in the high temperature region. This creates lateral convective flow from cold to hot regions at the bottom of the bulk liquid and presumably was primarily responsible for the freckles in the sample.

CHAPTER 6.

CONCLUSIONS

(1) The experimental data for PWA1484 exhibits excellent agreement with the well-known exponential equation ($\lambda_1 \propto G^{-1/2} V^{-1/4}$). However, the constant of proportionality is different depending upon whether the solidification microstructure contains secondary arms or not. The presence of secondary arms increases the spacing between dendrites and leads to a greater sensitivity of λ_1 on $G^{-1/2} V^{-1/4}$, while the primary spacings are much less sensitive to changes in the solidification parameter $G^{-1/2} V^{-1/4}$ when the secondary arms are not preserved.

(2) The primary dendritic arm spacing results were compared to recent theoretical models. The models of Hunt and Lu[42,43] provided excellent agreement at medium to high thermal gradients and a wide range of solidification velocities. The exponent of V was shown to vary with the imposed thermal gradient in the experimental results. At high thermal gradient (88~ 108 °C/cm), the exponent was measured as –0.19, approaching the theoretical value of –0.25. Off-axis heat flows were shown to cause radial non-uniformity in the dendrite arm spacing data for low thermal gradients and large withdrawal velocities.

(3) γ' precipitates initiate as small spheroids, and the morphologies develop to cubed, and then irregular. At high growth velocity, small scale $\gamma'+\gamma$ eutectics are

preferentially formed, while large scale divorced eutectics dominate when the growth velocity is quite low.

(4) Carbide morphologies are largely dependent on the process conditions: script carbides formed at high growth velocity, plate-like carbides formed at low growth velocity, and blocky carbides formed at near-planar interface conditions.

(5) The compositions of PWA1484 lead to less density inversion and perturbation probability ahead of the growth interface than that of the MM247 alloy, therefore PWA 1484 alloy has the better anti-freckling ability than MM247 alloy.

(6) In order to successfully implement Rayleigh number Ra as a critical parameter to estimate freckle formation potential, more precise expression of permeability at mushy zone needs to be developed, and more precise measurement of solute concentration over mushy zone is required.

REFERENCES

1. E. F. Bradley: " Superalloys: A Technical Guide". Metals Park, OH : ASM International, c1988

2. E. F. Bradley: Source Book on Materials for Elevated- Temperature Applications, American Society for Metals, Metals Park, Ohio 44073, 1969, pp. 275-298.

3. G. P. Sabol, R.Stickler: "Microstructure of Nickel –based Superalloys: Review Article" phys. Stat. Sol.35. 11 (1969) Westinghouse Research Laboratories, Pittsburgh, Pennsylvania

4. P. S. Kotval: Metallography, 1969, Vol. 1, pp. 251-285.

5. Madeleine Durand-Charre: "The Microstructure of Superalloys", Gordon and Breach Science Publishers, 1997, (ISBN 90-5699-097-7).

6. A. K. Jena, M.C. Chaturvedi: Journal of Materials Science, 1984, Vol. 19, pp. 3121-3139.

7. C. T. Sims: Journal of Metals, 1966, October, pp. 1119-1130.

8. Michael F. Ashby and David R.H. Jones: Engineering materials 1 : an introduction to their properties and applications. Oxford ; Boston : Butterworth-Heinemann, c1996. Materials and Engineering Textbook.

9. M. Ott, H. Mughrabi: Mater. Sci. & Eng., 1999, Vol. A272, pp24-30

10. Koji Kakehi: Materials Science and Engineering, 2000, Vol. A278, pp. 135-141.

11. M. P. Jackson, R. C. Reed: Materials Science and Engineering, 1999, Vol. A259, pp. 85-97.

12. W. H. Jiang, H. R. Guan, Z. Q. Hu: Materials Science and Engineering, 1999, Vol. A271, pp. 101-108.

13. John K.Tien, Thomas Caulfield: Superalloys, Supercomposites and Superceramics". Boston: Academic Press, c1989

14. R. A. (Tony) Overfelt, Craig Matlock, and V. Sahai "Microstructure and Grain Defect Formation in Directionally Solidified PWA1484" research report to Howmet Corp. Dec. 1995.

15. M. T. Jovanovic, Z. Miskovic, and B. Lukic: Materials Characterization, 1998, Vol. 40, pp. 261-268.

16. J. K. Tien and R. P. Gamble: Mater. Sci. Eng., 1971, Vol. 8, pp. 152-160.

17. A. F. Giamei, B.H. Kear: Metall. Trans., 1970, Vol. 1, pp 2185-2192.

18. S. M. Copley, A. F. Giamei, S.M. Johnson and M.F. Hornbecker: Metall. Trans. 1970, Vol. 1, pp. 2193-2204.

19. A. K. Sample, A.Hellawell: Metall. Trans. 1984, Vol. 15A, pp. 2163—2173.

20. J. R. Sarazin, A. Hellawell: Metall. Trans., 1988, Vol. 19A, pp. 1861—1871.

21. M. I. Bergman, D. R. Fearn, J.Bloxham, and M. C. Shannon: Metall. Trans. 1997, Vol. 28A, pp859—866.

22. M. I. Bergman, D. R. Fearn, J.Bloxham: Metall. Trans. 1999, Vol. 30A, pp. 1809-1815.

23. N. Streat and F. Weinberg: Metall. Trans., 1974, Vol. 5, pp. 2539—2548.

24. S. N. Tewari, R. Shah: Metall. Trans., 1992, Vol. 23A, pp. 3383—3392.

25. D. Hirvo, T. Hansen, B. A. Mueller: "Investment Casting Applications of Process Modeling" presentation at 1999 TMS Fall Meeting.

26. W. A. Tiller, K. A. Jackson, J. W. Rutter, and B. Chalmers: Acta Metall. 1953, Vol. 1, pp. 428-437.

27. W. Kurz and D.J. Fisher: Fundamentals of Solidification" Trans Tech Publications, Aedermannsdorf, Switzerland, 1992, pp80—89.

28. H. K. Kim, J.C. Earthman and E.J. Lavernia: Acta Metall. mater. Vol. 40(4), pp. 637-647.

29. S. N. Tewari and R. Shah: *Metall. Mater. Trans.*, 1996, Vol. 27A, pp. 1353-1362

30. T. M. Pollock and W.H. Murphy: *Metall. Mater. Trans.*, 1996, Vol. 27A, pp. 1081-1094

31. S. H. Han and R.Trivedi: *Acta metall. Mater.*, 1994, Vol. 42, pp. 25-41.

32. M. Vijayakumar and S.N. Tewari, James E. Lee, P.A. Curreri: Materials Science and Engineering, 1991, Vol. A132, pp. 195-201.

33. M. A. Chopra and S.N. Tewari: *Metall. Trans.*, 1991, Vol. 22A, pp. 2467-2473.

34. D. Bouchard and J.S. Kirkaldy: *Metall. Mater. Trans.*, 1996, Vol. 27B, pp. 101-113.

35. K. Somboonsuk, J.T. Mason and R.Trivedi: *Metall. Trans.*, 1984, Vol. 15A, pp. 967-975.

36. R. Trivedi: *Metall. Trans.*, 1984, Vol. 15A, pp. 977-982.

37. M. C. Flemings, D.R.Poirer, R.V. Barone, and H.D. Brody: J. Iron Steel Inst., 1970, pp208-371.

38. P. K. Rohatgi, Jr. C.M. Adams: Trans. Met. Soc. AIME, 1967, Vol. 239:1729

39. P. K. Rohatgi, Jr. C.M. Adams: Trans. Met. Soc. AIME, 1967, Vol. 239:1737

40. J. D Hunt: *Solidification and Casting of Metals*, The Metals Society, London, 1979, pp. 3-9.

41. W. Kurz and D.J.Fisher: *Acta Metallurgica*, 1981 Vol. 29, pp. 11-20.

42. J. D. Hunt, S-Z. Lu: Metall. Mater. Trans., 1996, Vol. 27A, pp. 611-623

43. Shu-Zu. Lu and J.D. Hunt: *J. Crystal Growth*, 1992, Vol. 123, pp.17-34.

44. Dexin Ma and Peter R. Sahm: *Metall. Mater. Trans.*, 1998, Vol. 29A, pp. 1113-1119.

45. Dexin Ma, P. R. Sahm: Giessereiforschung, 1992, Vol. 44(2), pp. 80-85.

46. D. Bouchard and J.S. Kirkaldy: *Metall. Mater. Trans.*, 1997, Vol. 28B, pp. 651-663

47.   R. J. Su, Ruel. A. Overfelt and W.A. Jemian: *Metall. Mater. Trans*, 1998, Vol. 29A, pp. 2375-2381

48.   R. J. Su, W.A. Jemian and Ruel. A. Overfelt: *J. Crystal Growth*, 1997, Vol. 179, pp. 625 -634.

49.   R. N. Grugel and Y.Zhou: *Metall. Trans.*, 1989, Vol.20A, pp. 969-973.

50.   R. Nasser-Rafi, R. Deshmukh, and D.R. Poirier: *Metall. Trans.*, 1985, Vol. 16A, pp. 2263-2271.

51.   D. R. Poirier: *Metall. Trans.*, 1987, Vol. 18B, pp. 245-255.

52.   M. C. Flemings: *Solidification Processing*, McGraw-Hill Inc., New York, 1974, pp. 66-77

53.   C. J. Paradies, R. N. Smith, and M.E. Glicksman: Metall. Mater. Trans. 1997, Vol. 28A, pp. 875-883.

54.   T. Grosdidier, A. Hazotte, A. Simon: Materials Science and Engineering, 1998, Vol. A256, pp. 183-196.

55.   S. J. Yeom, D. Y. Yoon, and M. F. Henry: *Metall. Trans.*, 1993, Vol. 24A, pp. 1976-1981.

56.   Y. Y. Qiu: J. Alloys and Compounds 1996, Vol. 232, pp 254-263.

57.   David Ulrich Furrer: Scripta Materialia, 1999, Vol. 40(11), pp. 1215-1220.

58.   Du Wei, Li Jianguo, Fu Hengzhi: Trans. Nonfeerous Met. Soc. China), 1998, Vol. 8(1), pp. 83-87

59.   Zhang Jun, Liu Yanhong, Li Jianguo, Fu Hengzhi: 0022-2461, 1999 Kluwer Academic Publishers, pp. 2507-2511.

60.   N. Yukawa, Y. Murata and T. Noda: Superalloy 1984, editors, pp. 83-92.

61.   Xuebing Huang, Yun Zhang, Zhuanqi Hu, Honghua Deng and Yulin Liu: Materials Transaction, JIM, Vol. 38(11), 1997, pp. 1016-1021.

62.   V. A. Wills and D. G. McCartney: Materials Science and Engineering, 1991, Vol. A145, pp. 223-232.

63. A. K. Bhambri, T.Z. Kattamis, J.E. Morral: Metall. Trans. 1975, Vol. 6B, pp523-537

64. Shuangjie Chu, Jianguo Li, Zhongyuan Liu, Zhengxing Shi, Hengzhi Fu: *Metall. Mater. Trans.*, 1994, Vol. 25A, pp. 637-642

65. D. Mukherji, H. Gabrisch, W. Chen, H. J. Fecht, & R. P. Wahi: Acta, mater., 1997, Vol. 45. no. 8, pp 3143-3154.

66. Ercan Balikci, R.A. Mirshams, A. Raman: Mater. Sci. & Eng., 1999, Vol. A265, pp50-62

67. C. A. Klepser: Scripta Metallurgica et Materialia, 1995, Vol. 33(4), pp. 589-596.

68. S. C. Fegan, T. Z. Kattamis, J. E. Morral, A. K. Bhambri: J. of Materials Science (letters), 1975, Vol.10, pp. 1266-1270.

69. J. Chen, J.H. Lee, Y.S. Yoo, S.J.Choe, Y.T. Lee: Materials Science and Engineering, 1998, Vol. A247, pp.113-125.

70. R. Fernardez, J. C. Lecomte, T. Z. Kattamis: *Metall. Trans*, 1978, Vol. 9A, pp. 1381-1386.

71. M. J. Starink, H. Cama and R. C. Thomson: Scropta Materialia, 1998, Vol. 38(1), pp. 73-80.

72. J. M. Dahl, W. F. Danesi, R. G. Dunn: *Metall. Trans.*, 1973, Vol.4, pp. 1087-1096.

73. J. Chen, J.H. Lee, Y.S. Yoo, S.J.Choe, Y.T. Lee, B.Y.Huang: High Temperature Materials and Processes (UK), 1999, Vol. 18(3), pp. 109-123.

74. W. R. Sun, J. H. Lee, S. M. Seo, S. J. Choe, Z. Q. Hu: Materials Science and Engineering, 1999, Vol. A272, pp. 143-149.

75. S. N. Tewari, R. Shah, M. A. Chopra: Metall. Trans. 1993, Vol. 24A, pp. 1661-1669.

76. P. Auburtin, S.L. Cockcroft, A. Witchell "Liquid Dendity Inversion during Solidification of Superalloy and their Relationship to Freckle Formation in Castings" Superalloys 1996, TMS, 1996 R.D. Kissinger, D.J. Deye, D.L. Anton, eds., pp. 443-450.

77. P. Auburtin, T. Wang, S.L. Cockcroft, and A. Mitchell: *Metall. Mater. Trans*, 2000, Vol. 31B, pp. 801-811

78. T. M. Pollock, W. H. Murphy, E. H. Goldman, D. L. Uram and J. S. Tu: Superalloys 1992, editors: S.D. Antolovich, R. W. Stusrud, R. A. MacKay, D. L. Anton, T. Khan, R. D. Kissinger, D. L. Klarstrom, TMS, 1992, pp. 125-134.

79. Van Den Avyle, James A., Brooks, John A., Powell, Adam C.: JOM, 1998, Vol. 50(3), pp. 22-25.

80. H. Shahani, G. Amberg, & H. Fredriksson: Metall. Trans. 1992, Vol. 23A, pp2301~2311.

81. J. C. Heinrich, S. Felicelli, P. Nandapurkar, D.R. Poirier: Metall. Trans. 1989, Vol. 20B. pp. 883—891

82. S. D. Felicelli, D.R.Poirier, J.C. Heinrich: J. of Crystal Growth, 1998, Vol. 191, pp. 879-888.

83. S. D. Felicelli, D.R.Poirier, J.C. Heinrich: Metall. Trans., 1998, Vol. 29B pp. 847-855.

84. N. Ahmad, H. Combeau, J. L. Desbiolles, T. Jalanti, G. Lesoult, J. Rappaz, M. Rappaz & C. Stomp: Metall. & Mater. Trans., 1998, Vol. 29A, pp617-630.

85. P. K. Sung, D. R. Poirier and S.D. Felicelli: *Metall. Mater. Trans*, 2001, Vol. 32A, pp. 202-207

86. W. D. Bennon, F. P. Incropera: Int. J. Heat Mass Transfer. 1987, Vol. 30(10), pp. 2171-2187.

87. P. J. Prescott, F. P. Incropera: Metall. Trans 1991, Vol. 22B, pp. 529-539.

88. D. R. Poirier, J. C. Heinrich: Modeling of Casting, Welding and Advanced Solidification Processes VI, editors: T. S. Piwonka, V. Voller, and L. Katgerman, The Minerals, Metals and Materials Society, 1993, pp.227-234

89. G. Hansen, A. Hellawell, S. Z. Lu, and R. S. Steube: Metall. Mater. Trans. 1996, Vol. 27A, pp.569-581

90. C. Bckermann, J.P. Gu, and W.J. Boettinger: *Metall. Mater. Trans.*, 2000, Vol. 31A, pp. 2545-2557.

91. M. C. Schneider, J.P. Gu, C. Beckermann, W.J. Boettinger, and U.R. Kattner: *Metall. Mater. Trans*, 1997, Vol. 28A, pp. 1517-1531

92. W. Kurz and D.J. Fisher: *Fundamentals of Solidification*, Trans Tech publications, Aedermannsdorf, Switzerland, 1992, pp. 65-69.

93. D. G. McCartney and J.D. Hunt: Acta Metallurgica, 1981, Vol. 29, pp. 1851-1863.

94. T. Okamoto, K. Kishitake: J. *Crystal Growth*, 1975, Vol. 29, pp.131-136.

95. T. Okamoto, K. Kishitake: J. *Crystal Growth*, 1975, Vol. 29, pp.137-146.

96. J. Lapin, A. Klimova, R. Velisek and M.Kursa: Scripta Materialia, 1997, Vol. 37, pp85-91.

97. L. Backerud, G.Chai, and J.Tamminen: *Solidification Characteristics of Aluminum Alloys, Vol 1: Wrought Alloys*, AFS/Skanaluminium, Des Plaines, IL 1990, pp. 65-70.

98. Dexin Ma, Peter R. Sahm: Z. Metallkd., 1990, Vol. 82, pp. 869-873.

99. P. N. Quested, M.McLean: Materials Science and Engineering, 1984, Vol. 65, pp. 171-180.

100. H. Jamgotchian, B.Billia, and L. Capella: *J. Crystal Growth*, 1983, Vol. 64, pp. 338-344.

101. M. B. Eshelman, V. Seetharaman and R. Trivedi: Acta Metall. Mater. 1988, Vol. 36, pp. 1165-1174.

102. M. A. Eshelman, V. Seetharaman, and R. Trivedi: Acta Metall., 1988, Vol. 36(4), pp. 1175-1185.

103. H. S. Whitesell, L. Li, and R.A. Overfelt: Metall. Mater. Trans. 2000, Vol. 31B, pp. 546-552

104. M. Grace Worster: J. Fluid Mech., 1992, Vol. 237, pp649-669.

105. P. K. Sung, D. R. Poirier, E. McBride: Materials Science and Engineering, 1997, Vol. A231, pp. 189-197.
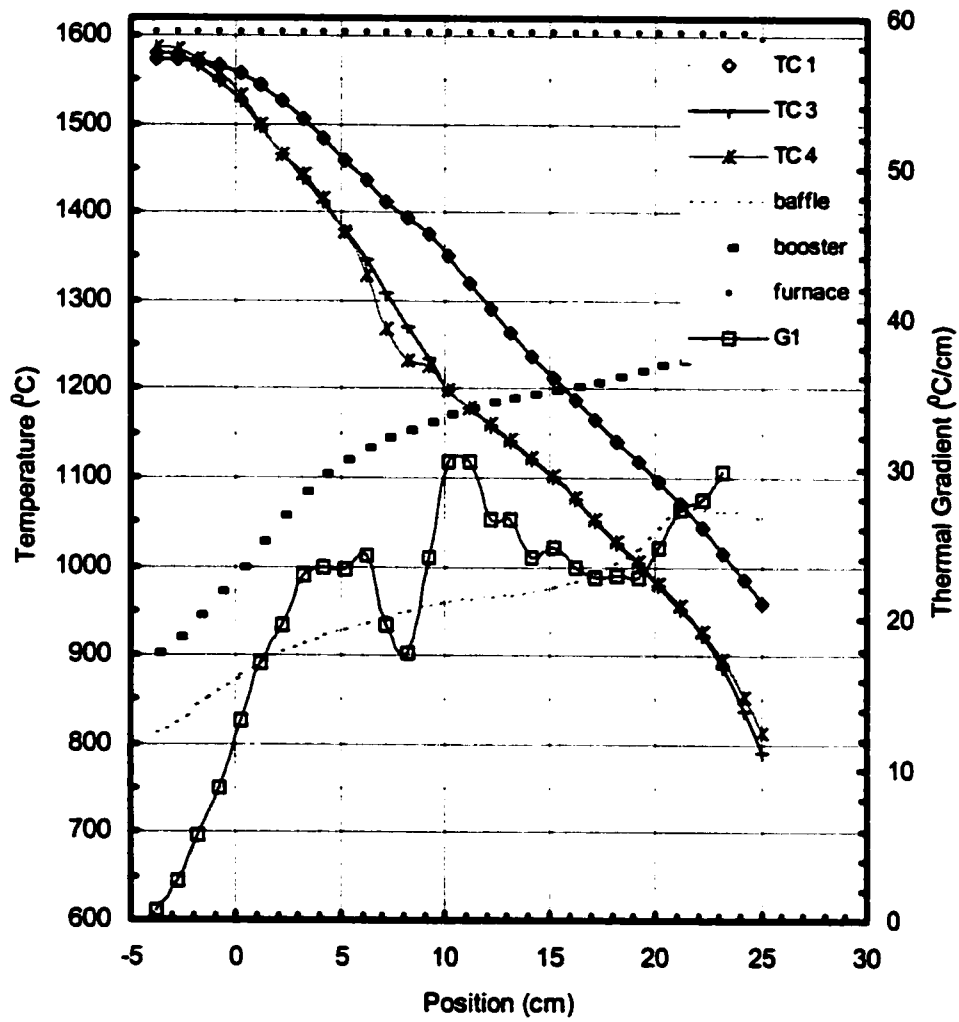
Figure A-1: V=0.01 cm/s and G=17 °C/cm. Furnace setting temperature = 1600 °C
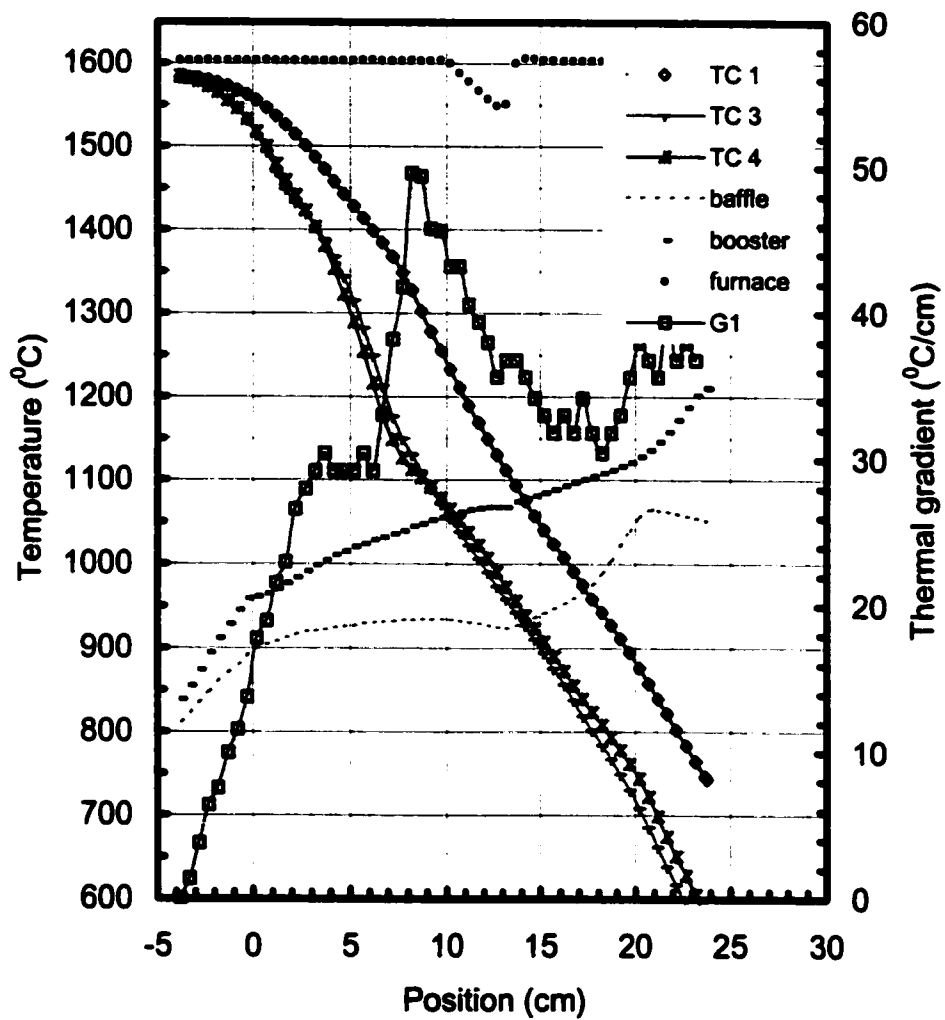
Figure A-2: V=0.005cm/s and G=30 °C/cm. Furnace setting temperature = 1600 °C
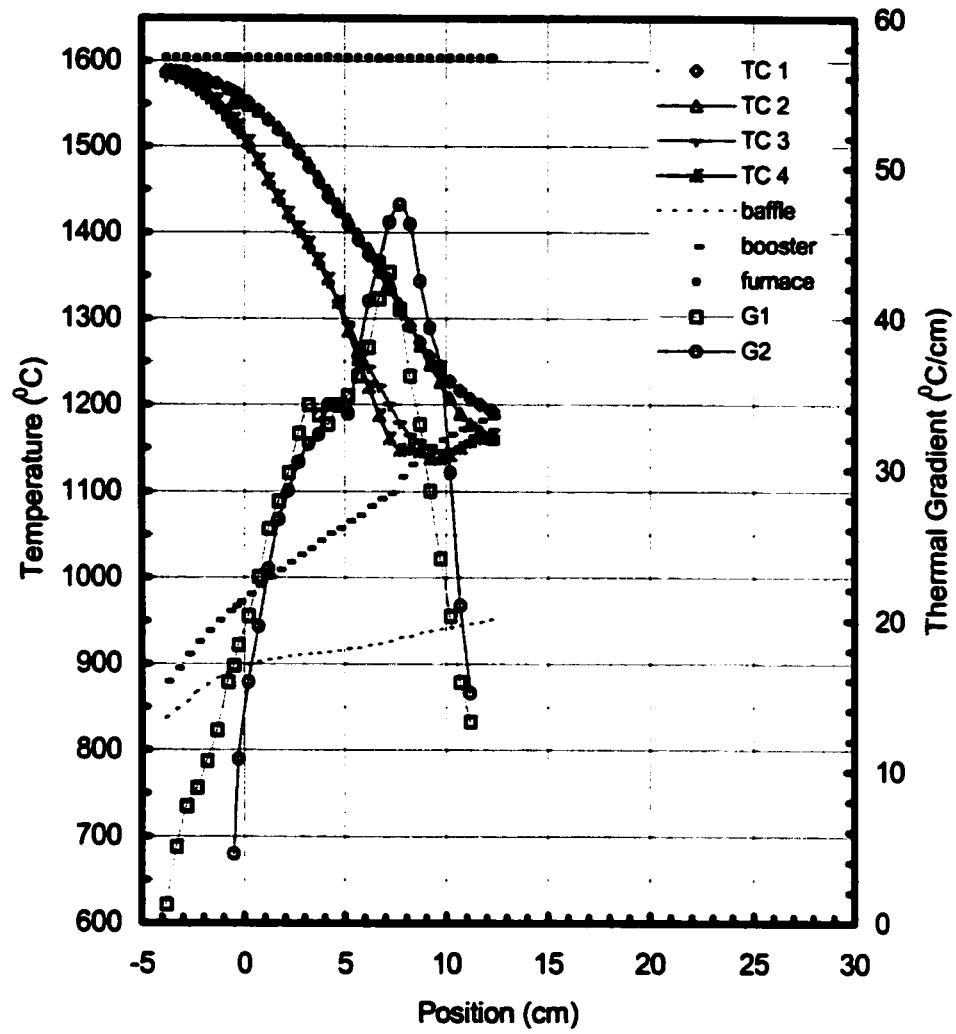
Figure A-3: V=0.0025cm/s and G=35 °C/cm. Furnace setting temperature = 1600 °C
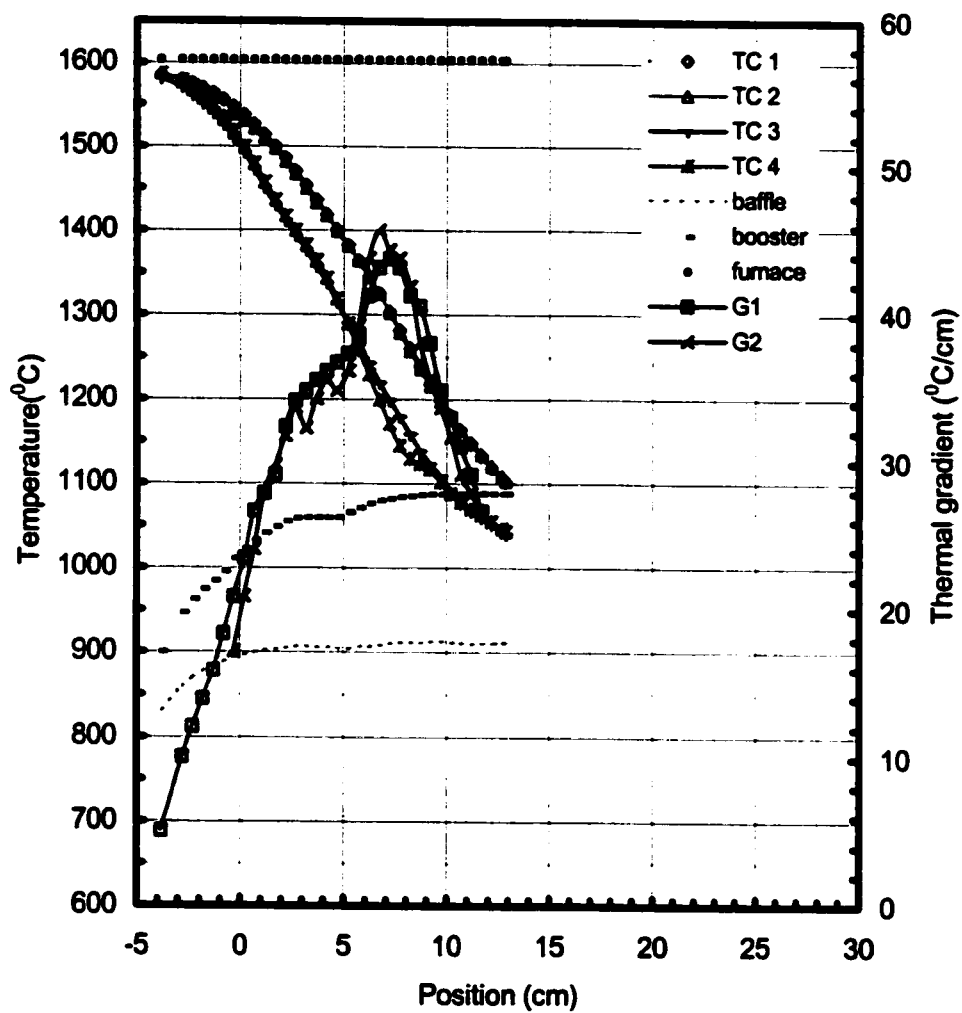
Figure A-4: V=0.001cm/s and G=36 °C/cm. Furnace setting temperature = 1600 °C
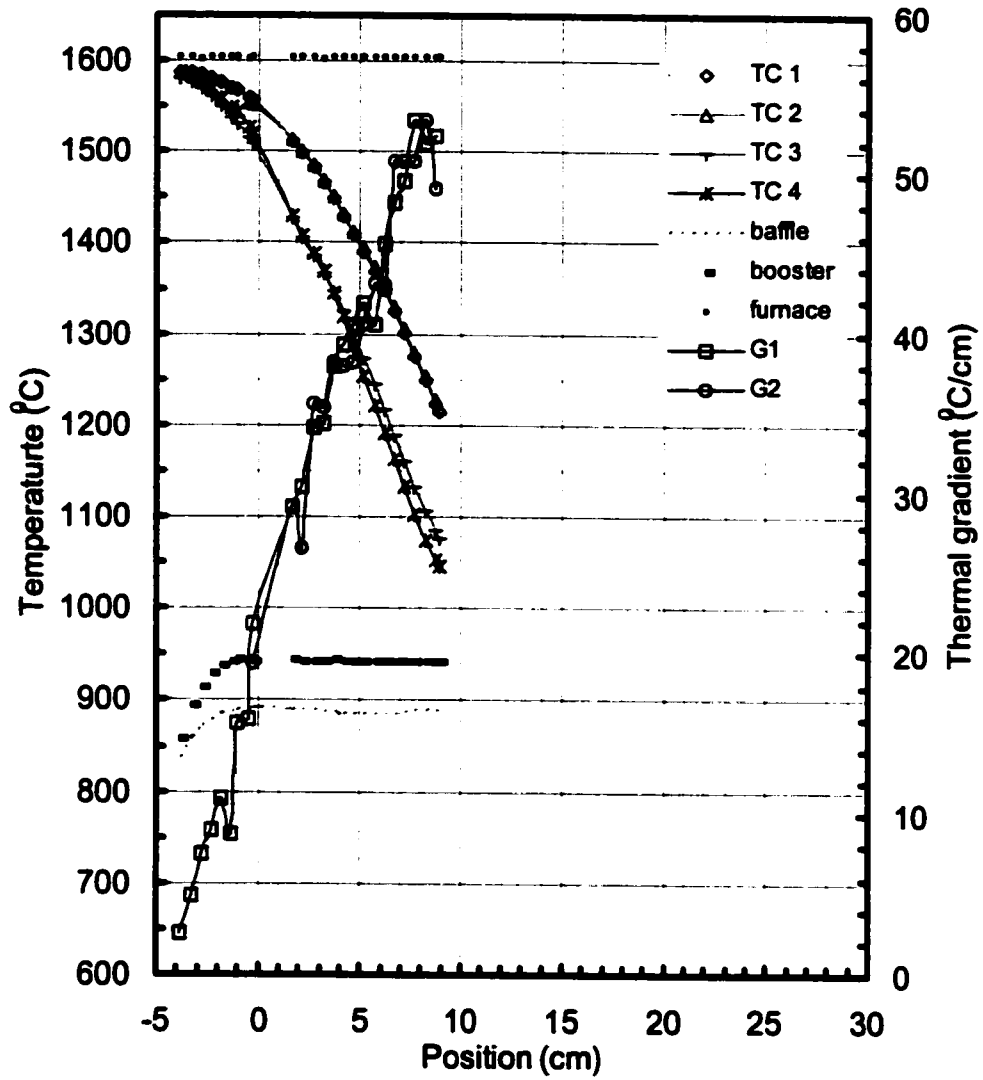
Figure A-5: V=0.0005cm/s and G=40 °C/cm. Furnace setting temperature = 1600 °C
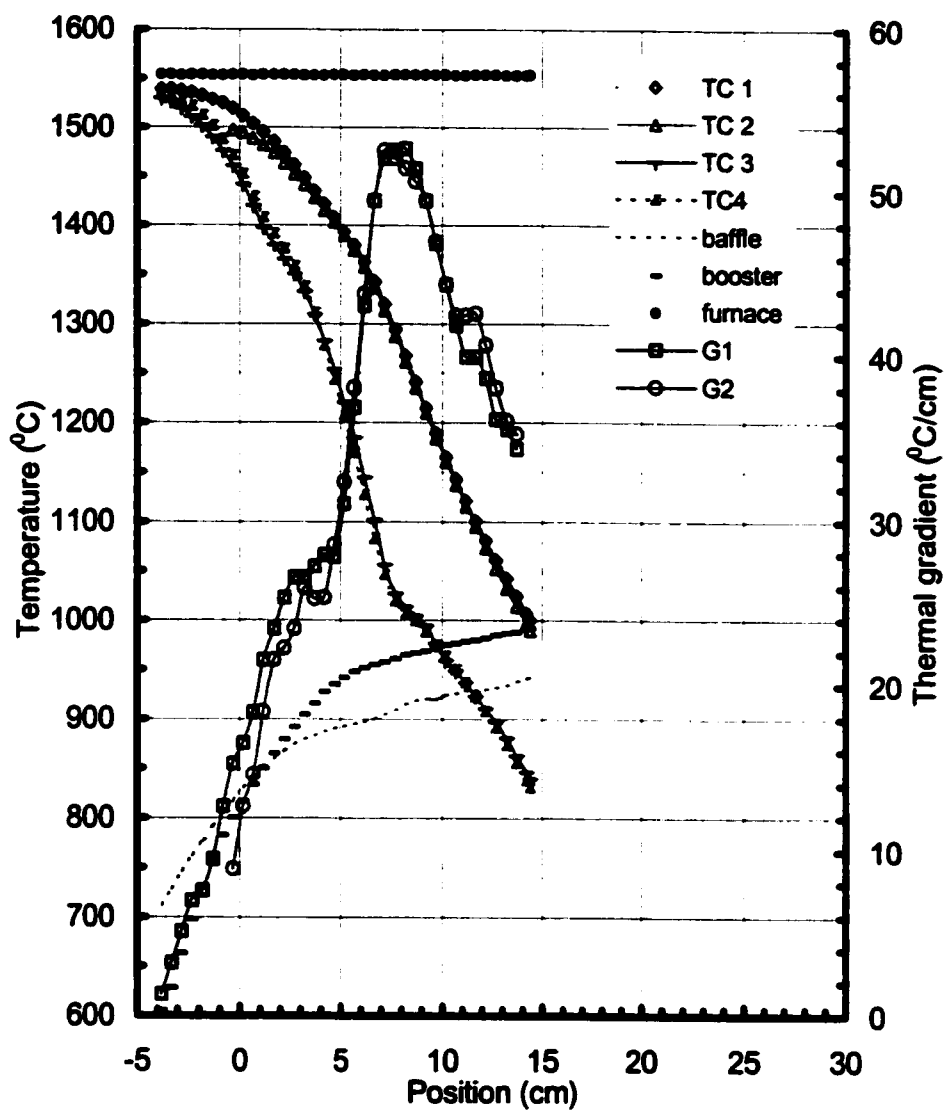
Figure A-6: V=0.005cm/s and G=28 °C/cm. Furnace setting temperature =1550 °C
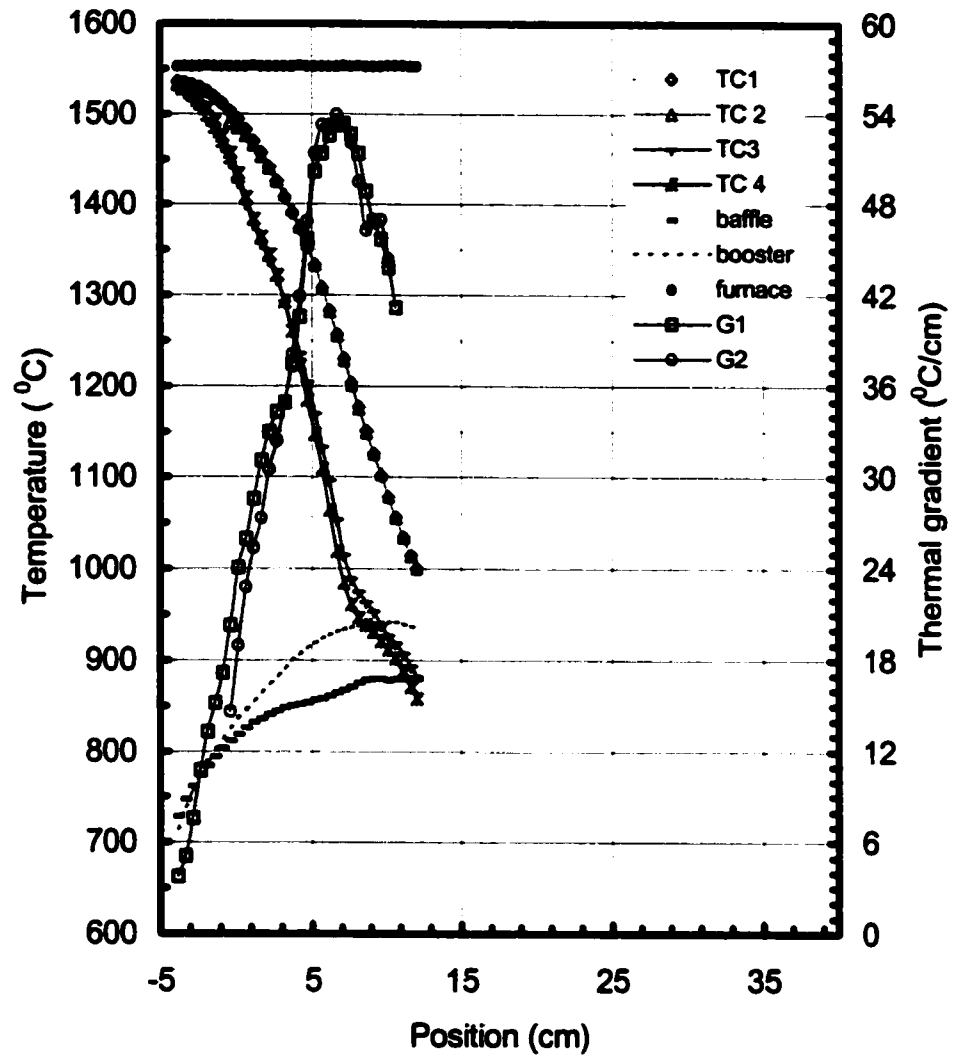
Figure A-7: V=0.0025cm/s and G=36 °C/cm. Furnace setting temperature =1550 °C
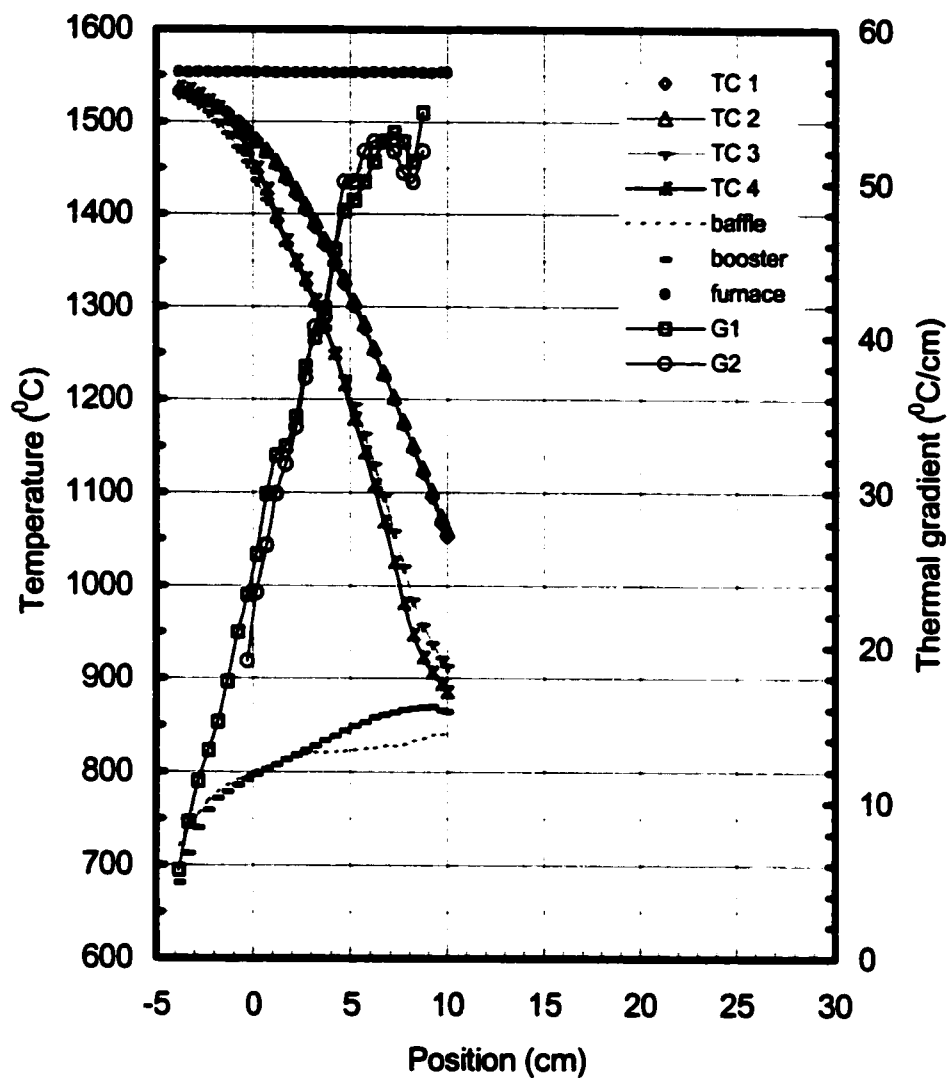
Figure A-8: V=0.001cm/s and G=38 °C/cm. Furnace setting temperature =1550 °C
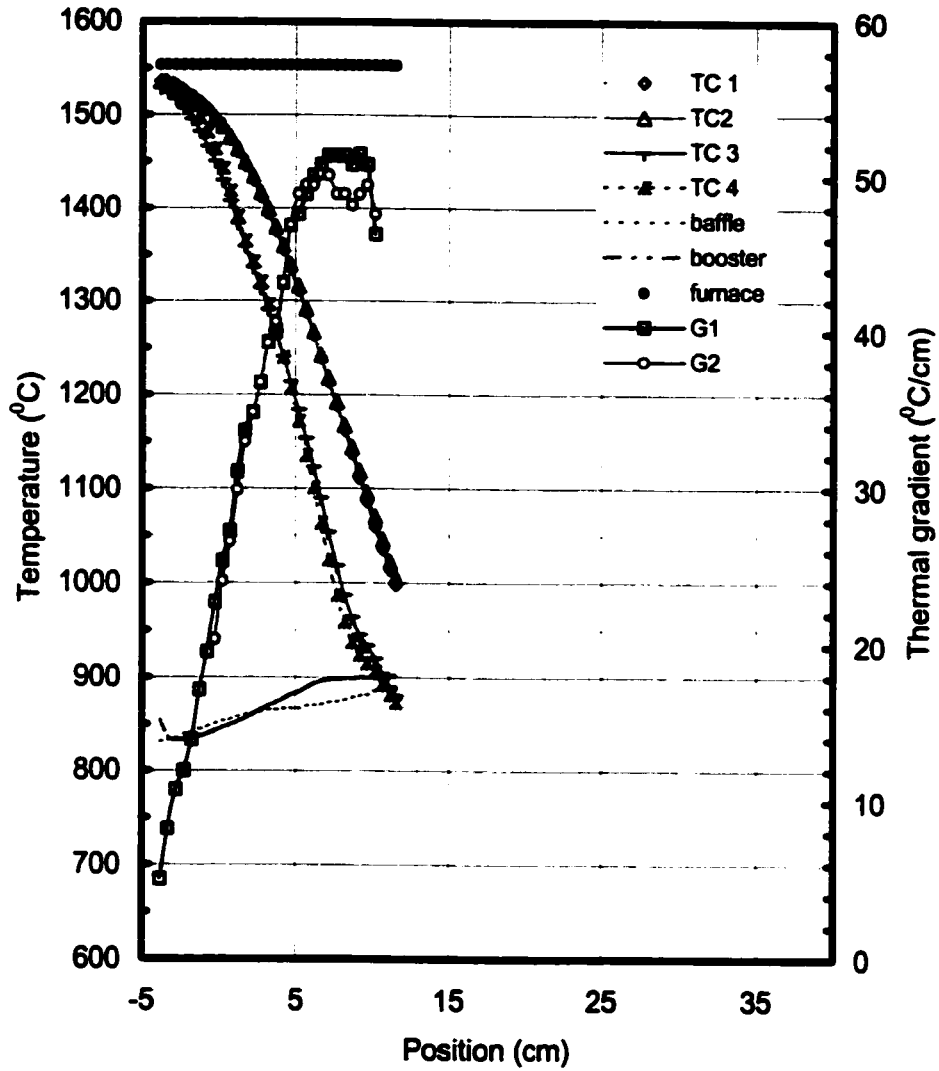
Figure A-9: V=0.0005cm/s and G=38 °C/cm. Furnace setting temperature =1550 °C
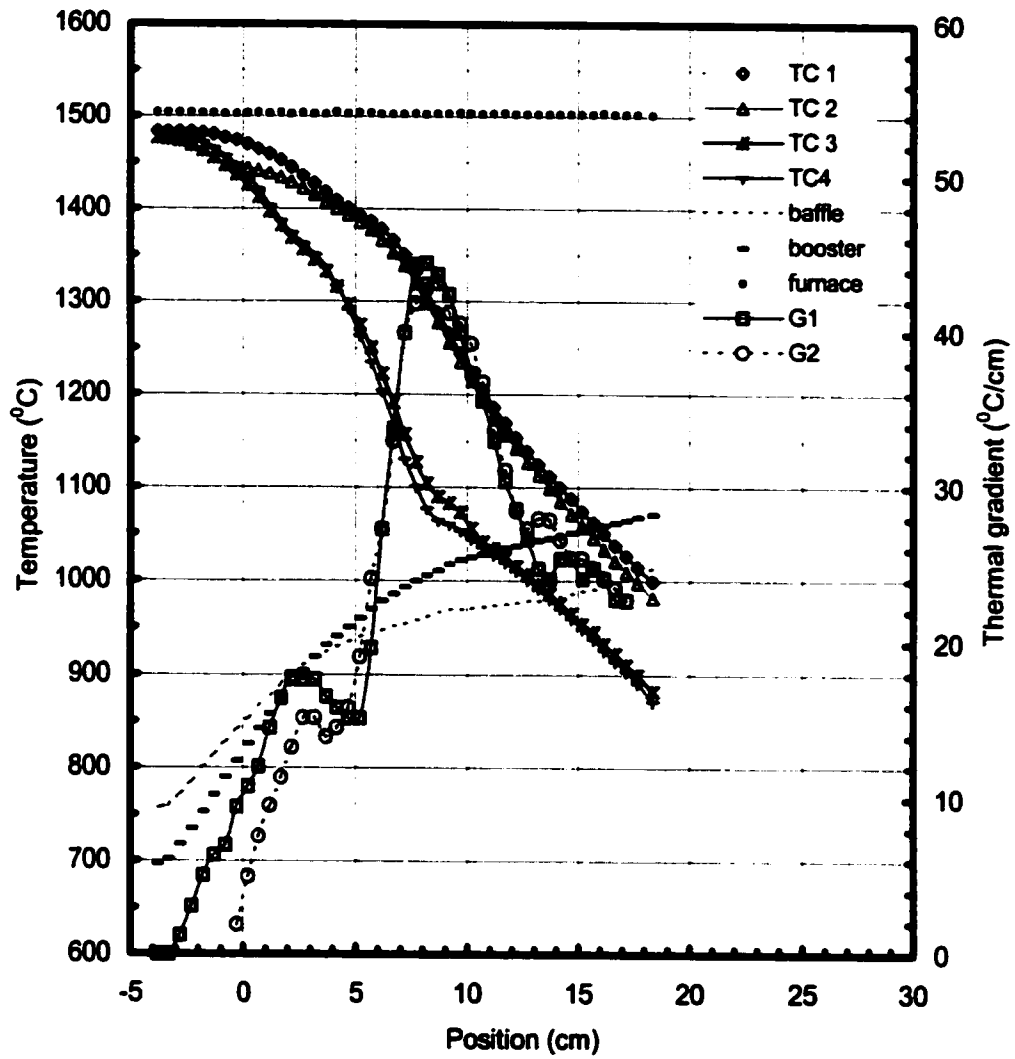
Figure A-10: V=0.01cm/s and G=15 °C/cm. Furnace setting temperature =1500 °C
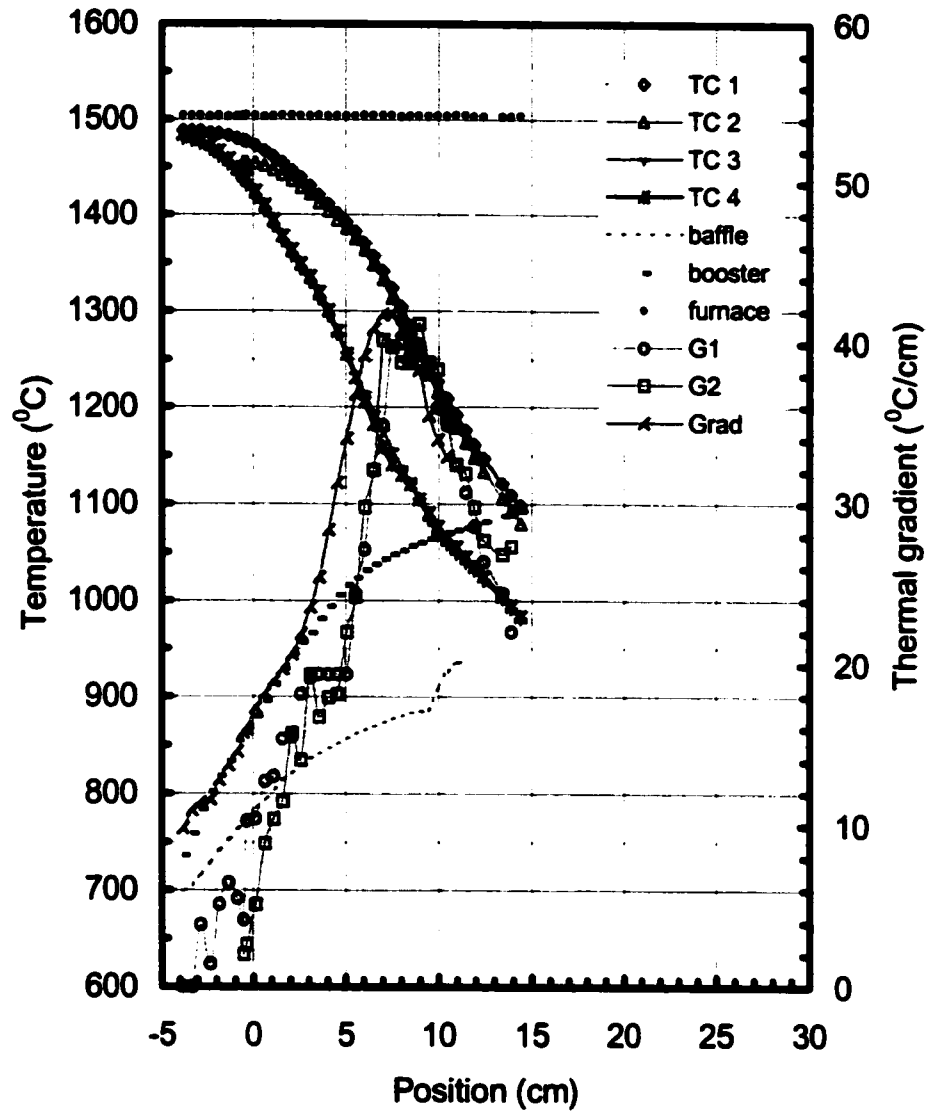
Figure A-11: V=0.005cm/s and G=20 °C/cm. Furnace setting temperature =1500 °C
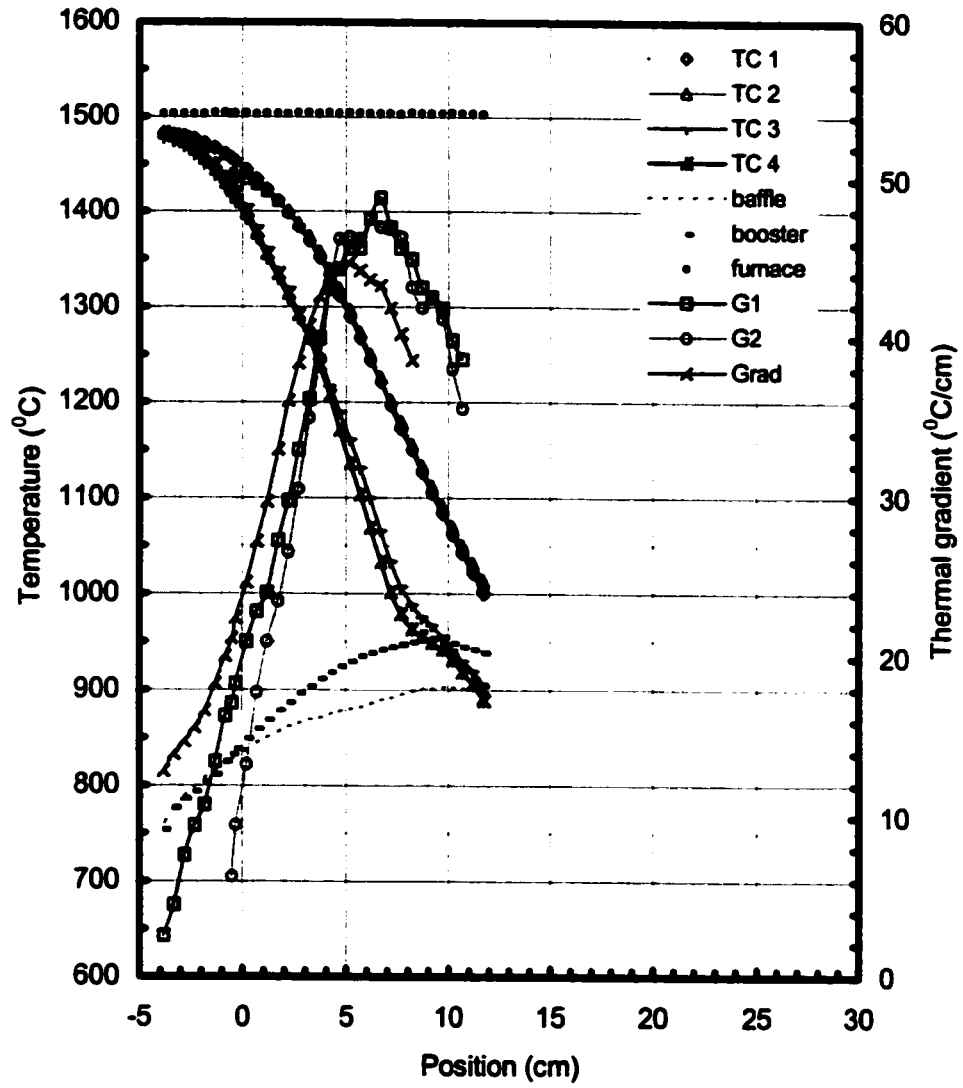
Figure A-12: V=0.0025cm/s and G=28 °C/cm.
Furnace setting temperature =1500 °C
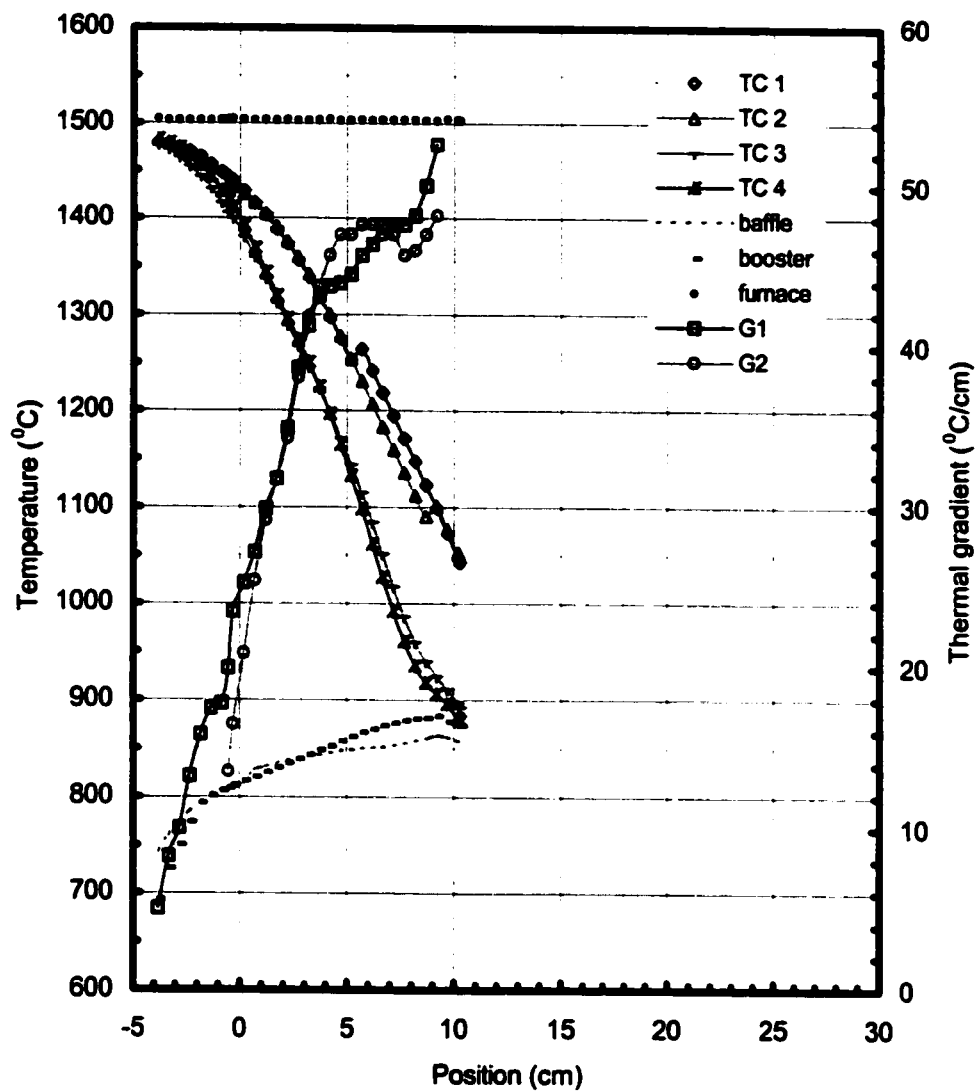
Figure A-13: V=0.001cm/s and G=28 °C/cm. Furnace setting temperature =1500 °C
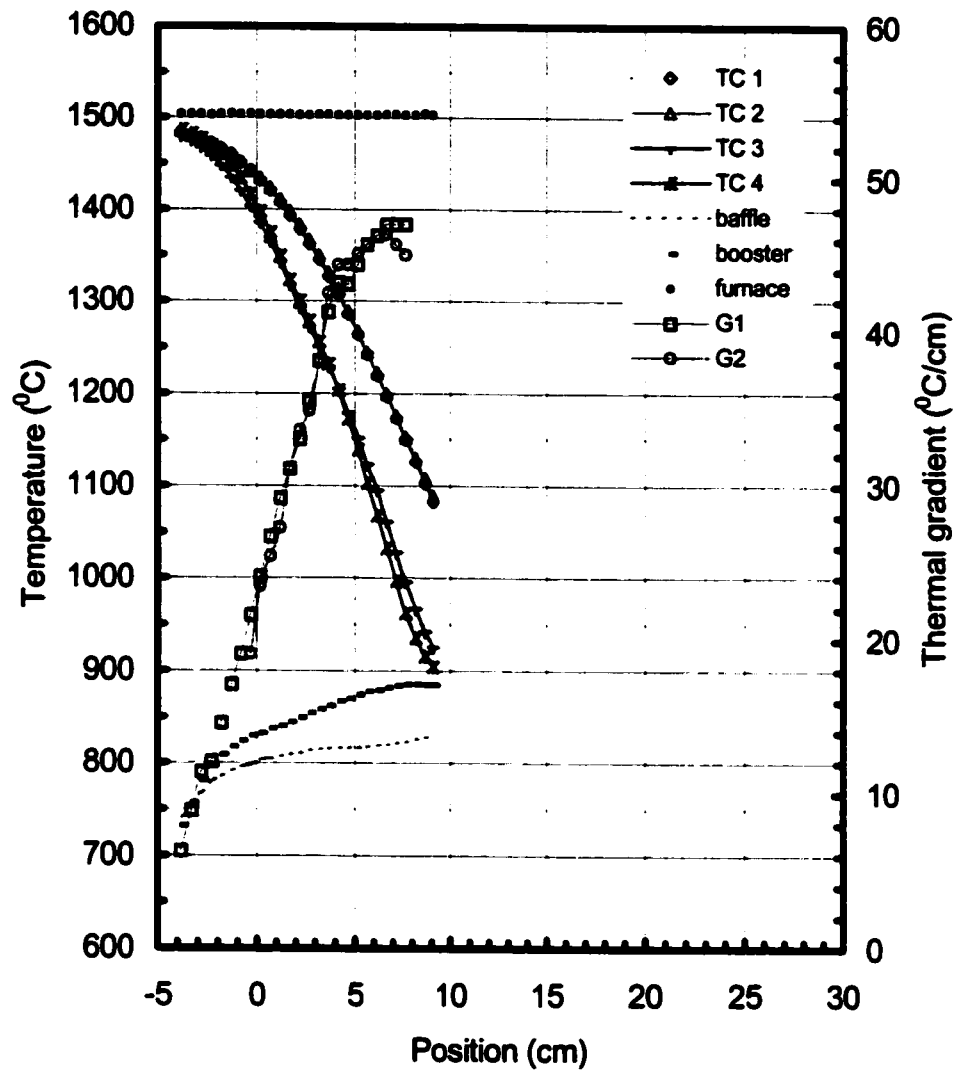
Figure A-14: V=0.0005cm/s and G=28 °C/cm.
Furnace setting temperature =1500 °C
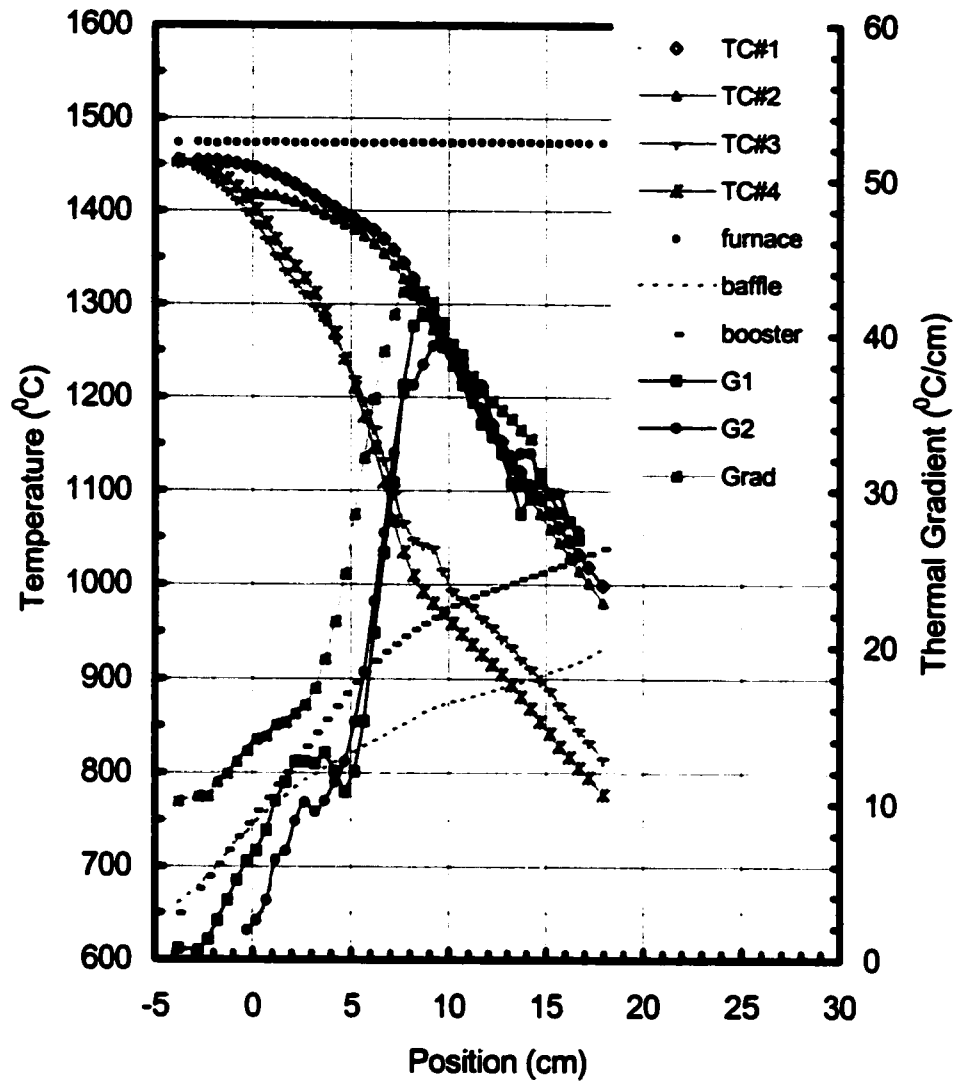
Figure A-15: V=0.01cm/s and G=12 °C/cm.
Furnace setting temperature =1470 °C
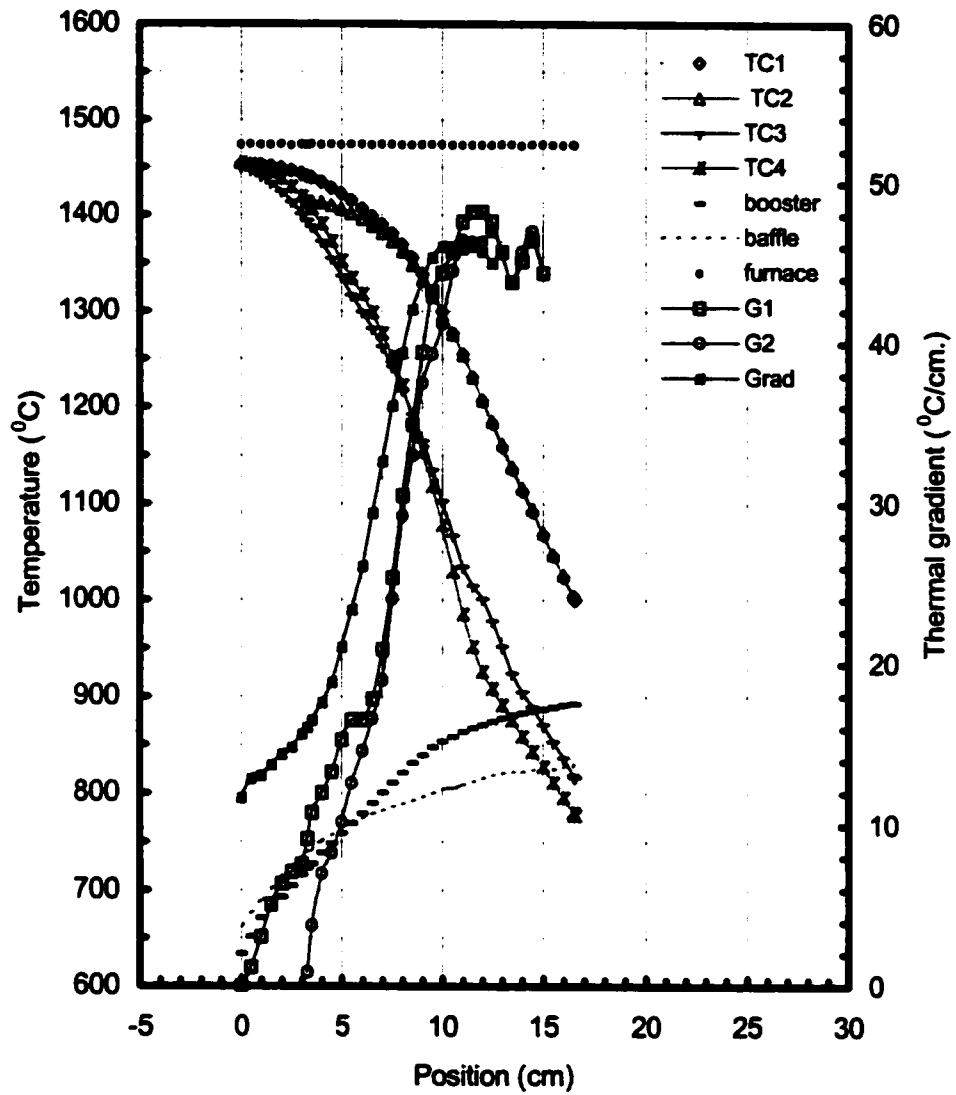
Figure A-16: V=0.005cm/s and G=18 °C/cm.

Furnace setting temperature =1470 °C
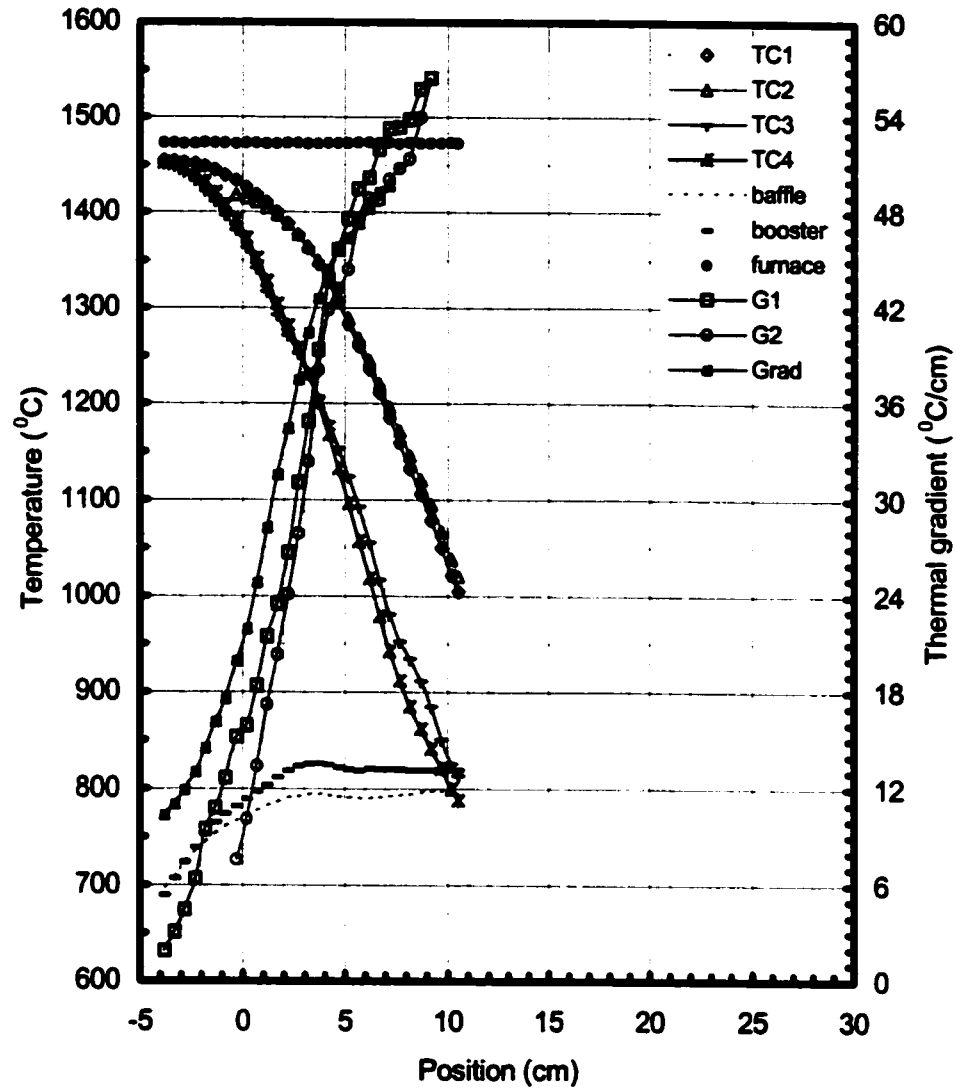
Figure A-17: V=0.0025cm/s and G=21 °C/cm.

Furnace setting temperature =1470 °C
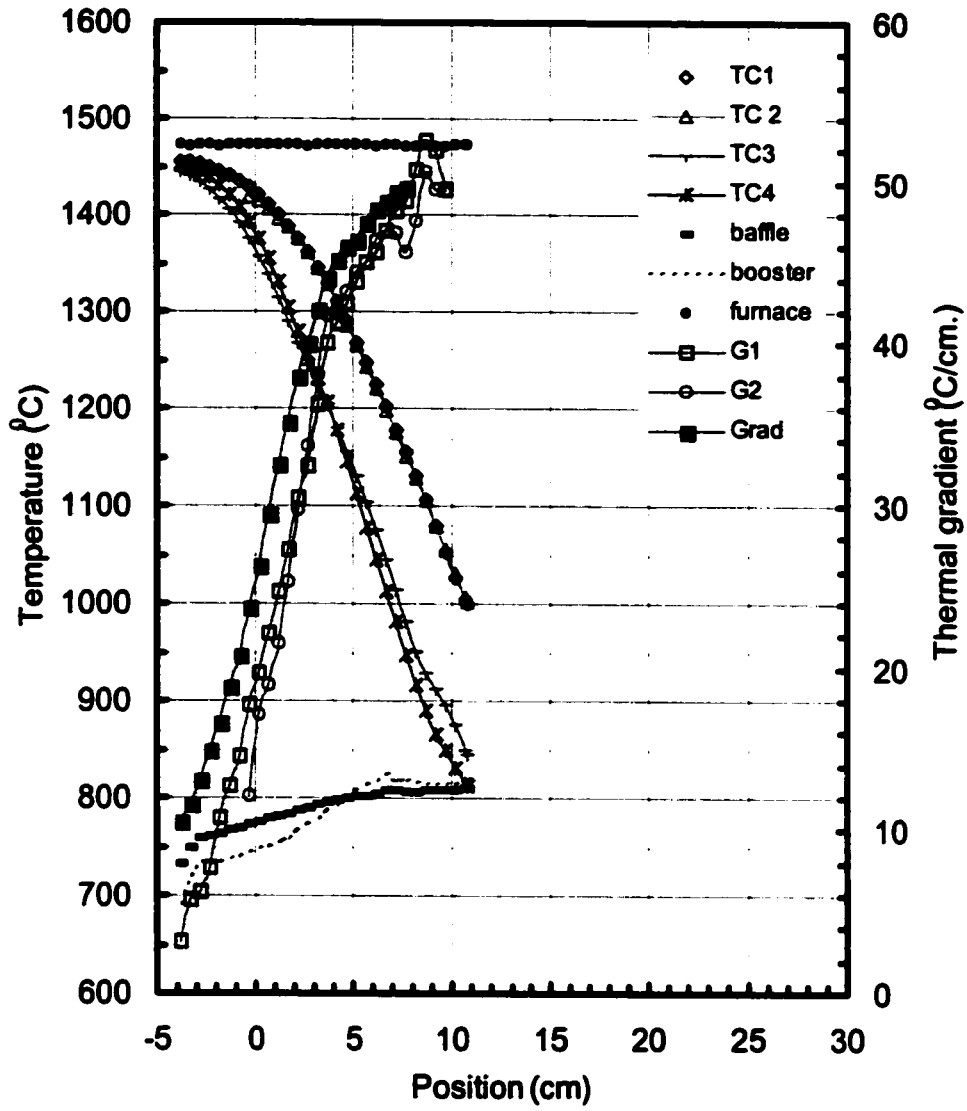
Figure A-18: V=0.001cm/s and G=23 °C/cm.

Furnace setting temperature =1470 °C
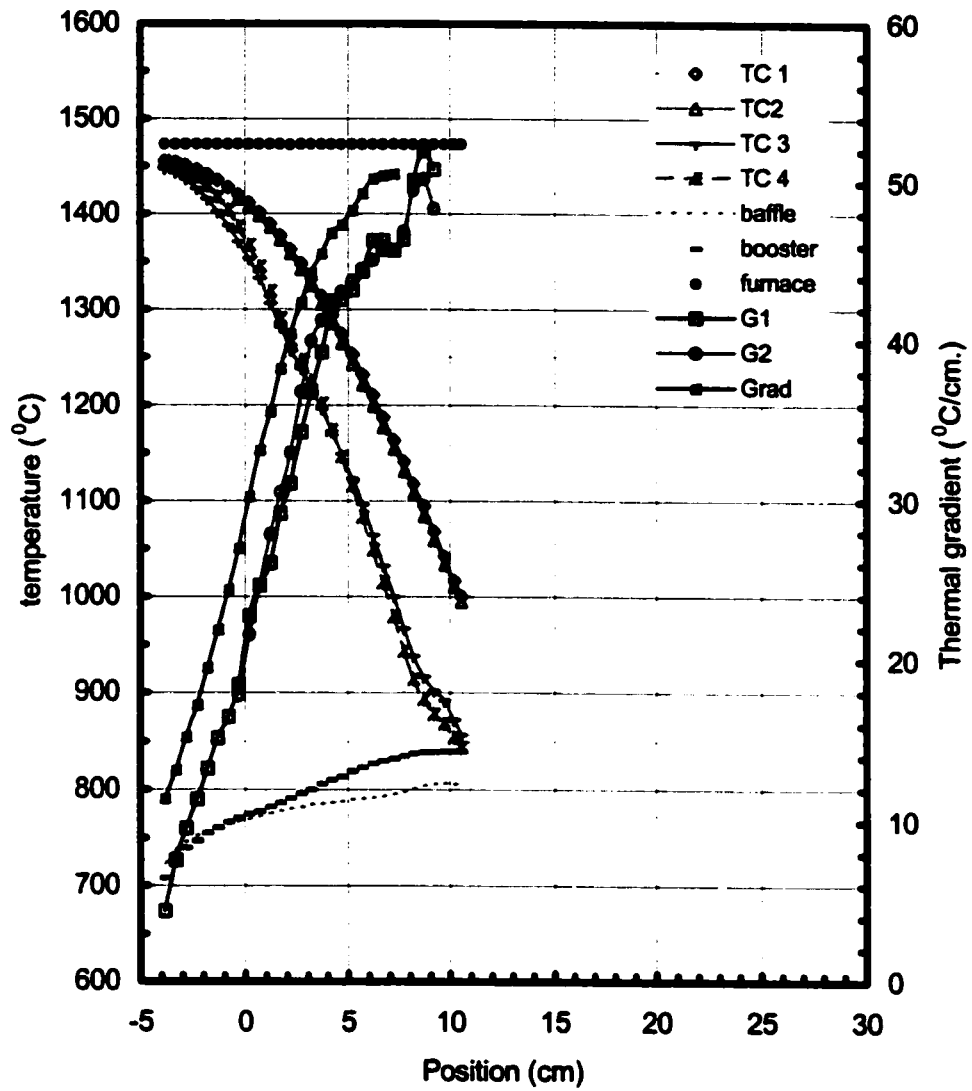
Figure A-19: V=0.0005cm/s and G=25 °C/cm.

Furnace setting temperature =1470 °C